eXPRESS Polymer Letters Vol.1, No.3 (2007) 122
Available online at www.expresspolymlett.com
DOI: 10.3144/expresspolymlett.2007.20

Editorial corner – a personal view

Trends – the future belongs to hybrid thermosets

J. Karger-Kocsis[*]

Institut für Verbundwerkstoffe GmbH (Institute for Composite Materials), Kaiserslautern University of Technology,
Erwin Schrödinger Str. 58, D-67663 Kaiserslautern, Germany

The commercial success with thermoplastics is mostly due to their ‘blending’. Via ‘blending, alloying’ the beneficial properties of the related thermoplastic resins can be combined and even tailored upon request in many cases. Blending does not necessary mean melt compounding, but covers numerous other techniques, as well (e.g. ‘reactor blends’ produced by in-situ polymerization).

Interestingly, fewer efforts were dedicated to follow this concept for thermosets, except rubbers. Similar to thermoplastic systems, the ‘blending concept’ was introduced for thermosets when starting with their toughening. Nowadays, toughened thermosets, especially epoxy resins, are commercialized. Their toughener content is usually less than 10 wt.%. The vivid academic interest in the past to prepare interpenetrating network (IPN) structured systems can be considered as the beginning of thermoset ‘hybridization’. Combination of two or more resins, which crosslink separately or co crosslink with each other in various extents, means a great potential for property modification. A commercial breakthrough with this concept was already achieved with unsaturated polyester-urethane and vinylester-urethane hybrid resins.

The driving force of resin hybridization in the future is linked with the necessary use of resins made (at least partly) from renewable resources. Note that the crosslinked network of resins of natural origin (e.g. from plant oils which will come sooner or later from gene-manipulated plants) can never be so tight as that of ‘traditional’ ones derived from petrochemical resources. This is due to the fact that the molecular segments between the crosslinking sites are much longer (and at the same time usually less reactive) than in the present systems. So, the related products are closer to rubbers than to thermosets which is well reflected by their low glass transition temperature (T_g). Consequently, additional co reactions and/or formation of IPN or IPN-like structures are needed to push the stiffness, strength and T_g toward higher values. It can be prophesied that the polyurethane chemistry will be one of the right tools to reach this target due to its versatility. However, we are faced with severe problems when following resin hybridization routes, from which only one has to be borne in mind here. The end-users prefer to utilize 1- or (maximum) 2-component systems, which can not always fulfilled by hybrids. To develop ‘user-friendly’, robust 2-component systems is a great challenge that can likely be met by adopting suitable blocking, end capping strategies. So, there is much to do, but it is of worth, is not it?

Prof. Dr.-Ing. Dr. h.c. József Karger-Kocsis
Editor-in-chief

---

[*] Corresponding author, e-mail: karger@ivw.uni-kl.de

eXPRESS Polymer Letters Vol.1, No.3 (2007) 123–131
Available online at www.expresspolymlett.com
DOI: 10.3144/expresspolymlett.2007.21

Tensile mechanical response of polyethylene – clay nanocomposites

A. Pegoretti*, A. Dorigato, A. Penati

Department of Materials Engineering and Industrial Technologies, and INSTM Research Unit, University of Trento, via Mesiano 7, 38050 Trento, Italy

Received 22 December 2006; accepted in revised form 14 February 2007

Abstract. In this work we report on the microstructural and the mechanical characteristics of high density polyethylene (HDPE)-clay nanocomposites, with particular attention to the creep behaviour. The samples were prepared through melt compounding, using two high-density polyethylenes with different melt flow rate (MFR), two different organo-modified clays, and changing the relative amount of a polyethylene grafted with maleic anhydride (PEgMA) compatibilizer. The intercalation process is more effective as the matrix melt viscosity decreases (higher MFR), while the clay interlamellar spacing increases as the compatibilizer amount increases. The relative stiffness of the nanocomposites increases with the addition of clay, with a limited enhancement of the relative yield stress. The better intercalation obtained by the addition of the compatibilizer is not accompanied by a concurrent improvement of the tensile mechanical properties. The creep resistance is enhanced by the introduction of clay, with an appreciable dependence on both the polyethylene and the clay type.

Keywords: *polymer composites, nanomaterials, polyethylene, clay, creep*

1. Introduction

The effective dispersion of nanostructured layered silicates with high aspect ratios may improve the mechanical, thermal and barrier properties of polymers, even at very low concentration [1–3]. High-density polyethylene (HDPE) is a commodity polymer broadly used for many industrial products. One of the most demanding applications of HDPE is the production of pipes and fittings for the transportation of water or gas under pressure. In this case, the creep behaviour is a very important property to be considered for the material selection. The preparation of HDPE-clay nanocomposites remains a scientific challenge. In fact the studies on HDPE-clay nanocomposites have been relatively few if compared to the huge literature existing on clay nanocomposites obtained with more polar polymers [4]. Effectively, polyolefins are difficult to intercalate in the interlayer space of hydrophilic swelling clays without chemical modification of one of the two pristine components. In order to solve the problem of the lack of interfacial adhesion between apolar polyethylene (PE) and polar layered silicates, the addition of PE grafted with maleic anhydride to the PE matrix has been proven to favour the intercalation/exfoliation process, with important improvements of the material stiffness, maintaining the ultimate stress and strain at an acceptable level [5–7].

In order to obtain a good chemical affinity between polyethylene and clay, the use of organoclay with high hydrophobicity is recommended [8, 9], and some researchers tried to use different organo-modifiers for clay functionalization [10–12]. Even if a number of papers have been published on the mechanical properties of melt-compounded PE-clay nanocomposites [4, 6, 13–27] , only Ranade *et al.* reported on their response to tensile creep [23].

---

*Corresponding author, e-mail: alessandro.pegoretti@ing.unitn.it

In particular, these authors found a substantial reduction of the creep compliance of HDPE blown films through the introduction of Cloisite® 15A clay and maleated polyethylene, and they successfully applied the Burger model to model the experimental data.

In this paper we used two different tube-grade polyethylenes and two different organoclays to produce PE-clay nanocomposites with and without a compatibilizer. The aim is to investigate the influence of the melt viscosity of the matrix, of the organoclay and compatibilizer concentrations on the microstructure and the mechanical behaviour of the resulting nanocomposites, with particular attention to the creep resistance.

2. Experimental

2.1. Materials

Two high density polyethylenes, having markedly different melt viscosities, were used:

- Lupolen 5031 L Q 449, density 0.952 g/cm³, melting temperature 131°C, MFR 6.5 g/10 min (190°C, 2.16 kg);
- Eltex A 4009 MFN 1325, density 0.960 g/cm³, melting temperature 134°C, MFR 0.9 g/10 min (190°C, 2.16 kg).

Both matrices were received in the form of fine powders.

Commercial organoclays Cloisite® 20A and Cloisite® 15A were supplied by Southern Clay Products Inc. These clays contain the same organomodifier, namely dimethyl dihydrogenated tallow ammonium (2M2HT), but in different concentrations, i.e. 95 meq/100 g for Cloisite® 20A and 125 meq/100 g for Cloisite® 15A. These two clays are among the most hydrophobic fillers of the Cloisite® series, due to the presence of long hydrocarbon chains in the organic modifier. In fact, hydrogenated tallow consists of about 65% C18, 30% C16, and 5% C14 fractions. Maleic anhydride grafted polyethylene Fusabond E MB 100D (DuPont) was used as compatibilizer. This compatibilizer has a density of 0.960 g/cm³, a MFR of 2 g/10 min (190°C, 2.16 kg), a melting temperature of 134°C, a maleic anhydride content of 0.9 wt%.

Since both compatibilizer and clay amounts were changed, the samples will be named in the order of HDPE/PEgMA/clay weight ratios hereafter.

2.2. Sample preparation

The preparation process was the same for all the composites. At first, the required amount of clay was mixed with HDPE powder and the compatibilizer with a mechanical stirrer (Dispermat F1), for 5 minutes at 500 rpm. The mixture was then melt compounded in a Thermo Haake Reomix 600p internal mixer working at 90 rpm at a temperature of 180°C for 17 minutes. The temperature was maintained relatively low in order to limit the organoclay degradation [28]. Square sheets (160 mm wide and 1.5 mm thick) were finally obtained by compression moulding in a Carver Laboratory press for 15 minutes at 180°C at a consolidation pressure of about 200 kPa.

2.3. Experimental methodologies

X-ray diffraction (XRD) analyses were performed by a Philips Xpert HRD diffractometer, using Cu $K\alpha$ ($\lambda = 0.15406$ nm) radiation, generated at a voltage of 40 kV and current of 30 mA. The diffraction angle 2θ was scanned from 1.75° to 10° at a step increment $\Delta\theta$ of 0.1°/s. By using Bragg' law, the XRD patters were used to calculate d-spacings of the clay layers. A relative intercalation (RI) of the clay in the polymeric matrix has been computed as a percentage increase of the d-spacing according to the following equation:

$$\mathrm{RI} = \left(\frac{d - d_0}{\mathrm{d}_0}\right)100 \tag{1}$$

where d_0 and d are the d-spacings of the pristine clay and the clay in the nanocomposites, respectively.

Tensile tests under constant rate and creep conditions were performed by an Instron 4502 universal testing machine on specimens punch-cut from the compression moulded plaques. Constant rate experiments were conducted on ISO 527 1BA dumbbell specimens. The tensile modulus was evaluated at a cross-head speed of 0.25 mm/min by using an electrical clip gage extensometer with a gage length of 12.5 mm. According to ISO 527 standard, the modulus was calculated as a secant modulus between 0.05% and 0.25% strain. The same specimens were used for the evaluation of the yield and fracture tensile parameters at a cross-head speed of 50 mm/min. The creep tests were conducted on rectangular strips 60 mm long and 5 mm

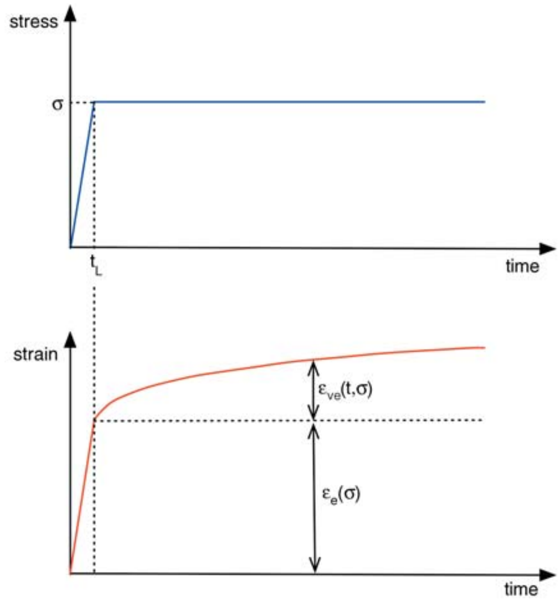

Figure 1. Schematic of the creep experiments and strain components

wide, in a thermostatic chamber at 30°C, at a constant nominal stress (σ_0) of 10 MPa. A schematic of the creep experiments is detailed in Figure 1. The loading ramp was performed at a cross-head speed of 25 mm/min that resulted in a loading time (t_L) always lower than 2 s.

3. Results and discussion

3.1. X-ray diffraction measurements

From the data reported in Table 1 it is evident that for both types of clays, Lupolen/clay intercalation is markedly promoted by PEgMA compatibilizer. In some cases, for non-compatibilized composites, negative RI values are reported, indicating a slight reduction of the clay interlayer distance. This phenomenon has been already reported by Shah *et al.* [28] and attributed to a processing-induced degradation of the quaternary ammonium surfactant of the organoclay. The data reported in Table 1 also reveal that, for a given compatibilizer amount, Cloisite® 20A can be intercalated to a much higher extent than Cloisite® 15A, thus indicating a better intercation of Cloisite®20A with both Lupolen and Eltex HDPE matrices. As described in the experimental part, the two organoclays contain the same type of organomodifier but in different concentrations. As a consequence, Cloisite® 15A is slightly less hydrophobic than Cloisite® 20A, as recently assessed by measuring the vibration induced equilibrium contact angles of water droplets on clay disks[29]. The slightly lower hydrophobicity of Cloisite® 20A may account for the better intercalation observed when the PEgMA compatibilizer is introduced in the system.

It is worthwhile to note that the intercalation process is far more effective for Lupolen than for Eltex based HDPE nanocomposites. This result can be explained by considering that the two polymeric matrices have markedly different MFR values, and the lower viscosity of the Lupolen is surely responsible of the better polymer-clay intercalation. This is in contrast with literature data on polyamide 6 where a better delamination was obtained by increasing the molecular weight of the polymer [30]: this result was attributed to the mechanical assistance to delamination of the clay by the larger shear stress in the extrusion process due to the larger melt viscosity of the polymer with larger molecular weight. On the other hand, our findings are in agreements with the experimental works on polyolefin-clay nanocomposites [31, 32]. In partic-

Table 1. XRD results of HDPE/PEgMA/clay nanocomposites

Sample composition	Lupolen			Eltex		
HDPE/PEgMA/clay	001 peak 2θ [deg]	d [nm]	RI [%]	001 peak 2θ [deg]	d [nm]	RI [%]
Cloisite® 15A						
0/0/100	2.85	3.098	–	2.85	3.098	–
98/0/2	2.76	3.198	3.26	–	–	–
95/0/5	2.90	3.044	–1.72	–	–	–
88/10/2	2.65	3.331	7.55	2.95	2.993	–3.39
85/10/5	2.75	3.210	3.64	2.75	3.210	3.64
Cloisite® 20A						
0/0/100	3.30	2.675	–	3.30	2.675	–
98/0/2	3.15	2.803	4.76	–	–	–
95/0/5	3.40	2.597	–2.94	–	–	–
88/10/2	2.65	3.331	24.52	3.05	2.894	8.19
85/10/5	2.65	3.331	24.52	3.15	2.803	4.76

ular, Giannelli *et al.* [31] studied the effect of the polypropylene based resin on the properties of organoclay-PP nanocomposites prepared by melt compounding using a twin screw extruder, and reported that the delamination of organoclays is favoured at high MFR for both homopolymers and heterophasic copolymers. In this case it seems that the organophilic environment, created in the layers interspace by combination of the organic cation and maleic anhydride grafted polypropylene, drives the delamination process through thermal diffusion control, making mechanical contribution negligible. In the present case a similar explanation could be invoked to explain our experimental results.

Following these preliminary results, the effect of the compatibilizer amount on the Cloisite® 20A intercalation level in Lupolen HDPE matrix has been investigated, and the results are summarized in Figure 2. It is clearly evident that the intercalation level almost linearly increases as the weight fraction of compatibilizer increases. Moreover, for the compatibilized samples the intercalation degree increases as the clay loading increases. In the existing literature, contradictory results are reported on this point. In fact, consistently with our observations, some authors reported an increase of the intercalation level with the clay loading [2, 11, 27], while other authors observed an opposite trend [33, 34].

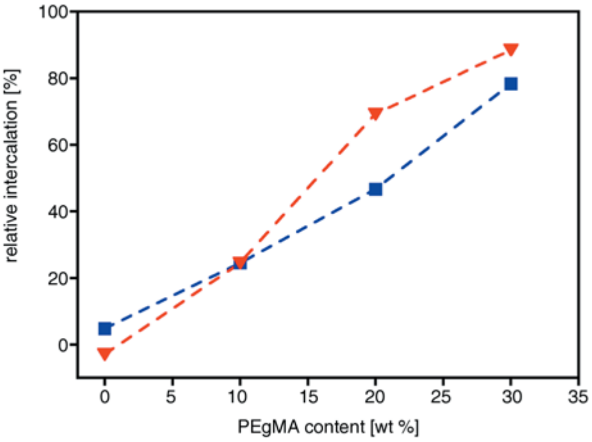

Figure 2. Effect of the PEgMA content on the relative intercalation of (■) 2 wt% and (▼) 5 wt% of Cloisite 20A in the Lupolen HDPE matrix

3.2. Constant rate tensile tests

As for most thermoplastics, the deformation was uniform along the gauge length up to the yield point (conventionally evaluated in correspondence of the zero-slope point on the engineering stress-strain curve). After the yield point, a neck in formed in the specimens and the permanent deformation is localized in this region that gradually extends to the whole gauge length. Table 2 summarizes the tensile modulus (E), yield stress (σ_y) and strain at break (ε_r) values of Lupolen and Eltex HDPE matrices both neat and filled with 2 and 5 wt% of Cloisite® 15A and 20A clays, with or without a 10 wt% of PEgMA compatibilizer.

For both HDPE matrices, the introduction of the compatibilizer at this percentage causes a slight decrease of the tensile modulus, remaining the yield stress and strain at break values practically unchanged. The effect of clay addition is markedly dependent on the polymer-clay intercalation level. In fact, for non-compatibilized samples (low intercalation level) the addition of Cloisite® 15A and 20A clays at 2 and 5 wt% does not cause an appreciable tensile modulus variation, that is instead observed for nanocomposites with PEgMA com-

Table 2. Tensile mechanical properties of HDPE/PEgMA/clay nanocomposites

Sample composition	**Lupolen**			**Eltex**		
HDPE/PEgMA/clay	**E [MPa]**	**σ_y [MPa]**	**ε_r [%]**	**E [MPa]**	**σ_y [MPa]**	**ε_r [%]**
100/0/0	932 ± 41	27.7 ± 0.1	1173 ± 50	1252 ± 32	30.5 ± 0.2	1650 ± 302
90/10/0	877 ± 36	27.2 ± 0.3	922 ± 282	1168 ± 75	30.6 ± 0.2	1697 ± 566
Cloisite® 15A						
98/0/2	934 ± 18	27.7 ± 0.5	166 ± 23	–	–	–
95/0/5	928 ± 21	26.0 ± 0.4	36 ± 25	–	–	–
88/10/2	1156 ± 45	27.8 ± 0.4	225 ± 97	1283 ± 114	29.7 ± 0.1	1406 ± 809
85/10/5	1112 ± 64	–	14 ± 8	1379 ± 85	28.7 ± 0.1	21 ± 7
Cloisite® 20A						
98/0/2	917 ± 62	28.2 ± 0.2	172 ± 18	–	–	–
95/0/5	975 ± 87	26.7 ± 0.3	14 ± 3	–	–	–
88/10/2	1147 ± 40	28.1 ± 0.2	51 ± 45	1400 ± 65	30.3 ± 0.2	692 ± 516
85/10/5	1184 ± 37	–	10 ± 2	1341 ± 75	29.6 ± 0.7	18 ± 7

patibilizer. The elastic modulus improvements are higher for the Lupolen than for Eltex based nanocomposites. The 5 wt% Cloisite® 20A filled Lupolen sample, with 10 wt% compatibilizer, shows an enhancement of the 35% of the elastic modulus, compared to the unfilled compatilized matrix, while the improvement for the Eltex sample, filled with the same amount of the same clay, is 15%. Moreover, the stiffness improvement is more effective for Cloisite® 20A filled nanocomposites than for Cloisite® 15A filled nanocomposite, confirming the microstructural observations of the XRD tests.

For as the yield stress is concerned, the 2 wt% filled Lupolen nanocomposites show a little but significant enhancement of the yield point, when the compatibilizer is used. When an higher clay amount of 5 wt% is introduced, sample breakage occurs before the yield point is reached. For the Eltex based nanocomposites, a decrease of σ_y is evident, which accounts for a weaker polymer-clay interaction. The yield stress improvements are higher for the Cloisite® 20A filled nanocomposite. It is worthwhile to note, that a σ_y enhancement, even if small, is an indicator of a good filler matrix interaction [17, 22–24]. At the same time, the introduction of clay in these HDPE matrices has detrimental effects on the elongation at break of the resulting nanocomposites, the worst case being that of 5 wt% clay filled Lupolen nanocomposites that break before yielding.

In order to assess an optimal amount of PEgMA compatibilizer, its effect on the tensile modulus and yield strength of Lupolen based nanocomposites filled with 2 and 5 wt% of Cloisite® 20A has been assessed. The obtained results are reported in Figure 3.

For any given PEgMA concentration the tensile modulus increases proportionally to the clay content. It is worthwhile to note that, for elevated amounts of compatibilizer (20–30 wt%), the expected modulus improvement related to the better polymer-clay intercalation is not occurring, and that an optimal compatibilizer concentration can be detected at 10 wt%. A similar result has been observed by Hotta and Paul [17] for organoclay filled nanocomposites based on linear low density polyethylene (LLDPE). In fact, when the amount of compatibilizer consisting of maleic anhydride grafted linear low density polyethylene (LLDPE-g-MA) is varied, these authors observed a slight maximum in both modulus and yield strength in the blends occurring at about 10 wt% of LLDPE-g-MA.

Concurrently, the presence of high compatibilizer amounts causes a significant reduction of the tensile yield strength, both for the unfilled matrix and for the nanocomposites filled with 2 wt% and 5 wt% of Cloisite® 20A. A quite unexpected result is represented by the very low yield strength value observed for the uncompatibilized composites filled with 5 wt% clay, which is suggesting a possible lubricating effect of the clay platelets at this loading level.

3.3. Tensile creep tests

The strain in isothermal tensile creep, $\varepsilon(t,\sigma)$, depending on time *t* and stress σ, is usually viewed as consisting of three components: [35–37] (i) elas-

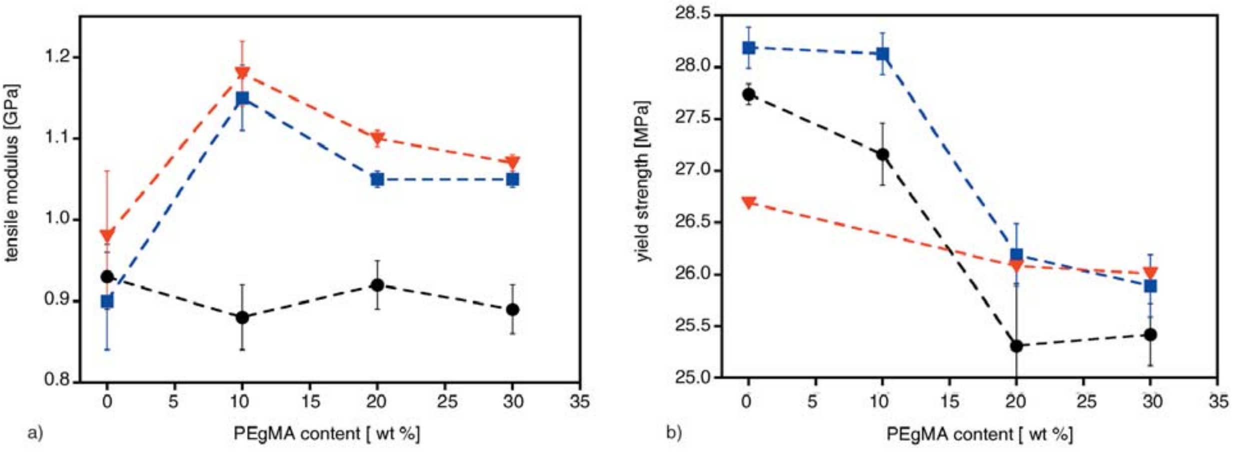

Figure 3. Effect of the PEgMA content on the a) tensile modulus and b) yield strength of the HDPE Lupolen matrix unfilled (●), and filled with 2 wt% (■) and 5 wt% (▼) of Cloisite® 20A

tic (instantaneous, reversible) $\varepsilon_e(\sigma)$; (ii) viscoelastic (time-dependent, reversible) $\varepsilon_{ve}(t,\sigma)$; (iii) plastic (irreversible) $\varepsilon_p(t,\sigma)$:

$$\varepsilon(t,\sigma) = \varepsilon_e(\sigma) + \varepsilon_{ve}(t,\sigma) + \varepsilon_p(t,\sigma) \tag{2}$$

Linear stress-strain behavior implies that the magnitudes of the three components are linearly proportional to the magnitude of the applied stress, so that a creep compliance $D(t) = \varepsilon(t)/\sigma$ can be defined as a function of time only. If no plastic deformation is produced in the course of creeping, the tensile compliance $D(t,\sigma) = \varepsilon(t,\sigma)/\sigma$ for the isothermal creep reads

$$D(t) = D_e + D_{ve}(t) \tag{3}$$

In the current study, Equation (3) has been adopted to analyse the experimental data. In fact, all the experiments have been performed under the same applied stress in order to avoid non-linearity effects. Moreover, the specimens recovered their initial length after unloading, thus excluding the presence of plastic deformations.

Representative curves of total creep compliance of Lupolen and Eltex based samples are reported in Figure 4a and 4b, respectively. Interestingly, at any time within the experimental window, the presence of 10 wt% of PEgMA compatibilizer leads to an increase of the creep compliance, while the introduction of – 2 wt% of Cloisite® 20A clay causes an appreciable reduction of the creep compliance. It is also worthwhile to note that the creep resistance of Lupolen and Eltex based nanocomposites is improved by the same level regardless the different intercalation levels reached for the two matrices. This experimental evidence is in agreement with the results recently reported by Siengchin and Karger-Kocsis [38] on the creep behaviour of polystyrene/fluorohectorite micro- and nanocomposites. In fact, these authors observed that the creep compliance curves of micro and nano-composites lay parallel to one another, at least until a given threshold, thus indicating that the creep response in this stable creep range is matrix dominated. As a consequence, the major effect of the reinforcement is the reduction of the initial compliance.

Table 3 summarizes the isochronous creep compliance components of Cloisite® 20A filled nanocomposites with or without 10 wt% of PEgMA compatibilizer. The data obtained for Lupolen based samples indicate that an improvement of the creep resistance can be reached only if the compat-

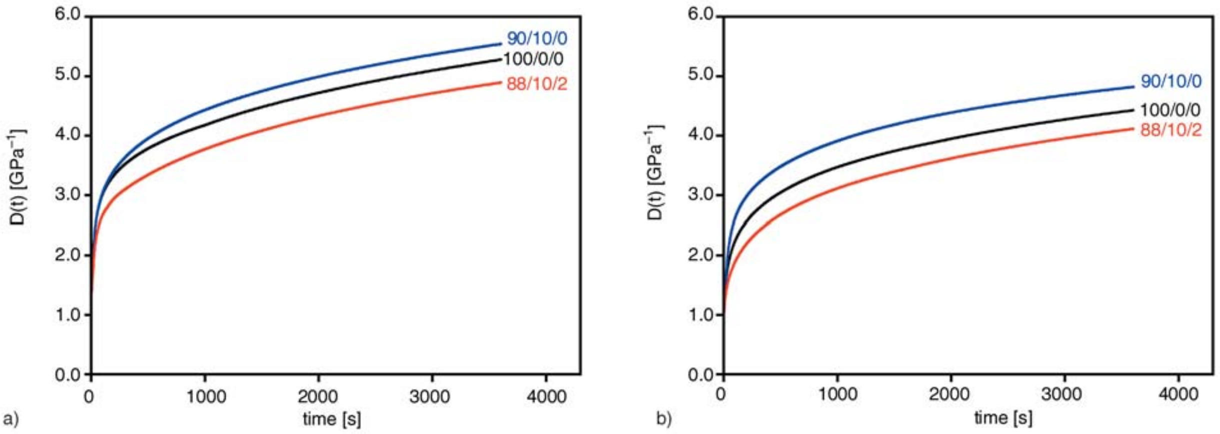

Figure 4. Typical creep curves of some HDPE/PEgMA/clay nanocomposites based on a) Lupolen and b) Eltex HDPE matrices and filled with Cloisite® 20A clay

Table 3. Isochronous creep compliance (D) and its elastic (D_e) and viscoelastic (D_{ve}) components at a time of 2000 s for HDPE nanocomposites filled with Cloisite® 20A

Sample composition	**Lupolen**			**Eltex**		
HDPE/PEgMA/clay	**D [GPa⁻¹]**	**D_e [GPa⁻¹]**	**D_{ve} [GPa⁻¹]**	**D [GPa⁻¹]**	**D_e [GPa⁻¹]**	**D_{ve} [GPa⁻¹]**
100/0/0	4.722	1.462	3.260	3.948	0.942	3.006
90/10/0	4.995	1.415	3.580	4.391	1.100	3.291
98/0/2	5.002	1.592	3.410	–	–	–
95/0/5	4.901	1.433	3.467	–	–	–
88/10/2	4.331	1.279	3.052	3.622	0.878	2.744
85/10/5	4.752	1.187	3.565	3.792	0.895	2.897

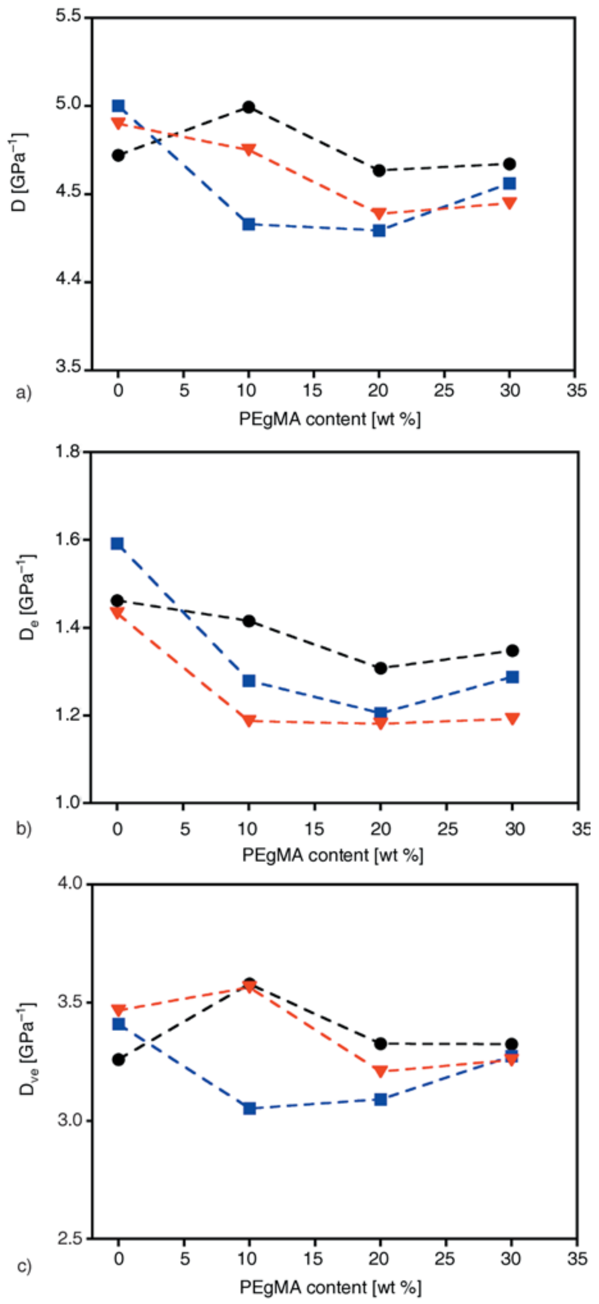

Figure 5. Isochronous creep compliance a) and its elastic b), and viscoelastic c) components at a time of 2000 s for HDPE Lupolen matrix unfilled (•), and filled with 2 wt% (■) and 5 wt% (▼) of Cloisite® 20A

ibilizer is used. In fact, for both Lupolen and Eltex based nanocomposites the creep compliance is reduced when a 2 wt% of clay and a 10 wt% of compatibilizer are added. It is wortwhile to note that if an higher amount of clay is added (5 wt%) no further improvements of the creep resistance are observed. In particular, even if the elastic component of the creep compliance is reduced, this effect is negatively counterbalanced by an increase of the viscoelastic component.

The creep behaviour as a function of the PEgMA content has been investigated for Lupolen based nanocomposites filled with 2 and 5 wt% of Cloisite® 20A. The creep compliance and its elastic and viscoelastic components are reported in Figure 5a, 5b and 5c, respectively.

For all the compatibilized samples, the introduction of clay leads to a decrease of the total compliance with respect to the corresponding unfilled matrices. At he same time, it is possible to note that when the clay amount is increased to 5 wt% the creep compliance increases, with the only exception of the samples with 30 wt% of PEgMA. This trend can be tentatively explained by considering that the elastic creep component is reduced proportionally to the clay amount as expected (see Figure 5b), while the viscoelastic component is negatively affected by the presence of an high percentage clay (see Figure 5b). The viscoelastic component of the creep compliance represents the solid-state flow behaviour of the materials, which is most probably governed by the yield strength. In fact, similarly to the yield strength, the peculiar trend of the viscoelastic component of the creep compliace could be tentatively related to a possible lubricating effect of the clay platelets at this loading level.

4. Conclusions

Polyethylene - clay nanocomposites were produced by melt compounding, using two HDPEs with different melt flow rate, two different organo-modified clays, and changing the relative amount of PEgMA compatibilizer.

The intercalation process is more effective as the matrix melt viscosity decreases (higher MFR), while the clay interlamellar spacing increases as the compatibilizer amount increases. Cloisite® 20A filled nanocomposites show better intercalation and mechanical properties than Cloisite® 15A filled samples.

The relative stiffness of the nanocomposites increases with the addition of clay, with a limited enhancement of the relative yield stress. The better intercalation obtained by the addition of the compatibilizer is not accompanied by a concurrent improvement of the tensile mechanical properties.

The creep resistance is enhanced by the introduction of clay that induces a decrease of the creep compliance, provided that the PEgMA compatibilizer is added.

Acknowledgements

This research was party supported by Eurostandard SpA (Tesero – Trento, Italy). The authors express their appreciation to DuPont (Dr. Tatiana Damian, Packaging & Industrial Polymer) for the kind provision of the PEgMA compatibilizer used in this research.

References

[1] Mandalia T., Bergaya F.: Organo-clay mineral-melted polyolefin nanocomposites. Effect of surfactant/CEC ratio. Journal of Physics and Chemistry of Solids, **67**, 836–845 (2005).

[2] Zhang J., Jiang D. D., Wilkie C. A.: Thermal and flame properties of polyethylene and polypropylene nanocomposites besed on an oligomerically moified clay. Polymer degradation and stability, **91**, 298–304 (2006).

[3] Yuan Q., Misra R. D. K.: Impact fracture behaviour of clay-reinforced polypropylene nanocomposites. Polymer, **47**, 4421–4433 (2006).

[4] Bergaya F., Mandalia T., Amigouet P.: Abrief survey on CLAYPEN and nanocomposites based on unmodified PE and organo-pillared clays. Colloid Polymer Science, **283**, 773–782 (2005).

[5] Lu H., Hu Y., Xiao J., Kong Q., Chen Z., Fan W.: The influence of irradiation on morphology evolution and flammability properties of maleated polyethylene/clay nanocomposite. Materials Letters, **59**, 648–651 (2005).

[6] Osman M. A., Rupp J. E. P., Suter U. W.: Effect of non-ionic surfactants on the exfoliation and properties of polyethylene-layered silicate nanocomposites. Polymer, **46**, 8202–8209 (2005).

[7] Chrissopolou K., Altintzi I., Anastasiadis S. H., Giannelis E. P., Pitsikalis M., Hadjichristidis N., Theophilou N.: Controlling the miscibility of polyethylene/layered silicate nanocomposites by altering the polymer/surface interactions. Polymer, **46**, 12440–12451 (2005).

[8] Su S., Jiang D. D., Wilkie C. A.: Polybutadiene modified clay and its nanocomposites. Polymer Degradation and Stability, **84**, 279–288 (2003).

[9] Wang K. H., Xu M., Choi Y. S., Chung I. J.: Effect of Aspect Ratio on melt extensional process of maleated polyethylene/clay nanocomposites. Polymer Bulletin, **46**, 499–505 (2001).

[10] Su S., Jiang D. D., Wilkie C. A.: Poly(methyl methacrylate), polypropylene and polyethylene nanocomposite formation by melt blending using novel polymerically modified clay. Polymer Degradation and Stability, **83**, 321–331 (2004).

[11] Zhang J., Jiang D. D., Wilkie C. A.: Polyethylene and polypropylene nanocomposites based upon an oligomerically modifed clay. Thermochinica Acta, **430**, 107–113 (2005).

[12] Zhao C., Qin H., Gong F., Feng M., Zhang S., Yang M.: Mechanical, thermal and flammability properties of polyethylene/clay nanocomposites. Polymer Degradation and Stability, **87**, 183–189 (2005).

[13] Gopakumar T. G., Lee J. A., Kontopoulou M., Parent J. S.: Influence of clay exfoliation on the physical properties of montmorillonite/polyethylene composites. Polymer, **43**, 5483–5491 (2002).

[14] Wang K. H., Choi M. H., Koo C. M., Xu M., Chung I. J., Jang M. C., Choi S. W., Song H.H.: Morphology and physical properties of polyethylene/silicate nanocomposite prepared by melt intercalation. Journal of Polymer Science: Part B: Polymer Physics, **40**, 1454–1463 (2002).

[15] Wang K. H., Koo C. M., Chung I. J.: Physical properties of polyethylene/silicate nanocomposite blown films. Journal of Applied Polymer Science, **89**, 2131–2136 (2002).

[16] Kato M., Okamoto H., Hasegawa N., Tsukigase A., Usuki A.: Preparation and properties of polyethylene-clay hybrids. Polymer Engineering and Science, **43**, 1312–1316 (2003).

[17] Hotta S., Paul D. R.: Nanocomposites formed from linear low density polyethylene and organoclays. Polymer, **45**, 7639–7654 (2004).

[18] Liang G. D., Xu J. T., Bao S. P., Xu W. B.: Polyethylene maleic anhydride grafted polyethylene organic-montmorillonite nanocomposites. I. Preparation, microstructure, and mechanical properties. Journal of Applied Polymer Science, **91**, 3974–3980 (2004).

[19] Zhao C. G., Feng M., Gong F. L., Qin H. L., Yang M. S.: Preparation and characterization of polyethylene-clay nanocomposites by using chlorosilane-modified clay. Journal of Applied Polymer Science, **93**, 676–680 (2004).

[20] Lee J. H., Jung D., Hong C-E., Rhee K. Y., Advani S. G.: Properties of Polyethylene-layered silicate nanocomposites prepared by melt intercalatin with a PP-g-MA compatibilizer. Composites Science and Technology, **65**, 1996–2002 (2005).

[21] Modesti M., Besco S., Lorenzetti A., Zanirato G., Rauli F.: Reinforcing effect of organo-modified layered silicates in high-density polyethylene. Journal of Nanoscience and Nanotechnology, **5**, 958–963 (2005).

[22] Morawiec J., Pawlak A., Slouf M., Galeski A., Piorkowska E., Krasnikowa N.: Preparation and properties of compatibilized LDPE/organo-modified montmorillonite nanocomposites. European Polymer Journal, **41**, 1115–1122 (2005).

[23] Ranade A., Nayak K., Fairbrother D., D'Souza N. A.: Maleated and non maleated polyethylene-montmorillonite layered silicate blown films: creep, dispersion and cristallinity. Polymer, **46**, 7323–7333 (2005).

[24] Tanniru M., Yuan Q., Misra R. D. K.: On significant retention of impact strength in clay-reinforced high-density polyethylene (HDPE) nanocomposites. Polymer, **47**, 2133–2146 (2006).

[25] Truss R. W., Yeow T. K.: Effect of exfoliation and dispersion on the yield behavior of melt-compounded polyethylene-montmorillonite nanocomposites. Jour-

nal of Applied Polymer Science, **100**, 3044–3049 (2006).

[26] Xie Y. C., Yu D. M., Kong J., Fan X. D., Qiao W. Q.: Study on morphology, crystallization behaviors of highly filled maleated polyethylene-layered silicate nanocomposites. Journal of Applied Polymer Science, **100**, 4004–4011 (2006).

[27] Zhong Y., De Kee D.: Morphology and properties of layered silicate-polyethylene nanocomposite blown films. Polymer Engineering and Science, **45**, 469–477 (2005).

[28] Shah R. K., Paul D. R.: Organoclay degradation in melt processed polyethylene nanocomposites. Polymer, **47**, 4075–4084 (2006).

[29] Pegoretti A., Dorigato A., Penati A.: Production and characteization of polyurethane-clay nanocomposites. in 2nd International Symposium on 'Nanostructured and Functional Polymer-based Materials and Nanocomposites'. 2006. Lyon, France.

[30] Fornes T. D., Yoon P. J., Hunter D. L., Keskkula H., Paul D. R.: Effect of organoclay structure on nylon 6 nanocomposite morphology and properties. Polymer, **43**, 5915–5933(2002).

[31] Gianelli W., Ferrara G., Camino G., Pellegatti G., Rosenthal J., Trombini R. C.: Effect of matrix features on polypropylene layered silicate nanocomposites. Polymer, **46**, 7037–7046 (2005).

[32] Shah R. K., Paul D. R.: Organoclay degradation in melt processed polyethylene nanocomposites. Polymer, **47**, 4075–4084 (2006).

[33] Zhai H. B., Xu W. B., Guo H. Y., Zhou Z. F., Shen S. J., Song Q. S.: Preparation and characterization of PE and PE-g-MAH/montmorillonite nanocomposites. European Polymer Journal, **40**, 2539–2545 (2004).

[34] Zhang J., Gupta R. K., Wilkie C. A.: Controlled silylation of montmorillonite and its polyethylene nanocomposites. Polymer, **47**, 4537–4543 (2006).

[35] Crawford R. J.: Plastics engineering. Butterworth-Heinemann, Oxford (UK) (1998).

[36] Lakes R. S.: Viscoelastic solids. CRC Press, Boca Raton (1999).

[37] Ward I. M., Hadley D. W.: An introduction to the mechanical properties of solid polymers. Wiley Chichester (1993).

[38] Siengchin S., Karger-Kocsis J.: Creep behavior of polystyrene/fluorohectorite micro- and nanocomposites. Macromolecular Rapid Communication, **27**, 2090–2094 (2006).

eXPRESS Polymer Letters Vol.1, No.3 (2007) 132–141
Available online at www.expresspolymlett.com
DOI: 10.3144/expresspolymlett.2007.22

Polymerization of acrylamide initiated with Ce(IV)- and $KMnO_4$-mercaptosuccinic acid redox systems in acid-aqueous medium

C. Özeroglu, S. Sezgin*

Department of Chemistry, Faculty of Engineering, Istanbul University, 34320 Avcilar Istanbul, Turkey

Received 28 November 2006; accepted in revised form 21 February 2007

Abstract. By using mercaptosuccinic acid-cerium(IV) sulfate and mercaptosuccinic acid-$KMnO_4$ redox systems in acid aqueous medium, the polymerization of acrylamide monomer was performed at room temperatures. Water soluble acrylamide polymers which contain mercaptosuccinic acid end-groups were synthesized. The dependence of polymerization yield and the molecular weight of polymer on the initiator concentration($n_{MSA} = n_{Ce(IV)}$) at different acid concentrations, polymerization time, temperature, and concentration of sulfuric acid was investigated. The decrease in the initiator concentration resulted in an increase in the molecular weight but a decrease in the yield. The increase of reaction temperature from 20 to 60°C resulted in an increase in the molecular weights and slight decrease of the yield of polymer. Cerium and manganese ions are reduced to Ce(III) and Mn(II) ions respectively in polymerization reaction. The existence of Ce(III) ion bound to polymer was investigated by UV-visible spectrometry and fluorescence measurements. The amount of Mn(II) which is incorporated to the polymer was determined.

Keywords: *polymer synthesis, molecular engineering, mercaptosuccinic acid, cerium(IV) sulfate, redox polymerization, acrylamide*

1. Introduction

$KMnO_4$ and ceric salts-(organic) reducing agent systems in acid-aqueous medium were used for polymerization of vinyl monomers. These methods have also been used for the preparation of graft copolymers of vinyl monomers such as acrylonitrile, methylmethacrylate, acrylic acid or acrylamide [1–15]. In previous studies, water soluble polymers containing amine, hydroxyl, carboxyl, dicarboxylic or amino tri(methylene phosphonic acid) end groups were synthesized by using redox initiator systems [16–23]. The initiator system, especially using mercaptosuccinic acid was used firstly in this study. Unlike other reducing agents used in most previous studies, mercaptosuccinic acid contains S–H group. The formation of $–S^{\bullet}$ radicals are more probable at low temperatures, because of low bonding energy of S–H bond. This gives advantages us to save energy in polymerization process and to obtain polymer with low degree of branching. Moreover if mercaptosuccinic acid is used as a reducing agent, polyacrylamide bearing mercaptosuccinic acid end groups is synthesized. Because of on the presence of this functional group in the polymer, it may also find some practical applications in various industries.

In the present communication, the polymerization of acrylamide monomer initiated by cerium(IV) sulfate-mercaptosuccinic acid and potassium permanganate-mercaptosuccinic acid redox systems was investigated at room temperatures. The effects of initiator concentration($n_{MSA} = n_{Ce(IV)}$), polymer-

---

*Corresponding author, e-mail: ozeroglu@istanbul.edu.tr

ization time, temperature, the concentration of sulfuric acid on the polymerization yields and the molecular weights of polymers were investigated. Water soluble polyacrylamides containing mercaptosuccinic acid end groups were synthesized. Such water soluble polymers prepared with Ce(IV)-organic reducing agent redox system containing amino, hydroxyl, carboxylic and thiol functional groups or end groups seem to be potential sources for the construction of high molecular weight polymers that can be destroyed under physiological conditions due to weakly bound structures occurring in the polymer and to have potential for the preconcentration and separation of some trace elements [24–28].

2. Experimental

Mercaptosuccinic acid(Merck), acrylamide(Merck), cerium(IV) sulfate(Merck) and sulfuric acid(Merck) were used without further treatment. Ce(IV) sulfate, mercaptosuccinic acid and acrylamide are denoted as Ce(IV), MSA and AAm respectively.

Polymerizations were carried out in a round-bottomed flask equipped with a stirrer by adding the calculated amount of Ce(IV) salt or $KMnO_4$ solution to aqueous solution of acrylamide monomer and mercaptosuccinic acid. The oxidants (cerium(IV) sulfate and potassium permanganate) were dissolved in the calculated amount of sulfuric acid solution. The solution volume containing oxidant was kept constant at 20 ml. The total volume of polymerization solution was 100 ml. It was reported that H_2SO_4 was used to increase the solubility of the oxidant and to prevent the hydrolysis of the oxidant. Moreover, the redox reaction between mercaptosuccinic acid and Ce(IV) or $KMnO_4$ salt takes place in acetic medium [1–22, 30–34]. After polymerization was completed, the solution was poured into an excess of acetone to precipitate the raw polymer. In the precipitation of polymers in acetone, volume ratios of acetone to polymer solution were exactly 7/1. The weight of isolated polymer was determined by direct weighting of polyacrylamide dried in air and the yield % was calculated by using Equation (1).

$$\text{Yield}\,[\%] = \frac{\text{weight of isolated polymer}\,[\text{g}]}{\text{weight of monomer}\,[\text{g}]}\cdot 100 \qquad (1)$$

In polymerization reaction, the effects of the initiator concentration ($C_{Ce(IV)} = 1.4\cdot10^{-3}$, $2.8\cdot10^{-3}$, $7\cdot10^{-3}$, $14\cdot10^{-3}$ and $20\cdot10^{-3}$ mol/l) at different acid concentrations, the temperature ($T = 20$, 30, 40, 50 and 60°C), polymerization time ($t = 5$, 10, 30 and 60 minutes) and the concentration of sulfuric acid ($C_{H_2SO_4} = 0.05$, 0.10, 0.20 and 0.40 mol/l) on the yield and molecular weight were examined. The $n_{Ce(IV)}/n_{MSA}$ ratio was kept constant at 1.

It seems from previous investigations, that the formation of radicals on carboxyl groups may be possible [2, 33]. However, the probability of radical formation on carboxyl groups may appear less than that of other radical formation reactions given in Figure 1, due to the formation of acid (proton) influence. It was also described that the redox reactions in the use of thioglycolic acid and 3-mercap-

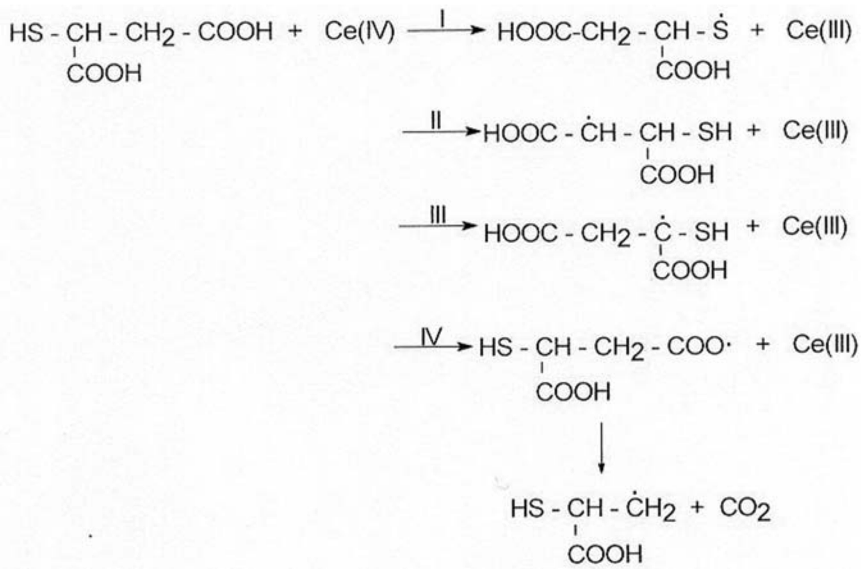

Figure 1. Radical formation reactions occurring between mercaptosuccinic acid and Ce(IV) ions

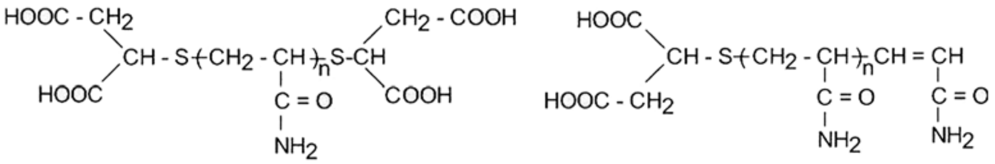

Figure 2. Probable structures of the synthesized polymers

topropionic acid as reducing agents in the redox systems occur at lower temperature, due to low bonding energy of S–H bond [30, 34].

The radical generation is believed to occur by one electron transfer from mercaptosuccinic acid to Ce(IV) according to the reactions given in Figure 1 as reported in the literature [22, 30, 34].

Because of low S–H bonding energy, the formation of free radicals in reaction I in Figure 1 is more likely than other reactions to initiate polymerization of acrylamide and oxidative termination of polymer radicals is also possible by ceric ions [2, 22, 30, 33–36]. For this reason, in the polymerization reaction, water soluble polyacrylamides having more probable structures given below in Figure 2 have been obtained.

Infrared measurements were carried out with ATI Unicam (Mattson 1000) FT-IR spectrometer and the spectra of polymers were determined by KBr disk method. For this purpose, pallets of about 300 mg KBr powder containing finely grained powder of MSA, AAm or PAAm sample(7–8 mg) were made. The FT-IR spectra of MSA, AAm and PAAm synthesized using MSA-Ce(IV) redox system were recorded by ATI Unicam (Mattson 1000) FT-IR spectrometer.

For determination of the viscosity average molecular weight (M_v), the flow time of dilute solution of polyacrylamide with 0.5 g/dl and that of water (the average value of flow times for three measurements was 163±0.2 s for water at 30°C) was measured by an Ubbelohde-level viscometer at 30°C. The intrinsic viscosities ($|\eta|$) of polymer solutions were calculated by using Equation (2) [29–30].

$$|\eta| = \frac{\eta_{sp} + 3\ln(\eta_r)}{4C} \qquad (2)$$

The relative(η_r) and specific(η_{sp}) viscosities were calculated using Equations (3) and (4).

$$\eta_r = \frac{t}{t_0}; \quad \eta_{sp} = \frac{t - t_0}{t_0} = \eta_r - 1 \qquad (3), (4)$$

t_0 and t are the flow times of water and polymer solution of defined volume in Ubbelohde capillary viscometer.

In standard measurements, the solution viscosity is measured in at least three different concentrations and triplicates for extrapolation of the Huggins or Kraemer plots to infinite dilution. However, this method is quite laborious and time consuming.

The molecular weights of polymers were determined by the Mark-Houwink equation (5).

$$|\eta| = K M_v^{\alpha} \qquad (5)$$

Where K and α are constants which are dependent on the solvent, type of polymer and the temperature of system. For polyacrylamide aqueous solution at 30°C, the values of K and α are $6.88 \cdot 10^{-4}$ and 0.66 respectively.

The UV measurements (200–1000 nm) were done using a JASCO V-530 UV/VIS spectrometer equipped with a temperature control attachment.

For fluorescence measurement, PTI QM-4/2003 spectrofluorimeter was used to establish the presence of Ce(III) in the polymer. 75 watt xenon lamp was operated at an excitation wavelength of 260 nm and a slit width of 1 nm

An Analytik Jena Vario 6 AAS, flame atomic absorption spectrometer was used for determining Mn(II) in polymers. Manganese hallow cathode lamps were operated at a wavelength of 297.5 nm and a slit width of 0.2 nm.

3. Result and discussion

In the polymerization of acrylamide initiated by Ce(IV)- mercaptosuccinic acid or $KMnO_4$-mercaptosuccinic acid in acid-aqueous medium, the formation radicals of $-S^{\cdot}$ is energetically most favorable due to low S–H bonding energy. Therefore the polymerization of acrylamide initiated with Ce(IV)-organic reducing agents such as polyamino, amino and carboxylic acids [17–22] requires higher energy, longer time and lower acid concentration than that initiated with Ce(IV)-organic reducing agents containing thiol groups.

The effect of initiator concentration at different acid concentrations ($C_{H_2SO_4}$ = 0.05, 0.10 and 0.20 mol/l) on the molecular weight of polymer and the yield are shown in Figure 3 and 4 respectively. The increase in the initiator concentration at a constant monomer concentration of 0.7 mol/l resulted in a decrease in molecular weight (Figure 3) but an increase in the yield (Figure 4) of polymer which contains mercaptosuccinic acid end-groups.

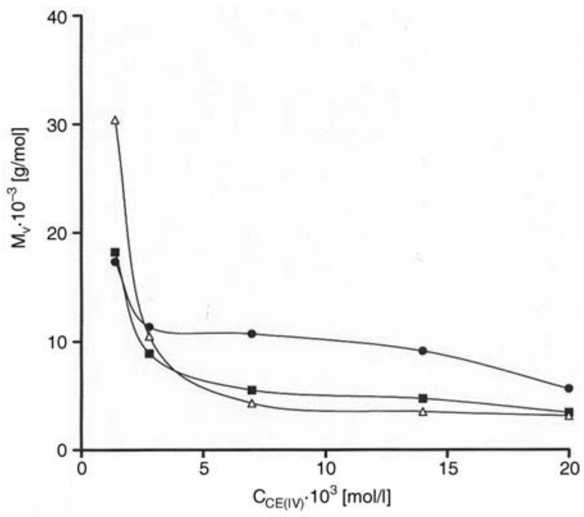

Figure 3. The effect of the initiator concentration on the molecular weight of polymer synthesized by using mercaptosuccinic acid-Ce(IV) redox system at different acid concentrations. $C_{H_2SO_4}$ = 0.05(●), 0.1(■) and 0.2(Δ). C_{AAm} = 0.7 mol/l; T = 30°C; t = 10 min; $n_{Ce(IV)} = n_{MSA}$

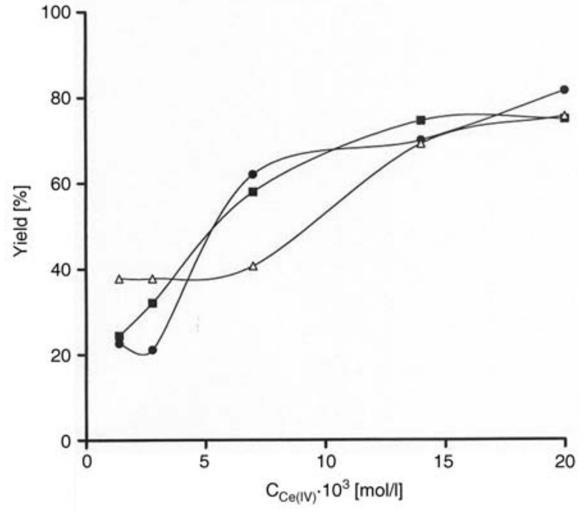

Figure 4. The dependence of polymerization yield on the initiator concentration at different acid concentrations. $C_{H_2SO_4}$ = 0.05(●), 0.1(■) and 0.2(Δ). C_{AAm} = 0.7 mol/l; T = 30°C; t = 10 min; $n_{Ce(IV)} = n_{MSA}$

The increase of the temperature in the polymerization reaction resulted in an increase in the molecular weight of polymer and slight decrease in the yield of polymer (Figure 5). This unexpected result must be because of the side reactions of the primary radicals generated from mercaptosuccinic acid. Those side reactions might be recombination of the initiating primary radicals or any other radical addition to the amide carboxyl etc. Similar unusual behavior has been reported by Lozinsky *et al.* [32] in the polymerization of polyacrylamide initiated with tertiary amine-persulfate redox couple.

The dependence of the yield and molecular weight of polymer on the acid concentration at different

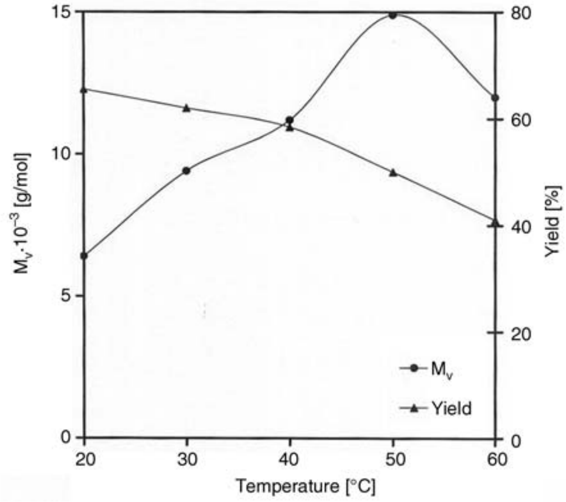

Figure 5. The effect of the temperature on the yield and molecular weight of polymer. C_{AAm} = 0.7 mol/l; $C_{Ce(IV)} = 7 \cdot 10^{-3}$ mol/l; $n_{Ce(IV)} = n_{MSA}$; $C_{H_2SO_4}$ = 0.05 mol/l; t = 10 min

Table 1. The dependence of the yield and the molecular weight of polymer on the acid concentration and the polymerization time. C_{AAm} = 0.7 mol/l; T = 30°C; $n_{Ce(IV)} = n_{MSA}$

$C_{Ce(IV)} \cdot 10^3$ [mol/l]	$C_{H_2SO_4}$ [mol/l]	Polymerization time [min]	Yield [%]	M_v [g/mol]
7.0	0.05	10	62,0	9 400
7.0	0.10	10	57.9	5 500
7.0	0.20	10	40.7	4 300
7.0	0.40	10	66.6	6 450
2.8	0.05	10	21.1	11 350
2.8	0.10	10	32.1	8 900
2.8	0.20	10	37.8	10 500
2.8	0.40	10	52.9	17 600
7.0	0.05	5	62.7	8 650
7.0	0.05	30	74.9	8 500
7.0	0.05	60	64.2	8 100

initiator concentrations and the polymerization time is shown in Table 1. When examining Figure 3 and Table 1, it is seen that the increase in the acid concentration resulted in a decrease in the molecular weight of polymer at higher Ce(IV) concentration. However, at low Ce(IV) concentration, with increasing acid concentration, the molecular weight of polymer increased. No significant change was observed in the molecular weights by extension of polymerization time. Polymerization yield remains constant at around 62–64.2% except for 74.9% of polymerization yield at 30 minutes of polymerization time. We attributed this phenomenon to an oxidation-reduction reaction between mercaptosuccinic acid and oxidant which was completed rapidly during a few minutes in the polymerization of acrylamide monomer in acid-aqueous medium. It was also observed that both colors of oxidants (Ce(IV) and $KMnO_4$) in polymerization reactions disappeared rapidly when their adding were completed.

To determine the acid values of PAAm with carboxyl end-groups synthesized at different initiator concentrations and at constant sulfuric acid concentration(0.10 mol/l), 0.3 g of each polymer was dissolved in distillated water and the total solution volume was 50 ml. The solutions of these polymer containing different amounts of mercaptosuccinic acid as carboxyl end-groups were titrated with 0.1 N NaOH solution by conductometric titration. The titration curves of polymer solutions containing different amounts of mercaptosuccinic acid as end-group by using 0.1 N NaOH solution as titrant were shown in Figure 6. The initial conductivities of polymer solutions, the amount of volume of 0.1 N NaOH solution at neutralization point in titration reaction and the calculated acid values of acrylamide polymers synthesized at various initiator concentrations in the polymerization reactions were given in Table 2. As can be seen from Table 2, the initial conductivities of polymer solutions and acid values of polymers indicated an increase with augmentation of mercaptosuccinic acid in different redox systems at constant sulfuric acid concentration (0.10 mol/l) in polymerization reactions. These results support the idea that polymers synthesized by using of mercaptosuccinic acid as a reducing agent in different redox systems contain carboxyl end-groups

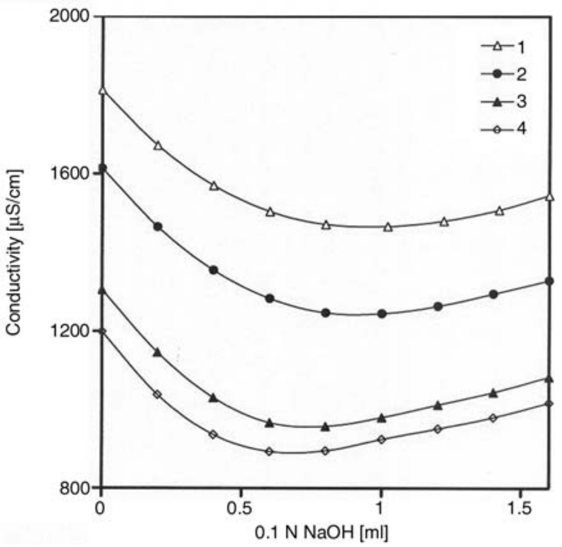

Figure 6. The conductometric titration curves of polymer solutions(0.3 g polymer/50 ml solution in distillated water) obtained at various initiator concentrations. $C_{Ce(IV)} = 20 \cdot 10^{-3}$(1), $14 \cdot 10^{-3}$(2), $7 \cdot 10^{-3}$(3) and $2.8 \cdot 10^{-3}$(4). $C_{AAm} = 0.7$ mol/l; $C_{H_2SO_4} = 0.1$ mol/l; $T = 30°C$; $t = 10$ min; $n_{Ce(IV)} = n_{MSA}$

The UV spectrum of polyacrylamide obtained using Ce(IV)-organic acid or amino acid (with or without thiol group) redox system indicates generally a peak at 254 nm, due to the complex formation between Ce(III) ions and polymer containing reducing agent as end-groups [21–23]. Two peaks at 238 nm and 254 nm were observed in the UV spectrum of acrylamide polymer synthesized using mercaptosuccinic acid –Ce(IV) redox system (Figure 7). It was reported that similar peaks at 238 and 253 nm were obtained in the UV-Visible spectra of polyacrylamides synthesized using Ce(IV)-thioglycolic acid redox system [30]. The obtained spectrophotometric data from peak values at 238 and 254 nm in Figure 5 and the values of Ce(IV) concentrations in polymerization reactions have been listed in Table 3. As can be seen from Figure 5

Table 2. Initial conductivities of polymer solutions(0.3 g polymer/50 solution in water) and acid values of polyacrylamides containing mercaptosuccinic acid end groups synthesized at different initiator concentrations. $C_{AAm} = 0.7$ mol/l; $C_{H_2SO_4} =$ 0.1 mol/l; $T = 30°C$; $t = 10$ min; $n_{Ce(IV)} = n_{MSA}$

$C_{Ce(IV)} \cdot 10^3$ [mol/l]	Initial conductivities of polymer solution [μS/cm]	V_{NaOH} [ml]	n_{COOH} [mmol/g polimer]
20.0	1813	0.62	0.206
14.0	1614	0.58	0.193
7.0	1305	0.52	0.173
2.8	1199	0.45	0.150

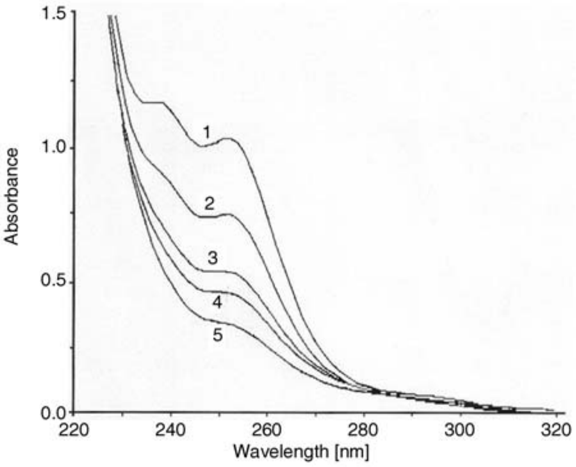

Figure 7. The dependence of absorbance values of polymer solution($C_{polimer} = 0.25$ g/100 ml solution in water) on the initiator concentration in polymerization reaction. $C_{Ce(IV)} = 20\cdot10^{-3}$(1), $14\cdot10^{-3}$(2), $7\cdot10^{-3}$(3), $2.8\cdot10^{-3}$(4) and $1.4\cdot10^{-3}$(5); $C_{AAm} = 0.7$ mol/l; $C_{H_2SO_4} = 0.1$ mol/l; $T = 30°C$; $t = 10$ min; $n_{Ce(IV)} = n_{MSA}$

Table 3. The relation between the absorbance values of polymer solutions ($C_{polimer} = 0.25$ g polymer/100 ml solution in water) measured at 238 nm and 254 nm and the initiator concentration in polymerization reaction at 30°C. $C_{AAm} = 0.7$ mol/l; $C_{H_2SO_4} = 0.1$ mol/l; $n_{Ce(IV)} = n_{MSA}$

$C_{Ce(IV)}\cdot10^3$ [mol/l]	Absorbance values at 254 nm	Absorbance values at 238 nm
20.0	1.013	1.168
14.0	0.733	0.908
7.0	0.523	0.714
2.8	0.466	0.640
1.4	0.332	0.561

and Table 3, the decrease in the initiator concentration in the polymerization reaction led to a decrease in the absorbance values of polyacrylamide solutions (0.25 g polymer/100 ml solution in water) at 238 nm and 254 nm. Since, polyacrylamide itself does not represent any absorption within this range, the observed adsorption bands indicates the presence of cerium(III) salt retention in free form or bonded to the polymer.

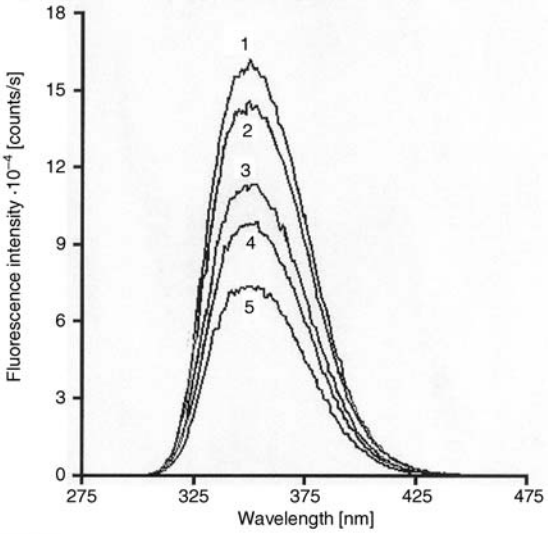

Figure 8. The fluorescence curves of polyacrylamide solutions($C_{polimer} = 0.25$ g polymer/100 ml solution in water) synthesized at various initiator concentrations. $C_{Ce(IV)} = 20\cdot10^{-3}$(1), $14\cdot10^{-3}$(2), $7\cdot10^{-3}$(3), $2.8\cdot10^{-3}$(4) and $1.4\cdot10^{-3}$(5); excitation wavelength = 260 nm; slit width=1 nm; $C_{H_2SO_4} = 0.1$ mol/l; $C_{AAm} = 0.7$ mol/l; $T = 30°C$; $t = 10$ min; $n_{Ce(IV)} = n_{MSA}$

Table 4. The effect of the initiator concentration in the polymerization reaction on the fluorescence intensity of polymer solution ($C_{polimer} = 0.25$ g polymer/ 100 ml solution in water; excitation wavelength = 260 nm; slit width = 1 nm) at 351 nm. $C_{H_2SO_4} = 0.1$ mol/l; $C_{AAm} = 0.7$ mol/l; $T = 30°C$; $t = 10$ min; $n_{Ce(IV)} = n_{MSA}$

$C_{Ce(IV)}\cdot10^3$ [mol/l]	Fluorescence intensity$\cdot10^{-4}$ at 351 nm [counts/s]
20.0	15.93
14.0	14.24
7.0	11.34
2.8	7.56
1.4	7.38

Unlike the fluorescence curve of homopolyacrylamide, the fluorescence curves of polyacrylamide obtained using mercaptosuccinic acid-Ce(IV) redox system show a peak at 351 nm (Figure 8). The peak values at 351 nm obtained from fluorescence curves of polymer solution indicated in Figure 8 and the values of different initiator concentrations in polymerization reaction were listed in Table 4. It was observed that with increasing Ce(IV) content in the polymerization reaction, the fluorescence intensity of polymer solution (0.25 g polymer/100 ml solution in water) at 351 nm increased. Ce(IV) reduces to Ce(III) in polymerization reaction and this indicates that reduced Ce(III) ions are absorbed by the polymer.

The FT-IR spectra of acrylamide (AAm), mercaptosuccinic acid (MSA) and polyacrylamide (PAAm) containing mercaptosuccinic acid end-groups were given in Figure 9. As can be seen from Figure 9, the band at 3400 which can be assigned to symmetrical and asymmetrical stretching of N–H group

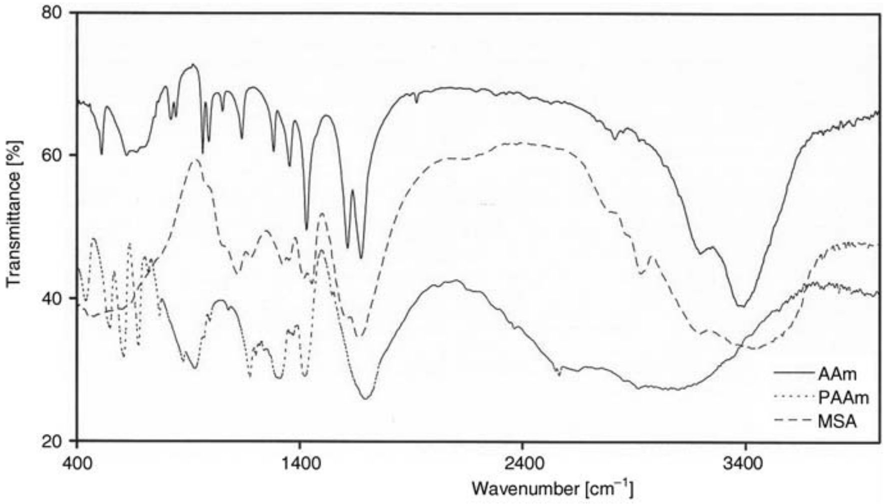

Figure 9. FT-IR spectra of acrylamide (AAm), mercaptosuccinic acid (MSA) and polyacrylamide (PAAm) obtained using mercaptosuccinic acid-cerium(IV) sulfate redox system

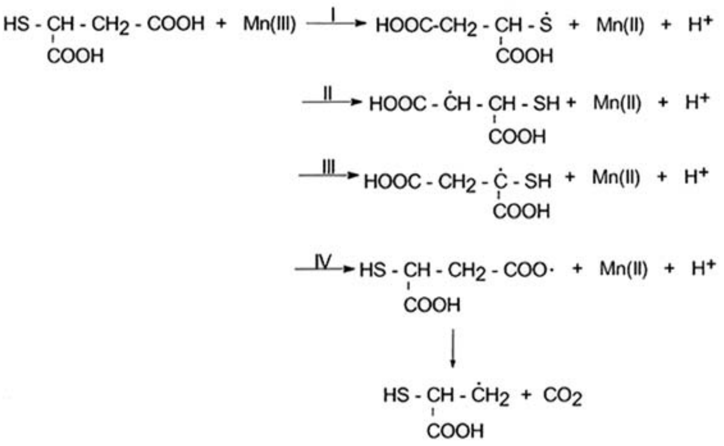

Figure 10. Radical generation reactions occurring between mercaptosuccinic acid and Mn(III) ions

observed in the FT-IR spectrum of acrylamide monomer was has been observed to shift to a band at 3450 cm^{-1} in the spectrum of polyacrylamide. The characteristic C=O stretching vibration bands of amide and acid groups have been observed at 1680 and 1720 cm^{-1} respectively. The peaks observed at 1620 cm^{-1} which have been attributed to the $-CH=CH_2$ group observed in the FT-IR spectrum of acrylamide monomer disappeared in the FT-IR spectrum of polyacrylamide. The band at 1430 cm^{-1} indicates O–H bending, the existence of C–O stretching in the plane of C–O–H bending in mercaptosuccinic acid and N–H stretching in acrylamide and polyacrylamide. There are also peaks at 1280 and 1180–1190 cm^{-1} which are seen in the FT-IR spectra of acrylamide and polyacrylamide. These peaks belong to N-–H stretching of amide groups in acrylamide and O–H bending respectively which are observed in the FT-IR spectra of mercaptosuccinic acid and polyacrylamide containing mercaptosuccinic acid end-groups. Moreover the peaks in the spectrum presented for polyacryamide can arise due to metal ions absorbed in the polymer.

Potassium permanganate in spite of being a powerful and versatile oxidant is incapable of initiating vinyl polymerization by itself in dark. If, however, the polymerization medium is sufficiently acidic to dissolve the manganese dioxide produced by the interaction of vinyl monomer with permanganate, polymerization can be initiated by adding reducing agent and manganese dioxide dissolves in carboxylic or hydroxyl carboxylic acids, producing highly reactive Mn(III) ions [2, 33]. Both Mn(IV) and Mn(III) ions formed can be react with mercaptosuccinic acid to produce radicals for the polymerization of acrylamide monomer in acid-aqueous medium. The radical generation mechanism in this redox reaction occurring between Mn(III) ions and mercaptosuccinic acid can be given as in Figure 10.

As explained in the mercaptosuccinic acid-Ce(IV) redox reaction defined in this paper, the formation of free radicals given in the reaction I of Figure 10 is more probable than other reactions to initiate polymerization of acrylamide monomer, due to low S–H bonding energy. As described in previous investigations, oxidative termination of polymeric radicals is also possible by Mn(III) or Mn(IV) ions [2, 22, 30, 33–36] and polyacrylamides having chemical structures given in Figure 2 can be obtained in the polymerization of acrylamide monomer initiated with $KMnO_4$-mercaptosuccinic acid redox system in acid aqueous medium.

Using mercaptosuccinic acid-$KMnO_4$ redox system, polymerization of acrylamide monomer was performed at different initiator concentrations at 30°C. It was observed that the increase of potassium permanganate concentration in polymerization reaction resulted in an increase in the yield but a decrease in molecular weight of polymer (Table 5). It is reported that manganese dioxide is produced by the interaction of vinyl monomer with permanganate and then manganese dioxide dissolves in acid producing highly reactive Mn(III) ions [2, 33]. Both Mn(IV) or Mn(III) ions reduced to Mn(II) ions during the polymerization reaction. The Mn(II) species that occur at the end of polymerization reaction are absorbed by the polymer [20–22]. The dependence of the concentration of Mn(II) which is incorporated into the polymer on the initiator concentration in the polymerization reaction is given in Figure 11. It is seen that the amount of Mn(II) bound to the polymer changes with the initial concentration of permanganate.

Table 5. The effect of the initiator concentration on the yield and molecular weight of acrylamide polymer. $C_{H_2SO_4} = 0.05$ mol/l; $C_{AAm} = 0.7$ mol/l; $T = 30°C$; $t = 15$ min

$C_{KMnO_4}·10^3$ [mol/l]	Yield [%]	M_v [g/mol]
1.4	18.1	56 600
2.8	25.6	26 800
7.0	36.6	12 850
20.0	37.6	8 000

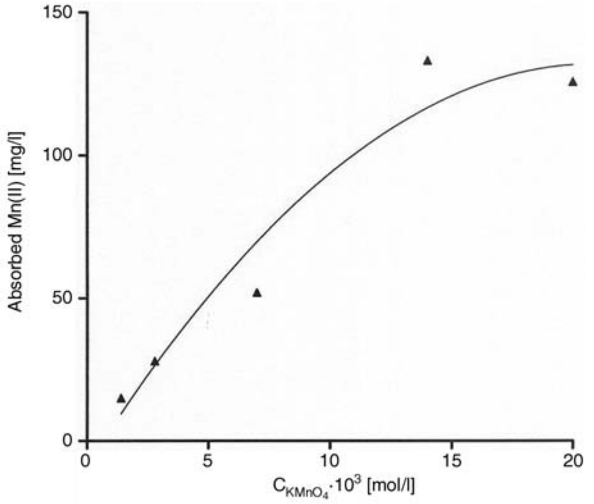

Figure 11. The relation between the concentration of Mn(II) bounded to polymer and the initiator concentration at the beginning of polymerization reaction. $T = 30°C$; $t = 10$ min; $C_{AAm} = 0.7$ mol/l; $C_{H_2SO_4} = 0.05$ mol/l; $n_{KMnO_4} = n_{MSA}$, $C_{polimer} = 0.25$ g/dl

4. Conclusions

In this study, the effects of temperature, polymerization time, sulfuric acid concentration and initiator concentration on the yield and molecular weight of polymer were investigated. The results indicate that this redox system is very convenient to initiate acrylamide polymerization at room temperature. The polymerization of acrylamide using mercaptosuccinic acid-Ce(IV) or $KMnO_4$ redox system in acid aqueous medium was performed at room temperatures. In the polymerization of acrylamide initiated by Ce(IV)- mercaptosuccinic acid or $KMnO_4$-mercaptosuccinic acid redox system in acid-aqueous medium, the formation radicals of $–S^•$ is energetically most favorable due to low S–H bonding energy. As a result, mercaptosuccinic acid is a convenient radical source for generation of radicals to initiate acrylamide polymerization at room temperature.

References

[1] Launer H. F., Yost D. M.: The kinetics of the reaction between potassium permanganate and oxalic acid. Journal of the American Chemical Society, **56**, 2571–2577 (1934).

[2] Misra G. S., Bajpai U. D. N.: Redox polymerization. Progress in Polymer Science, **8**, 61–131 (1982).

[3] Narita H., Maghida S.: The polymerization of acrylamide initiated with ceric ion. Die Angewandte Makromolekulare Chemie, **97**, 209–215 (1966).

[4] Pramanik D., Chaterjee A. K.: Mechanistic studies on ceric-thiourea-initiated polymerization in acid aqueous media from end group analysis. Journal of Polymer Science Part A-Polymer Chemistry, **18,** 311–319 (1980).

[5] Özeroglu C., Yalçinyuva T.: Oxidative polymerization of methyl methacrylate in acid-aqueous medium. Polymer-plastics Technology and Engineering, **43**, 731–743 (2004).

[6] Biçak N., Özeroglu C.: Low temperature initiation by methylene bis(diethyl malonate)-Ce(IV) redox system in organic solvents. European Polymer Journal, **37**, 2393–2395 (2001).

[7] Sui K. Y., Gu L. X.: Preparation and characterization of amplihilic block copolymer of polyacrylonitrile-block-poly(ethylene oxide). Journal of Applied Polymer Science, **89**, 1753–1759 (2003).

[8] Saraç A. S., Özkara. Ş., Ustamehmetoglu B., Sezer E.: Controlled electroinduced polymerization of methyl meyhacrylate in the presence of catalytic amount of Ce(IV). Journal of Macromolecular Science Part A: Pure and Applied Chemistry, **40**, 193–207 (2003).

[9] Ananthanarayanan V. S., Santappa M.: Kinetics of vinyl polymerization initiated by ceric ion in aqueous solution. Journal of Applied Polymer Science, **9**, 2437–2447 (1965).

[10] Mino G., Kaizerman S., Rasmussen E.: The polymerization of acrylamide initiated by ceric nitrate-3-chloro-1-propanol redox system. Journal of Polymer Science, **38**, 393–401 (1959).

[11] Subramaniun S. V., Santappa M.: Vinyl polymerization initiated by ceric ion-reducing agent system in sulfuric acid media. Journal of Polymer Science Part A-Polymer Chemistry, **6**, 493–504 (1968).

[12] Palit S. R., Konar R. S.: Permanganate-oxalic acid as a initiator of acrylonitrile polymerization in aqueous media: (III) Kinetics and degree of polymerization. Journal of Polymer Science Part A-Polymer Chemistry, **2**, 1731–1748 (1964).

[13] Palit S. R., Konar R. S.: Permanganate-$H_2C_2O_4$ as an initiator in aquelus media: (II) The kinetics and degree of polymerization. Journal of Polymer Science, **58**, 85–102 (1962).

[14] Misra G. S., Narain H.: Aqueous polymerization of acrylic acid initiated by potassium permanganate-oxalic acid redox system. Die Makromoleculare Chemie, **113**, 85–94 (1968).

[15] Hussain M. M., Gupta A.: Effect of some additions on the aqueous polymerization of acrylamide initiated by permanganate-oxalic acid redox system. Die Makromoleculare Chemie, **178**, 29–36 (1977).

[16] Akar A., Öz N.: Low molecular weight poly(acrylic acid) with nitrilo di(methylenephosponic acid) chain ends for scale inhibition. Die Angewandte Makromolekulare Chemie, **273**, 12–14 (1999).

[17] Saraç A. S., Erbil C., Soydan A. B.: Polymerization of acrylamide initiated with electrogenerated cerium(IV) in the presence of EDTA. Journal of Applied Polymer Science, **44**, 877–881 (1992).

[18] Erbil C., Cin C., Soydan A. B., Saraç A. S.: Polyaminocarboxylic acids-Ce(IV) redox systems as an initiator in acrylamide polymerization. Journal of Applied Polymer Science, **47**, 1643–1648 (1993).

[19] Saraç A. S., Başak A. H., Soydan A. B., Akar A.: Polymerization of acrylamide by electrolytically generated Ce(IV)-organic acid redox system. Die Angewandte Makromolekulare Chemie, **198**, 191–198 (1992).

[20] Özeroglu C., Güney O., Saraç A. S., Mustafaev M. I.: The polymerization of acrylamide initiated with Ce(IV) and $KMnO_4$ redox systems in the presence of glycine. Journal of Applied Polymer Science, **60**, 759–765 (1996).

[21] Özeroglu C., Güney O., Mustafaev M. I.: Oxidative polymerization of acrylamide in the presence of L-threonine. Die Angewandte Makromolekulare Chemie, **249**, 1–9 (1997).

[22] Özeroglu C., Kurtoglu A. E.: The synthesis and characterization of acrylamide polymer containing R-(+)-cystein end groups. European Polymer Journal, **37**, 1053–1059 (2001).

[23] Ustamehmetoglu B., Diler Z. I., Saraç A. S.: Chemical polymerization of acrylamide initiated with Ce(IV)-dicarboxylic acid redox system: effect of chain length between the carboxyl groups. International Journal of Polymer Analysis and Characterization, **7**, 263–272 (2002).

[24] Saraç A. S., Özeroglu C., Mustafaev M. I.: The ternary complexes of bovine serum albumin and polyacrylamide derivatives in the presence of copper ions in neutral water. Journal of Bioactive and Compatible Polymers, **10**, 121–134 (1995).

[25] Özeroglu C., Namazova N., Mustafaev M. I., Saraç A. S.: The complex formation between polyacrylamide containing glycine end groups and bovine serum albumin in the presence of copper(II) in neutral aqueous water. Colloid and Polymer Science, **274**, 418–427 (1996).

[26] Petrov R. V., Mustafaev M. I., Norimov A. Sh.: Physicochemical criteria for the constraction of artificial immunomodulators and immunogens on the basis of polyelectrolyte complexes. Sov. Med. Rev. D. Immunol., pp. 1–13. Harwood Academic Publisher GmbH. London UK (1992).

[27] Özcan M., Akman S., Özeroglu C.: The use of water soluble polymers for the preconcentration and separation of copper, lead and chromium prior to their determination by graphite furnace atomic absorption spectrometry. Analytical Letters, **35**, 1075–1083 (2002).

[28] Özcan M., Akman S., Erbil C., Saraç A. S.: Determination of copper, chromium, manganese and zinc by graphite furnace atomic absorption spectrometry after separation on polyacrylamide modified with nitriloacetic acid. Fresenius' Journal of Analytical Chemistry, **355**, 665–666 (1996).

[29] Chuah H. H., Lin-Vien D., Soni U.: Poly(trimethylene terephthalate) molecular weight and Mark-Houwink equation. Polymer, **42**, 7137–7139 (2001).

[30] Özeroglu C., Erdogan S.: Oxidative polymerization of acrylamide in the presence of thioglycolic acid.

Central European Journal of Chemistry, **3**, 705–720 (2005).

[31] Tsubokawa N., Maruyama K., Sone Y., Shimomura M.: Graft polymerization of acrylamide from ultra silica particles by use of a redox system consisting of ceric ion and reducing groups on the surface. Polymer Journal, **21**, 475–481 (1989).

[32] Lozinsky V. I., Ivanov R. V., Kalinina E. V., Timofeeva G. I., Khoklov A. R.: Redox-initiated polymerization of acrylamide in moderately frozen water solutions. Macromolecular Rapid Communications, **22**, 1441–1446 (2001).

[33] Saraç A. S.: Redox polymerization. Progress in Polymer Science, **24**, 1149–1204 (1999).

[34] Özeroglu C., Özduganci C.: Low temperature initiation by 3-mercaptopropionic acid-Ce(IV) or -$KMnO_4$ redox system for polymerization of acrylamide monomer. Polymer-plastics Technology and Engineering, **45**, 549–554 (2006).

[35] Saha S. K., Chaudhuri A. K.: Effect of amines on ceric ion-initiated polymerization of vinyl monomers. II. Polymerization of acrylonitrile by ceric ion in the presence of various substituted amines. Journal of Polymer Science Part A-Polymer Chemistry, **10**, 797–808 (1972).

[36] Patra M., Sinha B. K.:Acrylamide polymerization initiated with the redox system Ce(IV)-cyclohexanone in miceller phase: A kinetic study. Macromolecular Chemistry and Physics, **199**, 311–317 (1998).

eXPRESS Polymer Letters Vol.1, No.3 (2007) 142–149
Available online at www.expresspolymlett.com
DOI: 10.3144/expresspolymlett.2007.23

Waterborne polyurethane single-ion electrolyte from aliphatic diisocyanate and various molecular length of polyethylene glycol

C-H. Yang[*1], *W-C. Lin*[2], *F-J. Liu*[3]

[1]Department of Chemical and Materials Engineering, National University of Kaohsiung, Kaohsiung 811, Taiwan
[2]Department of Environmental Engineering, Kun Shan University, Tainan 710, Taiwan
[3]Department of Chemical Engineering, National United University, Miaoli 360, Taiwan

Received 3 November 2006; accepted in revised form 24 February 2007

Abstract. The waterborne polyurethane (WPU) dispersions from the reaction of cycloaliphatic diisocyanates [4,4'-methylenebis(cyclohexyl isocyanate) ($H_{12}MDI$) and isophorone diisocyanate (IPDI)] and polyethylene glycol (PEG) with various molecular lengths were synthesized using our modified acetone process. Differetial scanning calorimeter (DSC) and Fourier transform infrared spectroscopy (FTIR) were utilized to characterize WPU films for the behavior of their crystallinity and H-bonding of WPU films. The T_g value of WPU increases with increasing the molecular length of PEG, whereas the T_m of WPU decreases with increasing PEG length. Alternating current (AC) impedance experiments were performed to determine the ionic conductivities of WPU films. The WPU gel electrolytes exhibits an ionic conductivity as high as ~10^{-5} S/cm at room temperature.

Keywords: *polymer gels, waterborne polyurethane electrolyte, single ion, polyethylene glycol*

1. Introduction

Solid polymer electrolytes have received much interest because of their use in lithium ion polymer batteries. Most of the researchers have concentrated on designing novel polymer materials possessing high ionic conductivity, good mechanical properties as well as thermal stability for practical applications [1–3]. Polyether-based electrolytes showed features such as good adherence to electrodes and the ability to solvate many inorganic salts. Ionic conductive polymers such as complexes of poly(ethylene oxide) (PEO) and lithium salts, which showed high ionic conductivity of 10^{-4} to 10^{-3} S/cm at high temperature were characterized by a bi-ion transport mechanism [4, 5]. The disadvantage of these materials is the significant decrease in ionic conductivity using direct current polarization. Therefore, an ionic conductive polymer with single-ion transport mechanism is required for a number of applications. In general, the ionic conductivity of single-ion transport materials is lower than that of the bi-ion transport materials. Several ionic conductive polymers have been characterized by a single-ion transport mechanism [6]. Most of them are polyblends of polymer and polyether or copolymers synthesized from polymers with low molecular weight of polyether. Polyblend electrolytes show poor mechanic properties, while copolymer electrolytes have low conductivity [7].

It is conceivable that ionic transport exists in the amorphous phase of polymers whereas nonconducting behavior is found in the crystalline phase [8]. Thus, to design an excellent polymer elec-

---

[*] Corresponding author, e-mail: yangch@nuk.edu.tw

trolyte, the crystallinity of the polymer should be decreased, as well as adequate mechanical properties should be maintained for applications. However, PEO is a semicrystalline polymer, possessing both amorphous and crystalline phases at room temperature. Hence, considerable ionic conductivity in PEO-based polymers can only be obtained at high temperature [9]. Knowing this, in designing a novel polymer of similar PEO structure, it is reasonable to react PEG with diisocyanate to form PEG-based polyurethane (PU), because PU polymer possesses high tensile strength, elasticity as well as low crystallinity. In our laboratory, a series of studies [10–14] have been performed for the polymer electrolytes on the basis of waterborne polyurethane (WPU).

Polyurethanes are composed of polyether or polyester soft segment and a diisocyanate-based hard segment, which can be characterized by a two-phase morphology [13]. The phase separation is due to the fact that the hard and soft phases are immiscible and leads to the formation of a hard-segment domain, a soft-segment matrix, and an ill-defined inter-phase. The hard-segment domains act as physical cross-links and filler particles to the soft segment matrix. The domain formation is derived from the intermolecular hydrogen bonding between the hard-hard segments of urethane or urea linkages. The hydrogen bonding is characterized by a frequency shift to the values lower than those corresponding to the free groups (i.e. no hydrogen bonding) in the spectrum of FTIR. Meanwhile, the extent of the frequency shift is usually used as an estimate of hydrogen-bonding strength. Particularly for polyether-based PUs, the fraction of the hydrogen-bonded carbonyls is defined by a hard-hard segment hydrogen bond (N–H•••O=C bond), which was employed to evaluate the extent of phase separation. On the other hand, the fraction of the hydrogen-bonded ether oxygen (N–H•••O–) represents the extent of phase mixing between hard and soft segments.

To clarify the effects of PEG molecular length and different kinds of cycloaliphatic diisocyanates on the polymer electrolyte, PEG-based WPU electrolytes were extended from the previous [12] to others by using various molecular weights of PEG as soft segments and two kinds of cycloaliphatic diisocyanates [4,4'-methylenebis(cyclohexyl isocyanate) ($H_{12}MDI$) and isophorone diisocyanate (IPDI)] as hard segments without adding the diol chain extender DMPA (dimethyolpropionic acid). By using FTIR, DSC, and impedance spectroscopy (IS), we investigate the effects of PEG molecular weight and kinds of diisocyanates on phase variation, morphology characteristics and bulk conductivity of these WPU electrolytes.

2. Experimental Section

2.1. Materials

PEG (M_w = 1000, 2000, 3000 and 4000, Showa) used as the soft segment was dried at 80°C in a vacuum oven for 24 h. IPDI (Lancaster) and $H_{12}MDI$ (Wako) were used as hard segment without further treatment. Propylene carbonate (PC) (Aldrich) was distilled at low pressure and stored over 3 Å molecular sieves before use. Acetone (Tedia) was immersed in 4 Å molecular sieves for more than one week before use. Di-n-butyltin(IV) dilaurate (DBTDL) (Wako), ehylenediamine (EDA) (Merck), and butane sultone (BS) (Aldrich) were used without further treatment.

2.2. Synthesis of WPU dispersions

Two series of WPU dispersions were prepared through our modified acetone process [1] with NCO/OH = 1.5 using polyaddition of two diisocyanates ($H_{12}MDI$ and IPDI) to various molecular weights of PEG. PEG was added to the reactor and heated to 50°C. Diisocyanates and DBTDL were then added and reacted at 85°C under nitrogen atmosphere for 6 h. To the final NCO-terminal PU prepolymer was added a suitable amount of acetone. The chain extender was prepared as follows [1]: Ethylenediamine (6.0 g; 0.1 mol) was added drop-wise to a solution of butane sultone (13.6 g; 0.1 mol) and H_2O (25 g). The resulting mixture was heated at 60 to 70°C for 30 min, then cooled to room temperature, after which LiOH (1.9 g; 0.1 mol) was added. The chain extender was added immediately to the freshly prepared NCO-terminated PU prepolymer solution with the [NCO]/[NH_2] ratio of 1.0. The ratio of [Li^+]/[EO] (where EO is the concentration of ethylene oxide units in WPU) was kept at 0.005. The resulting mixture was then heated at phase-inversion temperature of 50°C. Doubly distilled water was added to above PU solutions at agitation rate and water addition rate of 200 rev/min and 2.0 ml/min, respectively.

An aqueous dispersion of about 30 wt% solids was obtained upon removal of acetone by rotary vacuum evaporation.

2.3. Film preparation

The films from the solvent evaporation method were obtained by casting WPU dispersion solution on a Teflon disk, followed by drying at 45°C for 2 days. The films were then removed to a glove box further drying. Before all tests on these films, the water content of the films was determined to be around 10 ppm using a Karl Fisher moisture titrator (MKC-210, Kyoto Electronics, Japan) for the film extracted solvent (acetone).

2.4. Ac impedance measurement

Impedance analysis of the polymer electrolyte was performed using a CMS300 EIS system (Gamry Instrument, USA) with SR810 DSP lock-in amplifier (Standard Research System, USA) under an oscillation potential of 10 mV from 100 kHz to 0.1 Hz. The WPU films or their corresponding gel electrolytes were sandwiched by two stainless steel SS304) blocking electrodes for conductivity tests.

2.5. DSC measurement

Thermal analysis of WPU films was carried out using Du Pont system DSC (Du Pont 910, USA) with a temperature range from –100 to 100°C at a heating rate of 10°C/min under nitrogen purging.

2.6. FTIR spectroscopy

The samples for infrared analysis were prepared by casting 1% (w/v) WPU solution, acetone as solvent, directly on KBr pellets and drying at 120°C in a vacuum oven for 24 h. Infrared spectra were obtained with a Fourier Transform IR spectrophotometer (Nicolet FTIR-550) and recorded by averaging 64 scans at a resolution of 4 cm^{-1}.

3. Results and discussion

3.1. DSC analysis

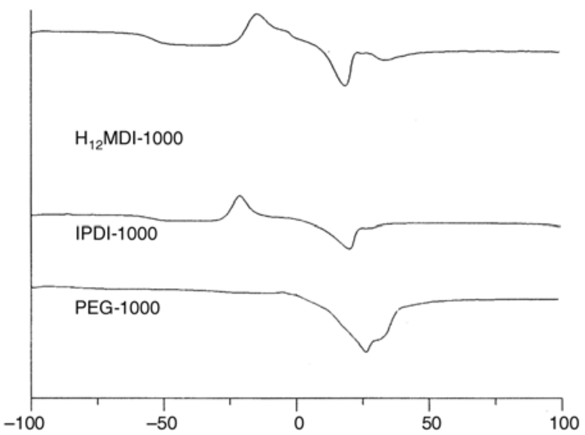

Figure 1. DSC thermograms of WPU films with PEG-1000 samples at a heating rate of 10°C/min

Table 1. Phase-transition characteristics of PEG-based WPU films

Film	T_g [°C]	T_m [°C]	ΔT/S [°C/mol]	ΔT/ΔC [°C/mg/g WPU]
PEG-1000	–79	26	–	–
PEG-2000	–76	51	–	–
PEG-3000	–72	58	–	–
PEG-4000	–68	59	–	–
IPDI-1000[a]	–62	20	22.67	2.39
IPDI-2000	–59	47	19.84	4.17
IPDI-3000	–52	48	22.22	7.02
IPDI-4000	–49	52	20.58	8.67
H_{12}MDI-1000[b]	–59	20	27.86	2.93
H_{12}MDI-2000	–57	48	22.73	4.79
H_{12}MDI-3000	–55	53	19.23	6.07
H_{12}MDI-4000	–53	54	16.47	6.94

[a] waterborne polyurethanes based on the copolymers of IPDI and PEG, numbers represent the molecular weight of PEG.

[b] waterborne polyurethanes based on the copolymers of H_{12}MDI and PEG, numbers represent the molecular weight of PEG.

Figure 1 shows the DSC thermograms of PEG-1000, IPDI-1000 (WPU obtained from the copolymer of IPDI and PEG-1000) and H_{12}MDI-1000 (WPU obtained from the copolymer of H_{12}MDI and PEG-1000) samples, indicating crystallinity for H_{12}MDI-1000 and IPDI-1000 samples as compared PEG-1000 sample. Meanwhile, a soft-segment T_m of these samples was readily observed. A series of the soft-segment T_g and T_m are listed in Table 1. Note that the values of T_g and T_m of PEG increase with increasing molecular weight. And, the values of T_g increase with adding IPDI and H_{12}MDI, respectively, in the WPU polymers. This reflects two effects: First, the addition of lithium salt increases T_g. Second, the segregation of between soft segment and hard segment occurred in these WPUs. For these investigated polymers, the effect of lithium salt on the polyether soft-segment T_g is significant in the PEG-based WPUs. This indicates that the solvation of the lithium cation by the PEG soft-segment partially arrests the local motion of the polymer segment through the formation of transient cross-links, leading to an increase in the soft-segment T_g. By normalizing the T_g data against unit salt concentration for these WPU films, the $\Delta T_g/\Delta C$ was calculated at each measurement and which are listed in Table 1. It is obvious that the value of $\Delta T_g/\Delta C$ increases with increasing PEG molecular length in the WPUs. This result reflects that the formation of transient cross-links between lithium cation and PEG soft-segment increases with increasing the molecular weight of PEG. This arises from the higher content of ethylene oxide (EO) per gram of WPU with the higher molecular weight of PEG. Furthermore, the specific variation of T_g is defined as $\Delta T_g/S$, where S is the soft content, and is also listed in Table 1. It is interesting that these values remain around 20.0 for IPDI-based WPUs, but the value decreases with increasing the length of PEG molecules for H_{12}MDI-based WPUs. This may be because the strength of H-bonding decreases with increasing PEG length in H_{12}MDI-based WPUs (see below). In contrast, the values of T_m decrease with adding IPDI and H_{12}MDI, respectively, in WPUs. These results indicate that the polymers have a certain degree of hard- and soft-segment mixing. The decrease of soft-segment T_m values for these investigated polymers was observed in the range of 5–10°C. In comparison with both of T_g increase and T_m decrease of these WPU polymers, it is obvious that the segregation of between soft- and hard-segments is more significant than the hard- and soft-segment mixing. This result is very different from that with the addition of DMPA content in WPU polymers [12]; the latter implies that the degree of mixing of hard- and soft- segments can be enhanced by the addition of DMPA. In addition, note in Figure 1 that the devitrification exists in both IPDI- and H_{12}MDI-based WPUs, but occurring at exotherm and is followed by an endotherm at a higher temperature that corresponds to the melting of these crystals (IPDI- and H_{12}MDI-based WPUs). This suggests that there should exist a nucleating phase of crystal structure in these WPU polymers during temperature scanning. After nucleation, crystal growth rates are small because the glass phase is heated to a higher temperature, at which crystal growth occurs on the surface of the existing nuclei. Because there is a large number of nuclei present, distributed throughout the bulk of the glass, each can grow by only a small amount until it impringes on neighboring nuclei. It is noteworthy that the devitrification cannot be observed in both of pure PEG and high DMPA-introducing WPUs [12]. Moreover, the devitrification temperature of H_{12}MDI-based WPUs is generally higher than that of IPDI-based WPUs; this result could be related to the H-bonding between hard-hard and hard-soft segments.

3.2. Evaluation of FTIR spectra

In this study, the addition of different PEG molecular weight was achieved by keeping constant NCO/OH ratio of 1.5 in the WPU chain. Therefore, the content of lithium salt (LiOH) decreases with increasing the molecular weight of PEG because the chain extension was completed with the residual NCO/NH_2 ratio of 1.0. A typical FTIR spectrum is shown in Figure 2. Four main regions are presented: (i) 3000–3600 cm^{-1} N–H stretching, a broad absorption band of the N–H region was observed; (ii) 1600–1750 cm^{-1} C=O stretching, the carbonyl stretching absorption band was observed as two peaks. The higher frequency at around 1700 cm^{-1} was assigned to free (i.e., not H-bonded) carbonyl stretching whilst the peak at around 1600 cm^{-1} was attributed to H-bonded carbonyl stretching; (iii) 1500–1600 cm^{-1} (–COO) stretching, characteristic of the urethane group; (iv) 1000–1150 cm^{-1} C–O–C stretching, the ether oxygen of the soft segment.

FTIR spectra have demonstrated H-bonding in PU [12, 15]; the strength of the H-bonding was measured by frequency shifts to values lower than those observed when these groups are free. The N–H group could form hard-hard segment H-bonding with the carbonyl oxygen and hard-soft segment

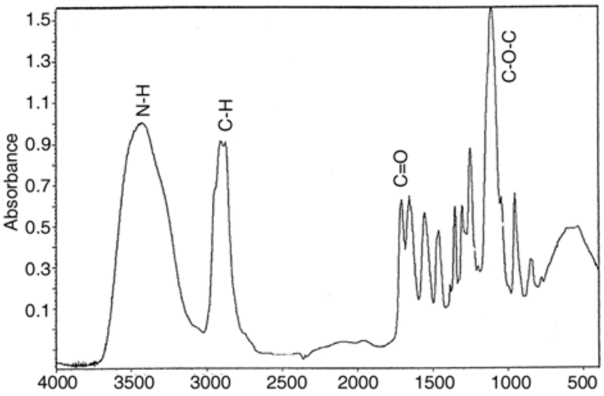

Figure 2. Typical FTIR spectrum of IPDI-1000 WPU film

H–bonding with the ether oxygen. In general, the strength of hard-hard segment H-bonding is stronger than that of hard-soft segment H-bonding [7]. Deconvolution of the N–H stretching region was done and the best fits were obtained using a Gaussian-Lorentzian sum as seen in Figure 3. This indicates that the higher frequency of the deconvoluted peak (peak 3) is assigned to free N–H stretching (about 3550 cm^{-1}), lower frequency (peak 1) is assigned to N–H stretching which is affected by hard-hard segment H-bonding (about 3300 cm^{-1}). The central peak (peak 2) is N–H stretching which is affected by hard-soft segment H-bonding (about 3430 cm^{-1}). The frequency shift of H-bonded N–H stretching represents the stretching of H-bonding in polyurethane [13, 16]. The area of each band was determined by using the Nelder-Mead optimization method. All N–H band areas were normalized on the basis of total N–H stretching band area and are listed in Table 2, revealing that the band shift of three decomposition peaks is almost proportional to the lithium salt concentration. The peak position of free N–H stretching (peak 3) with salt addition is higher than that peak position (3450 cm^{-1}) without the salt doping. This is due to the interaction between the Li^{+1} cation and the lone pair of electrons on nitrogen atom [14], leading to the reduction of N–H bond length. Thus, the vibration energy of N–H bond is relatively increased when the salt is doped in WPU film, resulting in a higher frequency of absorption peak. Table 2 shows that the area ratio of peak 3 is insignificantly influenced by the concentration of doping salt for both of IPDI- and H$_{12}$MDI-based WPUs.

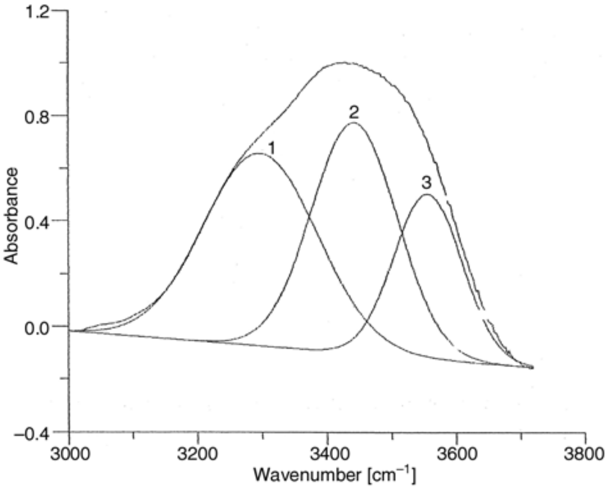

Figure 3. FTIR spectrum and deconvolution curves of IPDI-1000 WPU film in N–H stretching region

Table 2. Decomposition results of WPUs in the N–H stretching region

Film	Frequency shift [cm^{-1}]			Peak area^a [%]		
	H–H*	H–S**	Free N–H stretching	1	2	3
H$_{12}$MDI-1000	280	160	20	23.20	45.10	31.70
H$_{12}$MDI-2000	268	151	16	26.51	37.43	33.05
H$_{12}$MDI-3000	257	143	11	30.05	37.10	32.85
H$_{12}$MDI-4000	233	113	8	31.75	34.24	34.01
IPDI-1000	260	133	25	25.01	42.86	32.13
IPDI-2000	240	127	21	27.85	39.01	33.14
IPDI-3000	233	120	17	30.45	35.54	34.01
IPDI-4000	227	112	12	33.12	32.92	33.96

*Hard-hard segment H-bonded N–H stretching.

**Hard-soft segment H-bonded N–H stretching.

[a] The band areas are based on the total N–H stretching area.

In Table 2, the component of peak 1 corresponds to hydrogen bonding between N–H and carbonyl groups [14]. The position of this component shifts to higher frequency as the salt content increases for both of the two WPU systems. Because band position is related to the strength of H-bonded N–H bond, the shift to higher frequency with high salt concentration indicates a decrease in the H-bonded strength. Therefore, the H-bonding strength is decreased with increasing salt content. This is possibly due to the localization of the electron-rich oxygen atoms on the carbonyl through coordination of the Li^{+1} cation with the H-bonded species. Furthermore, the band area of peak 1 decreased with increasing salt content in Table 2. This reflects that the possibility of the hydrogen bonding between N–H and carbonyls is decreased.

Note in Table 2 reveals the band position of hydrogen bonding of N–H to –O– (ether oxygen) (peak 2) [14] of PEG soft segment is also shifted to higher frequency with the addition of salt. This shift of frequency to higher values increases with increasing salt content, implying that the more added salt in WPU gives the stronger band strength of N–H bond. This is likely due to the coordination of non-bonded electrons on the ether oxygen atoms with the Li^{+1} cation, leading to a weakening of the hydrogen-bonded strength between N–H and ether oxygen atoms. An examination of Table 2 reveals that the band area of NH-ether (peak 2) increases with increasing salt content. This can be attributed to the fact that the coordination of non-bonded electrons on ether oxygen atoms with cation is increased, inducing an increase in hydrogen bonding between N–H and ether groups.

On the other hand, the strength of H-bonding stretching of $H_{12}MDI$-based WPUs is higher than that of IPDI-based WPUs for both hard-hard and hard-soft segments. This implies that the molecular architectures of $H_{12}MDI$-based WPUs are beneficial to form the H-bonding between hard-hard and hard-soft segments as compared with IPDI-based WPUs. This observation may be related to the result of devitrification temperatures.

3.3. Ionic conductivity

Since these WPU samples possess different molecular weight of PEG in the polymer chains, it is interesting to investigate the ionic conducting behavior of these samples. Thus, AC impedance was employed to determine the conductivity (σ) of these films. The result was plotted as a Cole-Cole plot to show the real/image parts of impedance at various frequencies. A typical Cole-Cole plot of WPU film sandwiched between stainless steel electrodes is shown in Figure 4. The profile shows a straight line in which the impedance decreases with increasing frequency. This indicates that the interfacial impedance decreases with increasing frequency, which is attributed to double layer formation and charge transfer reaction. At a frequency approaching 100 kHz, the line closes to the real axis, indicating that the impedance approaches pure resistance. In this case, the interfacial impedance is negligible and the bulk resistance (R_b) is obtained. The conductivity of WPU film can be determined by letting $\sigma = (1/R_b)(L/A)$, where L and A represent film thickness and surface area of the WPU film, respectively. Figure 5 shows the Arrhenius plot of ionic conductivity for WPU films. It is obvious that IPDI-PEG (Figure 5a) and $H_{12}MDI$-PEG series (Figure 5b) have similar behavior of conductivity. The conductivity of these WPU films increases with decreasing the molecular weight of PEG. This is ascribable to the more significant hard-and soft-segment mixing exists in PEG-1000 WPUs as compared with other samples, resulting in the formation of amorphous state in WPU polymers which is readily to transport Li^+ ion in the polymer matrix. It also indicates that the conductivities of these samples almost obey the Arrhenius law but PEG-1000 sample possesses a transition point around 20°C. This transition point reflects the fact that this polymer has $T_m = 20°C$ (see Table 1), as the migration of lithium ion in polymer electrolytes should be easier in melted (amorphous) polymer state than in the crystalline state.

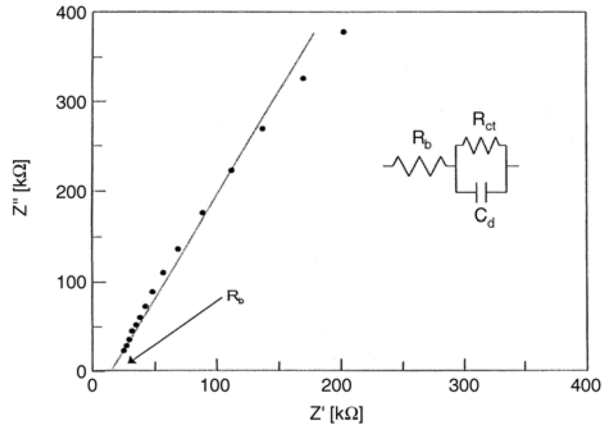

Figure 4. Cole-Cole plot of SS/WPU film (IPDI-2000)/SS at 25°C; 150 µm thickness and 0.785 cm² area for the film. Impedance frequency from 100 kHz to 100 Hz. SS represents the stainless steel. Insert is the equivalent circuit

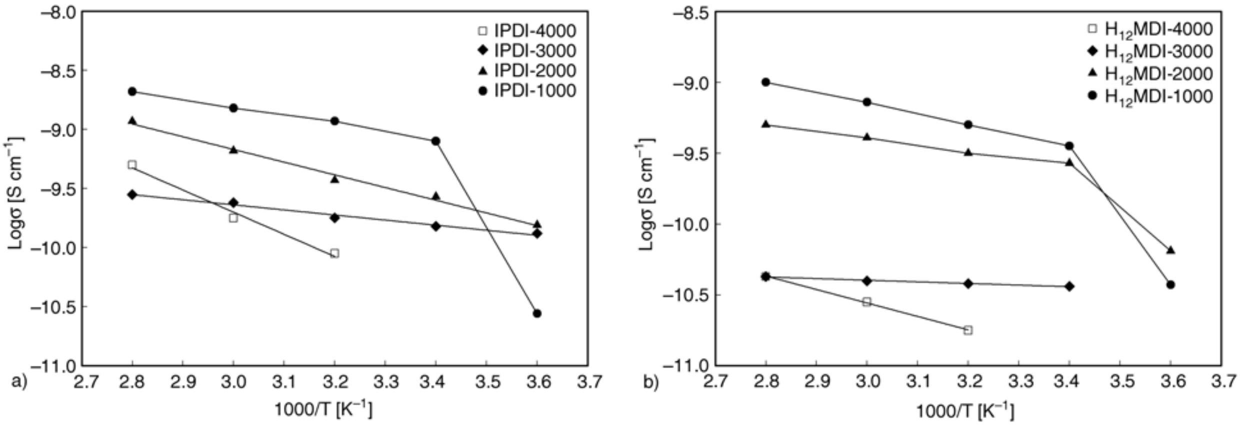

Figure 5. Arrhenius plot of conductivity for WPU films with various molecular weights of PEG. (a) IPDI and (b) $H_{12}MDI$ samples

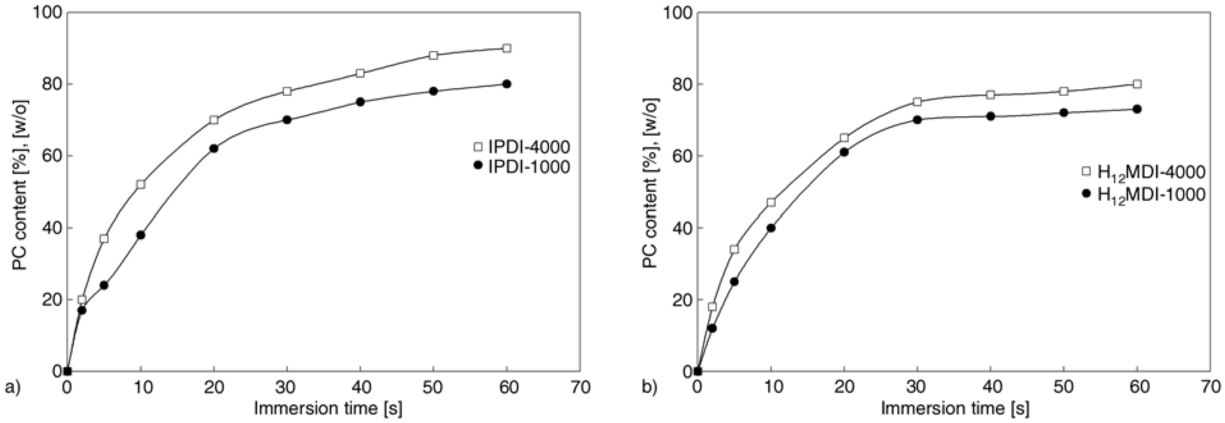

Figure 6. PC swelling rate of WPU films with various molecular weights of PEG. (a) IPDI and (b) H_{12}MDI samples

In order to improve the conductivity, these WPU samples were impregnated with PC to form gel-type electrolytes. The swollen weight was measured with various immersion times and the results were plotted in Figure 6. It is clear that the curves are saturated for all of IPDI and H_{12}MDI samples. The swelling rate may be obtained from the slope of the curves; the saturated soaking of solvent (PC) can be attained after 1 min immersion of the WPU films. Note that the swelling rate and the saturated swollen quantity increase with increasing molecular weight of PEG. This reflects that the shorter soft segment (PEG) in WPU yields the more contents of urethane groups. This readily forms the H-bonding between hard-hard and hard-soft segments to retard PC uptaking, and thus PC is mainly absorbed in soft phase of PEG. To understand the effects of PEG molecular weight on the conductivity of WPU gel electrolytes, the swollen PC in these WPU samples was controlled at about 50 wt% and consequently AC impedance was performed. The conductivity data as shown in Figure 7 was analyzed using the Arrhenius phenomenological relationship as follows (1):

$$\sigma(T) = A\exp^{-\frac{E}{k_bT}} \tag{1}$$

The Arrhenius formula is used when the ions are decoupled from the polymer host and activated hopping is required for ionic transport. In Figure 7, these straight lines imply that the conductivity of these films almost obeys Arrhenius law, and therefore, the activated hopping predominates in the conductivity process. The conductivity of gel-type WPU films (Figure 7) is higher than that of the solvent-free films as compared with the results of Figure 6. Also, there is no transition point in PEG-1000 WPU samples. This is ascribable that the lithium ion is completely solvated by PC solvent, resulting in the collapse of crystalline and H-bonding structures in these samples. Hence, the ion-conduction behavior of the gel film is quite different from that of the solvent-free film. Moreover, the conductivity increases with increasing molecular

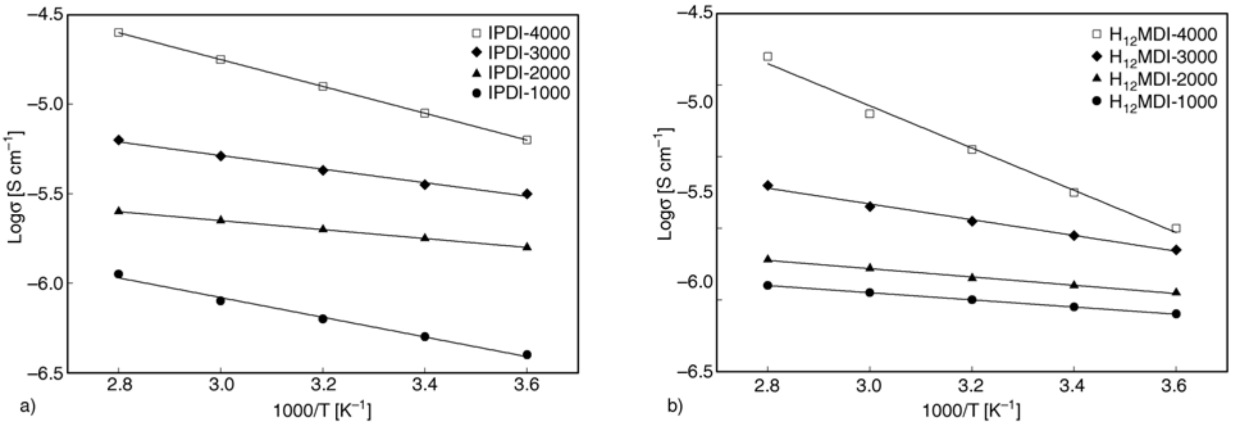

Figure 7. Arrhenius plot of conductivity for WPU gel electrolytes (containing 50 wt% PC) with various molecular weights of PEG. (a) IPDI and (b) H_{12}MDI samples

weight of PEG in gel electrolytes, indicating that the increase in the flexibility of polymer would promote the conductivity due to more channels for the mobility of Li^+ ions. Without adding the diol chain extender DMPA in these WPUs, a suitable choice of soft segment in the WPUs is possibly used as a single-ion electrolyte having a similar ~$10^{-(4-5)}$ S/cm at room temperature.

4. Conclusions

The T_g increases with the introduction of cycloaliphatic diisocyanates into PEG forming WPUs; the strength of H-bonding between hard-hard and hard-soft segments decreases with increasing molecular weight of PEG in WPUs. The molecular architectures of H_{12}MDI-based WPUs are beneficial to form the H-bonding between hard-hard and hard-soft segments as compared with IPDI-based WPUs. The hard-soft segment mixing obviously exists in the IPDI- and H_{12}MDI-1000 samples. Without adding DMPA, WPUs with the more significant phase separation possess the lower conductivity as single-ion electrolytes in IPDI- and H_{12}MDI-2000, 3000, 4000 samples. The conductivity of WPU gel electrolytes increases with increasing molecular weight of PEG. Thus, a WPU gel electrolyte of PEG-4000 exhibits an ionic conductivity as high as ~$10^{-(4-5)}$ S/cm at room temperature without adding the diol chain extender DMPA in these WPUs,. This demonstrates that this type of WPU gel electrolyte has potential for use as a single-ion electrolyte.

Acknowlegements

The financial support of this work by the National Science Council of the Republic of China under contract NSC 95-2221-E-218-060, is gratefully acknowledged.

References

[1] Yang C. H., Lin S. M., Wen T. C.: Application of statistical experimental strategies to the process optimization of waterborne polyurethane. Polymer Engineering and Science, **35**, 722–730 (1995).

[2] Murata K.: An overview of research and development of solid polymer electrolyte batteries. Electrochimica Acta, **40**, 2177–2184 (1995).

[3] Fauteux D., Massucco A., McLin M., Van Buren M., Shi J.: Lithium polymer electrolyte rechargeable battery. Electrochimica Acta, **40**, 2185–2190 (1995).

[4] Barthel J., Buestrich R., Carl E., Gores H. J.: A new class of electrochemically and thermally stable lithium salts for lithium battery electrolytes. Journal of the Electrochemical Society, **143**, 3565–3571 (1996).

[5] Ramanujachary K. V., Tong X., Lu Y., Kohn J., Greenblatt M.: Lithium ionic conductivity in poly(ether urethanes) derived from poly(ethylene glycol) and lysine ethyl ester. Journal of Applied Polymer Science, **63**, 1449–1456 (1997).

[6] Xu H. S., Yang C. Z.: The ionic conductive property of sulfonated polyethylene oxide polyurethane ionomers. Journal of Polymer Science Part B-Polymer Physics, **33**, 745–751 (1995).

[7] Petrovic Z. S., Javni I.: The effect of soft-segment length and concentration on phase separation in segmented polyurethanes. Journal of Polymer Science Part B-Polymer Physics, **27**, 545–560 (1989).

[8] Berthier C., Gorecki W., Minier M., Armand M. B., Chabagno J. M., Rigand P.: Microscopic investigation of ionic conductivity in alkali metal salts-poly(ethylene oxide)adducts. Solid State Ionics, **11**, 91–95 (1983).

[9] Gadjourova Z., Andreev Y. G., Tunstall D. P., Bruce P. G.: Ionic conductivity in crystalline polymer electrolytes. Nature, **412**, 520-523 (2001).

[10] Cheng T. T., Wen T. C.: Novel water-borne polyurethane based electrolytes for lithium batteries-(I) tailor-made polymer. Journal of Electroanalytical Chemistry, **459**, 99–110 (1998).

[11] Cheng T. T., Wen T. C.: Novel waterborne polyurethane based electrolytes for lithium batteries-(II) the effect of adding $LiCF_3SO_3$-PC. Solid State Ionics, **107**, 161–171 (1998).

[12] Wen T. C., Wang Y. J., Cheng T. T., Yang C. H.: The effect of DMPA units on ionic conductivity of PEG-DMPA-IPDI waterborne polyurethane as single-ion electrolytes. Polymer, **40**, 3979–3988 (1999).

[13] Wen T. C., Wu M. S., Yang C. H.: Spectroscopic investigations of poly(oxypropylene) glycol-based waterborne polyurethane doped with lithium perchlorate. Macromolecules, **32**, 2712–2720 (1999).

[14] Wen T. C., Luo S. S., Yang C. H.: Ionic conductivity of polymer electrolytes derived from various diisocyanate-based waterborne polyurethanes. Polymer, **41**, 6755–6764 (2000).

[15] Van Heumen J. D., Stevens J. R.: The role of lithium salts in the conductivity and phase morphology of a thermoplastic polyurethane. Macromolecules, **28**, 4268–4277 (1995).

[16] Teo L-S., Chen C-Y., Kuo J-F.: Fourier transform infrared spectroscopy study on effects of temperature on hydrogen-bonding in amine-containing polyurethanes and poly(urethane-urea)s. Macromolecules, **30**, 1793–1799 (1997).

eXPRESS Polymer Letters Vol.1, No.3 (2007) 150–156
Available online at www.expresspolymlett.com
DOI: 10.3144/expresspolymlett.2007.24

Synthesis, characterizations and electro-optical properties of nonlinear optical polyimide/silica hybrid

F. X. Qiu[1*], *P. P. Li*[2], *D. Y. Yang*[1]

[1]School of Chemistry and Chemical Engineering, Jiangsu University, Zhenjiang 212013, China
[2]Jiangsu Provincial Key Laboratory of Modern Agricultural Equipment and Technology, Zhenjiang 212013, China

Received 17 November 2006; accepted in revised form 27 February 2007

Abstract. Transparent Nonlinear Optical (NLO) inorganic/organic (polyimide/silica) hybrid composites with covalent links between the inorganic and the organic networks were prepared by the sol-gel method. The silica content in the hybrid films was varied from 0 to 22.5/wt%. The prepared PI hybrids were characterized by IR, UV-Vis, Thermogravimetric analysis (TGA), X-ray diffraction (XRD), Scanning Electron Microscopy (SEM) and Transmission Electron Microscopy (TEM). They exhibited fair good optical transparency. The SiO_2 phase was well dispersed in the polymer matrix. DSC and TGA results showed that these hybrid materials had excellent thermal stability. The polymer solutions could be spin coated on the indium-tin-oxide (ITO) glass to form optical quality thin films. The electro-optic coefficients (γ_{33}) at the wavelength of 832 nm for polymer thin films poled were in the range of 19–27 pm/V.

Keywords: *polymer composites, nonlinear optical, hybrid, electro-optical property*

1. Introduction

Organic polymeric second-order nonlinear optical (NLO) materials have been extensively studied due to their potential application in integrated photonic devices such as high-speed electro-optic (EO) modulators and switches optical data storage and information processing [1–3]. It is most remarkable that recent improvements in various polyimide systems have resulted in several waveguide devices based on the second-order NLO polymers. However, to develop practical devices, the challenge of achieving excellent tradeoffs in all the properties of the NLO polymers (i.e. EO coefficients, thermal, chemical, and photochemical stability, temporal dipole alignment stability, optical loss, dielectric constant and mechanical properties) still exists [4–6]. However, inorganic glasses are excellent photonic media because of their high optical quality, extremely low optical losses and thermal stability. Therefore, combining inorganic glass and organic photo-functional molecules is probably one of the best ways of getting optical waveguide materials with large optical nonlinearity and low losses.

Combining organic polymers with inorganic oxides using variations of the sol-gel method has become prevalent for the past 10 years as a means of preparing organic-inorganic hybrid and inorganic glasses [7–10]. The preparation of the films with high transmission coefficient from infrared to about 220 nm by sol-gel method was considered a successful technique since this way, high quality waveguide devices were obtained intended to applications in integrated optics for telecommunications [11–12]. On the other hand, the sol-gel processes with low processing temperature allows the incorporation of organic polymer networks leading to the formation of organic-inorganic hybrid materials.

---

*Corresponding author, e-mail: fxqiuchem@163.com

In this study, we synthesized an electro-optical chromophore (Figure 1), hydroxyl polyimide based on the fluorine-containing monomers, 6FDA-6FHP (Figure 2) and side-chain NLO polyimide 6FDA-6FHP-NLO (Figure 3). We report the sol-gel synthesis of organic-inorganic silica waveguide materials (Figure 4), and investigated the optical properties, thermal properties and micrographs study.

2. Experimental

2.1. Materials and characterization

N, N-dimethylacetamide (DMAc) were stirred over powered calcium hydride overnight and then distilled under reduced pressure and stored over 4 Å molecular sieves. The 4,4’-(Hexafluoroisopropylidene) diphthalic Anhydride (6FDA) and 2,2-Bis (3-amino-4-hydroxyphenyl) hexafluoropropane (6FHP) used in the polyimide synthesis were obtained from TCI and used without further purification. The 3-aminopropyltriethoxysilane, APTES was purchased from Nanjing shuguang chemical plant. Tetrahydrofuran (THF) was purified by distillation and other reagents and solvents were obtained commercially and were used as received.

IR spectra of the prepared thin films were obtained on a KBr pellet using Nicolet AVATAR 360 spectrometer. To examine the optical characteristics of materials with addition of sample light transmission was measured in ultraviolet and visible range by means of a spectrophotometer (Shimadzu UV-240). The fracture surfaces of hybrid thin films were examined on a HITACHI X-650 Scanning Electron Microscope (SEM). HITACHI H-600 Transmission Electron Microscope (TEM) measured the particle sizes. Thermogravimetric analysis (TGA) and differential scanning calorimetry (DSC) were performed on NETZSCH STA449C. The programmed heating range was from room temperature to 800°C, at a heating rate of 10°C/min under a nitrogen atmosphere. The measurement was taken using 6–10 mg samples. TGA and DSC curves were recorded. X-ray diffraction (XRD) patterns of SiO_2 were obtained with a CuKα X-ray source and a step of 0.02(2θ) and run from $2\theta = 6\sim80°$ at room temperature. The elemental analysis was determined on the Foss Heraeus CHN-O-Rapid.

2.2. Synthesis of a NLO chromophore

To a stirred solution of p-nitroaniline (13.8 g, 0.10 mol) in methanol/HCl (50%, V/V, 50 ml) was added sodium nitrite (6.90 g, 0.10 mol) in ice-water (15%, m/m) at 0°C [13–16]. The mixture was stirred at this temperature for 1 h. Meanwhile stirred solution of aminobenzene purified by distillation (9.3 g, 0.10 mol) in HCl (50 ml, 1 mol·l^{-1}). Then these two solutions were mixed and sodium nitrite (6.90 g, 0.10 mol) was added in ice-water (15%, m/m) at 0°C. The mixture was added dropwise into a solution of N-2-hydroxyethyl-N-methylaniline (15.10 g, 0.10 mol) with excess HAc-NaAc. The mixture was stirred at 40–50°C for 20 min. The mixture solution was cooled down and placed for 2 h, and the solid was collected by filtration and further recrystallized from toluene/methanol (4:1) to give a bright red crystal. ^{1}H NMR (300 MHz, acetone-d$_6$, ppm): 10.61 (s, OH, 1H), 8.05 (s, ArH, 2H), 8.00 (s, ArH, 2H), 7.83 (s, ArH,

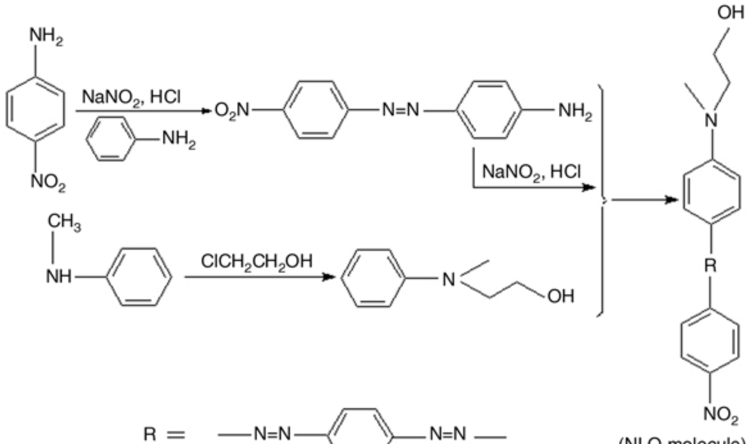

Figure 1. Synthesis of the NLO chromophore molecule

2H), 7.11 (s, ArH, 2H), 6.56 (s, ArH, 2H), 6.20 (s, ArH, 2H), 4.20 (s, –CH_2CH_2O–, 2H), 3.73 (s, –CH_2CH_2O–, 2H), 2.46 (s, –CH_3, 3H). Anal. Calcd for $C_{21}H_{20}N_6O_2$: C, 62.38%; H, 4.95%; N, 20.79%. Found: C, 62.48%; H, 4.89%; N, 20.82%. The synthetic route is shown in Figure 1.

2.3. Hydroxyl polyimide synthesis

The polymerization was conducted in a dry nitrogen flushed three-neck flask with a magnetic stirrer, reverse Dean-stark trap, and reflux condenser filled dry xylene. A stoichiometric amount of 6FDA (3.33 g, 7.5 mmol) was added to a solution of 6FHP (2.7 5g, 7.5 mmol) in 30 ml DMAC at 0°C. The solution was then warmed to room temperature and magnetically stirred overnight under nitrogen to form the poly (amic acid) solution. Dry xylene (30 ml) was added to the flask, and the poly (amic acid) was thermally cyclized in an oil bath at 160°C for 5 h under nitrogen atmosphere. The resulting solution was added dropwise into a solution of methanol/water (1:1, V/V, 50 ml) and 2NHCl (10 ml) in a high-speed blender to obtain the polyimide A or B. The product was filtered and washed with methanol/water (1:1, 10 ml) three times, and dried at 60°C under vacuum for 24 h. **A** ^1H NMR (300 MHz, CD_3COCD_3, ppm): 10.65 (s, OH, 2H), 8.44 (s, ArH, 2H), 8.35 (d, ArH, 2H), 8.33 (s, ArH, 2H), 7.62 (s, ArH, 2H), 7.32 (d, ArH, 2H), 7.10 (d, ArH, 2H). Anal. Calcd for $C_{34}H_{14}F_{12}N_2O_6$: C, 52.71%; H, 1.81%; N, 3.62%. Found: C, 52.79%; H, 1.78%; N, 3.66%. The molecular weight was measured by GPC and has Mn of 17,800, M_w of 37,300 with a polydispersity of 2.10 (polystyrenes as standards). The synthetic route was shown in Figure 2.

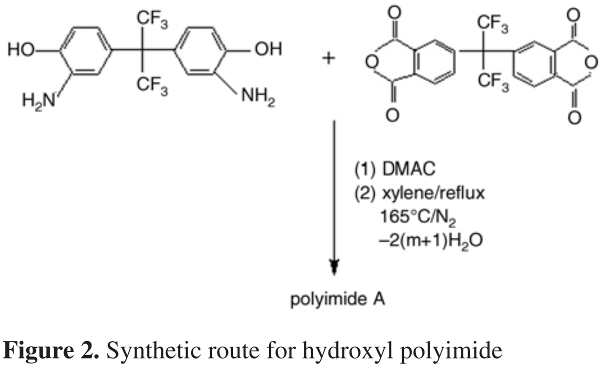

Figure 2. Synthetic route for hydroxyl polyimide

2.4. Synthesis of side-chain NLO polyimide

The polyimide A (0.39 g, 0.5 mmol), PPh_3 (0.39 g, 1.5 mmol) and 4-(N-2-hydro-xyethyl-N-methyl-anino)-4'-(p-nitrobenzene-diazenyl) azobenzene (NLO chromophere) (0.40 g, 1.00 mmol) were dissolved in THF (15 ml). Diethyl azodicarboxylate (DEAD) (0.26 g, 1.50 mmol) was added dropwise into the solution under nitrogen atmosphere. The reaction mixture was stirred for 2 days at room temperature, and then the resulting reaction solution was added dropwise into an agitated solution of methanol/water (1:1,30 ml) and 2N HCl (5 ml) in a high-speed blender. The collected solid further precipitated in THF (10 ml) and reprecipitated into the solution of methanol/water. The product was filtered out and washed with methanol/water for several times, and dried at 60°C under vacuum for 24 h. **B** ^1H NMR (300 MHz, CD_3COCD_3, ppm): 8.46 (s, ArH, 2H), 8.38 (d, ArH, 2H), 8.35 (s, ArH, 2H), 8.06 (s, ArH, 4H), 7.99 (s, ArH, 4H), 7.85 (s, ArH, 4H), 7.63 (s, ArH, 2H), 7.33 (d, ArH, 2H), 7.13 (d, ArH, 2H), 7.08 (s, ArH, 4H), 6.55 (s, ArH, 4H), 6.21 (s, ArH, 4H), 4.19 (s, –CH_2CH_2O–, 4H), 3.66 (s, –CH_2CH_2O–, 4H), 2.40 (s, –CH_3, 6H) Anal. Calcd for $C_{76}H_{50}F_{12}N_4O_{10}$: C, 59.00%; H, 3.23%; N, 12.68%. Found: C, 59.06%; H, 3.21%; N, 12.73%. The molecular weight was measured by GPC and has an M_n of 19,600, an M_w of 41,400 with a polydispersity of 2.11 (polystyrenes as standards). The synthetic route is shown in Figure 3.

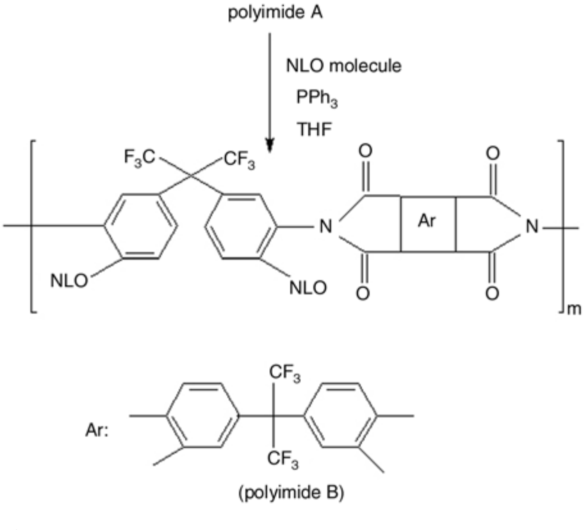

Figure 3. Synthetic route for side-chain NLO polyimide

2.5. Synthesis of inorganic-organic hybrid waveguide materials

Hybrid materials were successfully synthesized via sol-gel process. Its technique is based on creating two individual homogeneous inorganic and organic solutions, which are then mixed together and allowed to react at room temperature with carefully controlled evaporation conditions. The first homogeneous inorganic solution is a partially acid hydrolyzed alkoxide sol in THF, while the second homogenous organic solution is an APTES functionalized polyimide in THF. Furthermore, the presence of the pendant APTES groups on the functionalized polyimide facilitates chemical bonding with the partially hydrolyzed alkoxide sol via condensation reactions as shown in Figure 1. At the completion of the evaporation step of the previously mixed inorganic and organic solutions, further heat treatments are used to promote additional conversion of the alkoxide xerogel domains via condensation reactions. The hybrid material was prepared by systematically varying the concentration of the tetrathylorthosilicate (TEOS). The silicon alkoxide content is reported as a weight percent in the hybrid system and is based on the loading mass and not on the mass of silica after the sol-gel process. This is shown in Figure 4. Table 1 summarized the various hybrid systems fabricated for this study.

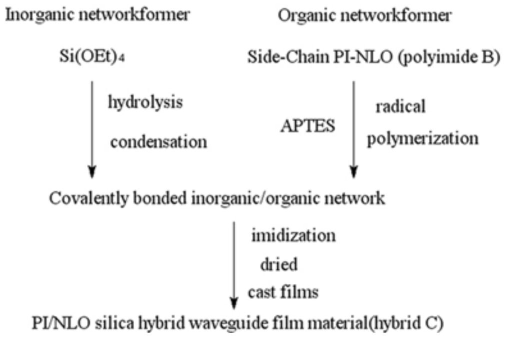

Figure 4. Synthesis of polyimide/silica hybrid waveguide systems

3. Results and discussion

Figure 5 illustrates the FT-IR spectra of the prepared polyimide-silica hybrid thin films C-1, C-2, C-3 and C-4. The characteristic absorption bands of the imide group are observed at 730, 1378, 1716, 1776 cm^{-1} for all samples. The intensity of the absorption band around 1000~1140 cm^{-1} gradually increases with increasing silica content, consistent with the formation of the three-dimensional Si–O–Si network in the hybrid film [17–18]. The broad absorption around 3100~3500 cm^{-1} are assigned to the Si–OH residue, formed in the hydrolysis of alkoxy groups of TEOS. This band is barely detectable in the spectrum of C-1 with lower silica content but increases its intensity in that of C-4 with higher silica content [19]. Besides, the FT-IR spectrum consists of some peaks located at 1520 cm^{-1} (ν_{as}, –N=N–), 1364 cm^{-1} (ν_{str}, –C–N–C–), 1345 cm^{-1} (ν_s, $-NO_2$), 1378 cm–1 (wagging CH_2), 695 cm^{-1} (wagging N–H), indicating that the silica xerogel networks is composed of Si–O–Si backbones and some organic groups.

Figure 6 and Figure 7 present the SEM and TEM micrographs of the prepared polyimide-silica hybrid thin films C-2 and C-4. In most cases, surface morphology of materials is of great impor-

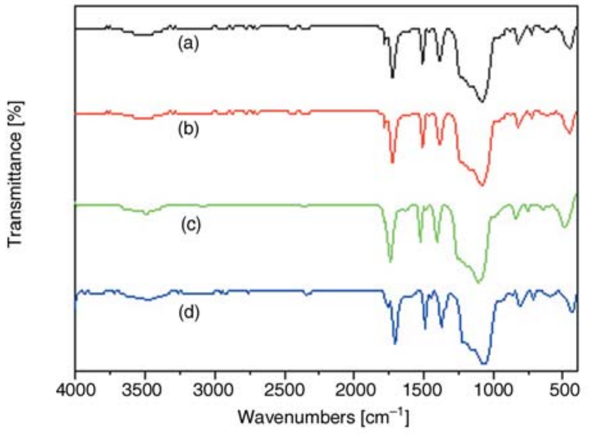

Figure 5. FT-IR spectrums of C-1 (a), C-2 (b), C-3 (c) and C-4 (d)

Table 1. Reactant Summary and properties of polyimide and hybrid systems

Materials	TEOS [wt%]	polyimide [g]	APTES [ml]	HCl [ml]	H_2O [ml]	THF [ml]	Appearance[a] [ml]	T_g[b] [°C]	T_d[c] [°C]	γ_{33} [pm/V]
C	0							225	340	27
C-1	5	2.55	0.20	0.10	0.25	30	Transparent	348	459	25
C-2	10	2.55	0.20	0.25	0.53	30	Transparent	353	462	23
C-3	15	2.55	0.20	0.50	1.02	30	Transparent	356	469	20
C-4	22.5	2.55	0.20	0.65	2.10	30	Transparent	362	472	19

[a]UV-Vis spectrum was observed; [b]Experimental results from DSC; [c]Experimental results from TGA

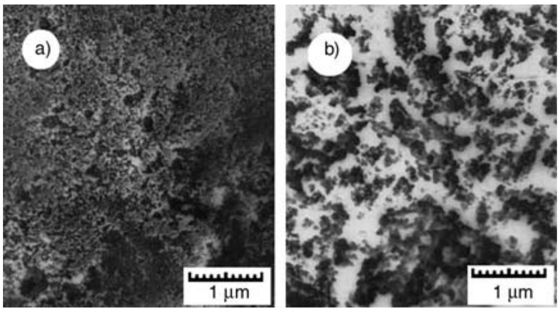

Figure 6. SEM photographs of C-2 (a) and C-4 (b)

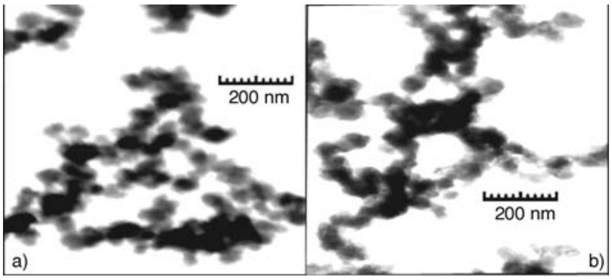

Figure 7. TEM photographs of C-2 (a) and C-4 (b)

tance for many technical applications requiring well-defined surfaces or interfaces. The SEM figures reveal that no phase separation. That is, the covalent bonding (Si–O–Si) between the organic and inorganic components enhanced miscibility. Both components were homogeneously and uniformly dispersed at a molecular level. When the silica content was below 15 wt%, the silica particle size was 50 nm, as indicated in Figure 7. However, when the silica content was increased to 22.5 wt%, the particle size was increased to 80 nm. The increase in the silica particle size clearly resulted from the increase in the aggregation tendency as the silica content and the silica particle number were increased. These micrographs show the fine interconnected or co-continuous phases morphology, which improve the efficiency of stress transfer mechanisms between the two components.

XRD measurements were inferred by estimating the crystallizability of the hybrid material (C-2). From Figure 8, the diffractogram typical of amorphous samples can be seen, The XRD pattern of the hybrid films (C-3) display only a very broad hump centered at 2θ = 23.55°; originating from amorphous phase of aromatic polyimide. This result also indicates that covalent bonding (Si–O–Si) between the organic and inorganic components enhanced miscibility.

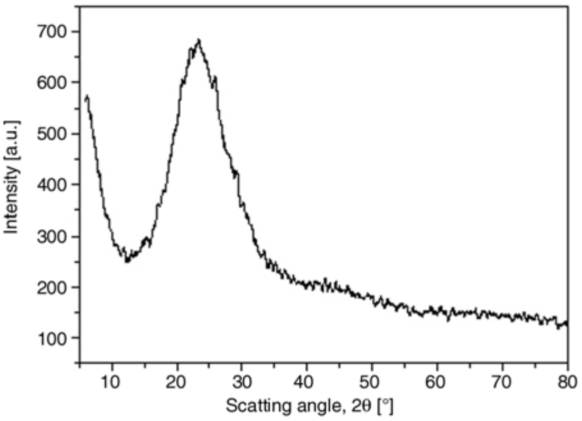

Figure 8. XRD patterens of the C-3

To examine thermal activities of hybrid materials in higher temperature range and their thermal decomposition characteristics, DSC and TGA experiments were carried out on NETZSCH STA449C with the heating rate 10°C/min under nitrogen. Their data listed in Table 1. Compared with the pure *E* or *F*, the initial degradation temperature (T_d) of hybrid materials increased with the increase of TEOS moiety. The enhanced thermal stability of hybrid materials is due to the formation of network of polyimide and the inorganic moieties, which results from the restriction of polymer chain mobility and becomes more intertwined with the rigid silica network. Therefore, the existence of covalent bonds between polyimide and silica impose even more restraints to chain movement in hybrids. DSC analysis shows glass transition temperature (T_g) for the polyimide- silica network in the hybrids at 348~362°C. Based on what was mentioned the above, the compatibility of the PI/SiO_2 hybrid can be enhanced via incorporating polymer matrix with inorganic silica covalently. The chemical bonding not only restricts the migration of inorganic silicates but also hinders the aggregation of silanol [20]. It is estimated that these materials will be pretty good for the practical application.

High-quality films could be easily prepared from the polyimides and hybrids solutions in NMP by spin coating on ITO glass. The electro-optic (EO) coefficient measurement of our nanohybrid was performed at a wavelength of 832 nm. The test sample consisted of a high-index prism, a thin silver film, a poled material layer, a buffer layer, and a base silver film. The silver film was thermally evaporated onto the hypotenuse face of a high-index prism as the first electrode. The thickness of the film was about 55 nm. A polymer was spin coated onto the silver substrate to a thickness of 1–2 µm, which can support four or five surface-plasmon modes with TE or TM polarization. A polymer buffer layer was then coated onto the polyimide film to a thickness of 3–5 μm or so. Corona discharge poling was performed by alignment of the chromophore dipoles in a high static electric field while the polyimide was heated to high mobility close to its glass transition temperature. The poling voltage was 1500 V. Finally; another silver film was deposited onto the buffer layer as the second electrode. The γ_{33} values were listed in Table 1. From the Table 1, the γ_{33} coefficients of hybrids were smaller than corresponding polyimide. This was due to the content of chromophore is smaller than the pure polyimide. Therefore, these results showed that these polymers might be useful in photonic device applications.

4. Conclusions

Transparent Nonlinear Optical (NLO) inorganic/organic waveguide films systems had been prepared in situ sol-gel process. They have network structure and silica particles were uniformly dispersed on the nanoscale. Covalent bonding (Si–O–Si) between the organic and inorganic components enhanced miscibility between the silica and the copolymer. The thermogravimetric analysis and differential scanning calorimetry behavior indicate excellent thermal stability. The resulting polyimide/silica hybrids exhibited a relatively high $T_g > 348°C$ and thermal stability up to 448°C. Large EO coefficient values (20–30 pm/V) at the wavelength of 832 nm were achieved and the values remained well.

Acknowledgements

This work was financially supported by the Jiangsu Planned Projects for Postdoctoral Research Funds (0602037B), the Natural Science of Jiangsu Education (05KJB150016) and the fund of Jiangsu University (06JDG015).

References

[1] Dalton L. R., Harper A. W., Ghosn R., Steier W. H., Ziari M., Fetterman H., Shi Y., Mustacich R. V., Jen A. K. Y., Shea K. J.: Synthesis and processing of improved organic second-order nonlinear optical materials for applications in photonics. Chemistry of Materials, **7**, 1060–1081(1995).

[2] Burland D. M., Miller R. D., Walsh C. A.: Second-order nonlinearity in poled-polymer systems. Chemical Reviews, **94**, 31–75 (1994).

[3] Marder S. R., Kippelen B., Jen A. K-Y., Peyghamarian N.: Design and synthesis of chromophores and polymers for electro-optic and photorefrative applications. Nature, **388**, 845–851(1997).

[4] Leng W. N., Zhou Y. M., Xu Q. H., Liu J. Z.: Synthesis and characterization of nonlinear optical side – Chain polyimides containing the benzothiazole chromophores. Macromolecules, **34**, 4774–4779 (2001).

[5] Qiu F. X., Zhou Y. M., Liu J. Z., Zhang X. P.: Preparation, morphological and thermal stability of polyimide/silica hybrid material containing dye NBDPA. Dyes and Pigments, **71**, 37–42 (2006).

[6] Watanabe O., Tsuchimori M., Okada A., Ito H.: Electro-optic intensity modulator using a vovel urethane-urea copolymer. Japanese Journal of Applied Physics, **37**, 5588–5592 (1998).

[7] Loy D. A., Shea K. J.: Bridged polysilsesquioxanes. Highly porous hybrid organic-inorganic materials. Chemical Reviews, **95**, 1431–1442 (1995).

[8] Wen J. Y., Wilkes G. L.: Organic/inorganic hybrid network materials by the sol-gel approach. Chemistry of Materials, **8**, 1667–1681 (1996).

[9] Chung C. M., Lee S. J., Kim J. G., Jang D. O.: Organic-inorganic polymer hybrids based on unsaturated polyester. Journal of Non-Crystalline Solids, **311**, 195–198 (2002).

[10] Kim J. H., Lee Y. M.: Gas permeation properties of poly(amide-6-b-ethylene oxide)-silica hybrid membranes. Journal of Membrane Science, **193**, 209–225 (2001).

[11] Najafi S. I., Touam T., Sara R., Andrews M. P., Fardad M. A.: Sol-gel glass waveguide and grating on silicon. Journal of Lightwave Technology, **16**, 1640–1646 (1998).

[12] Alvarez-Santos S., Gonzalez-Lafont A., Lluch J. M.: On the intramolecular proton transfers in N,N'-bis(salicydene)-p-phenylene diamine. New Journal of Chemistry, **18**, 873–877 (1994).

[13] Qiu F. X., Jiag Y., Zhou Y. M., Liu J. H.: Synthesis, characterization and thermal properties of novel PMDA-PAPD/silica hybrid network polymers. Silicon Chemistry, **3**, 65–73 (2006).

[14] Qiu F. X., Zhou Y. M., Liu J. Z.: The synthesis and characteristic study of 6FDA-6FHP-NLO polyimide/SiO_2 nanohybrid materials. European Polymer Journal, **40**, 713–720 (2004).

[15] Saadeh H., Gharavi A., Yu D., Yu L. P.: Polyimides with a diazo chromophore exhibiting high thermal stability and large electrooptic coefficients. Macromolecules, **30**, 5403–5407 (1997).

[16] Cojocariu C., Rochon P.: Thermotropic side-chain liquid crystalline copolymers containing both mono- and bisazobenzene mesogens: synthesis and properties. Macromolecules, **38**, 9526–9538 (2005).

[17] Que W. X., Hu X.: Sol-gel derived titania/γ-glycidoxypropyltrimethoxysilane and methyltri methoxysilane hybrid materials for optical waveguides. Journal

of Sol-Gel Science and Technology, **28**, 319–325 (2003).

[18] Cornelius C. J., Marand E.: Hybrid inorganic-organic materials based on a 6FDA- 6FpDA-DABA polyimide and silica: physical characterization studies. Polymer, **43**, 2385–2400 (2002).

[19] Zheng M. P., Gu M. Y., Jin Y. P., Jin G. L.: Preparation, structure and properties of TiO_2-PVP hybrid films. Materials Science and Engineering: B, Solid State Materials for Advanced Technology, **77**, 55–59 (2000).

[20] Hsiue G. H., Kuo W. J., Huang Y. P., Jeng R. J.: Microstructural and morphological characteristics of PS-SiO_2 nanocomposites. Polymer, **41**, 2813–2825 (2000).

eXPRESS Polymer Letters Vol.1, No.3 (2007) 157–165
Available online at www.expresspolymlett.com
DOI: 10.3144/expresspolymlett.2007.25

Modeling study on the combustion of intumescent fire-retardant polypropylene

F. Zhang, J. Zhang, Y. Wang*

Key Laboratory of Rubber-Plastics for Ministry of Education, Qingdao University of Science and Technology, 53 Zheng Zhou Road, Qingdao, 266042, P.R. China

Received 13 February 2007; accepted in revised form 5 March 2007

Abstract. The heat transfer and burning behavior of intumescent fire-retardant polypropylene were studied by cone calorimeter at heat flux levels of 50 $kW\cdot m^{-2}$ to establish an essential physical model for the intumescence process in fire. A mathematical model for the burning process of fire-retardant intumescent polymer was put forward based on the assumption that an intumescent front existed between the char layer and virgin layer. The model emphasizes the thermodynamic aspect of the intumescence process and a corresponding submodel is presented. Meanwhile the thicknesses and mass loss rates of the intumescent polypropylene during burning were measured for the validation of the modeling results. Thermal conductivity and heat capacity of polymer material were also measured as input parameters of the model. The validation results showed that the intumescent thicknesses and mass loss rates predicted by the model were in good agreement with the experimental results. The model was also used to predict the temperature distribution across the sample thickness during burning. The study shows that the present model can appropriately describe the intumescent behavior of the polymer and numerically predict its mass loss rates and temperature distribution in fire.

Keywords: *modeling and simulation, intumescence, polymer burning, cone calorimeter, polypropylene*

1. Introduction

Polypropylene (PP) is widely used in many fields such as housing materials, transport or electrical engineering applications. The polymer is inherently flammable due to its chemical constitution and flame retardancy is usually required in its applications. Halogen containing fire retardants were widely used for PP due to their high efficiency. However, the toxicity and corrosiveness of the combustion products and smoke generated from these fire reatradants have limited their further development. As an alternative way to improve the polymer's fire resistance, the intumescent fire retardant systems are growing rapidly[1–4].

Intumescent fire retardant materials are halogen-free, and provide flame retardant properties by developing a carbonaceous shield (char) on the surface protecting the underlying material from the action of the incident heat flux. The resulting char reduces the heat transfer to the substrate. Generally, intumescent formulations include three major components [5, 6]: 1 – acid source, such as phosphate; 2 – carbonific agent such as polyols; 3 – blowing agent such as melamine. When exposed to the heat flux from a fire, the temperature within these materials rises, causing the thermoplastic to melt. At a critical temperature, an endothermal chemical reaction releases volatiles, which results in swelling of the intumescent layer to many times of its original thickness. There are several reactions occurring almost simultaneously, but in a proper sequence during swelling. First, the acid source must decompose to yield an inorganic acid. Then it takes part in the dehydration of the carbon source to yield the

---

*Corresponding author, e-mail: safetyqust@163.com carbon char. Finally, the blowing agent decomposes to yield gaseous products that cause the char to swell and hence provide the thermal barriers to protect the underlying materials.

The processes taking place during intumescence were studied mainly from the chemical viewpoint. However, in recent years the number of reliable numerical models developed to predict the burning behavior of intumescent fire retardant materials is growing. Proper modeling can provide a useful means to simulate the influence of various parameters on the efficiency of intumescence and help to develop intumescent fire retardant.

Several models [5, 7–11] have been developed to study the effects of intumescence on heat transfer to the underlying surface. Most models are one-dimensional, and concentrate on the effects of swelling on the thermal properties of the materials. The one-dimensional models have been developed to investigate intumescent behavior with energy and mass conservations. The thickness of virgin material and char layers and the location of the pyrolysis zone are functions of the time, and each layer is assigned its own values of thermodynamic parameters. All of these models rely on empirical information such as the size and rate of expansion. For these models, it is generally believed that two mechanisms are responsible for slowing the transport of heat. One is that the pyrolysis reaction is endothermal, causing energy to be absorbed during swelling phase. Another one is by reducing thermal conductivity of the intumescent char. Staggs [12] has described a model of volatile transport and has discussed the effects of large changes in volume. Several studies [13] of solid phase decomposition and char forming are indicative of the complex processes.

Two or three-dimensional intumescent models have also been developed. Bhargava *et al.* [14] studied the heat transfer in two dimensions through epoxy based fire resistant coatings. In their model, only energy equations were incorporated while the endothermal effect was ignored. A three-dimensional approach was investigated at NIST [15], in which bubbling, melt hydrodynamics, heat transfer and chemical reactions were incorporated. The bubbles obey equations of mass, momentum, and energy on an individual basis according to the values of local parameters, and their collective behavior is responsible for the swelling and fire retardant properties of the material. The number of bubbles must be added as a known parameter value, but the fact is that it is hard to know the number. It is only an empirical value. All these shortcomings limit the model's further development.

In this paper, the heat transfer and burning behaviors of the intumescent fire-retardant polypropylene were studied using cone calorimeter, DSC, and DRX-I thermal conductivity tester to establish an essential physical model for the intumescence process in fire. A mathematical model for the burning process of fire-retardant intumescent polymer was put forward based on the assumption that an intumescent front existed between the char layer and virgin layer. In particular, an intumescent heat absorption model was incorporated to include thermodynamic swelling work involved in the intumecent process. Several important parameters were measured as input values of the model.

2. Modeling development

2.1. Physical Model Description

When an intumescent fire-retardant material is exposed to an external heat source, the initial heat transfer mode on the material is dominated by heat conduction and this is a preheating stage. The temperature of the material increases continuously with time under the influence of the external heat flux. When the temperature of the material reaches the temperature of intumescence, a thin intumescent layer is formed on the material surface. The intumescent reaction will occur within the intumescent layer. The incombustible and combustible gases will release from the intumescence layer, which make the viscoelastic fluid expand. Intumescent interface gradually moves into the inside of the material, with residual char left. This stage is the intumescent burning stage. So the material can be divided into three independent layers, i.e. char layer, intumescence layer and virgin layer, as shown in Figure 1. On heating, the intumescence

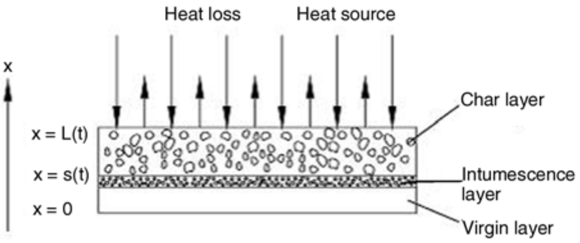

Figure 1. Schematic diagram of one-dimensional intumescent polymer model

develops and the intumescent front interface moves into the material from the top ($x = L(t)$) to the bottom ($x = 0$). The position of the front is defined by its location at $x = s(t)$. As the intumescent front interface moves through the material, the change of volume as char is formed will push the boundary of the top surface $x = L(t)$ upwards.

2.2. Intumescent heat absorption submodel

One of the intumescent fire-retardant mechanisms is heat absorption within intumescent layer. The heat absorption may primarily come from two sources, i.e. pyrolysis heat of the material including phase change heat and intumescent heat absorption. The latter is a peculiar phenomenon occurring during intumescence and has rarely been investigated so far. In this study, an intumescent heat absorption submodel was developed and coupled to describe intumescence mechanism.

The submodel is based on the following simplifying assumptions: 1 – the volatile gases behave ideally; 2 – intumescence reaction occurs at a definite temperature with infinitely thin layer; 3 – there is a thermodynamic equilibrium state between the intumescence layer and surroundings. So the infinitely thin intumescence layer can be approximately treated as an isothermal reversible system. Figure 2 shows intumescent volume change from state 1 (n, P_1, V_1, T) to state 2 (n, P_2, V_2, T).

It is well known that when ideal gas expands from initial state 1 (n, P_1, V_1, T) to state 2 (n, P_2, V_2, T) in an isothermal reversible way, the work in the process is reversible work, and

$$W = -\int_{V_{g1}}^{V_{g2}} p\,\mathrm{d}V \tag{1}$$

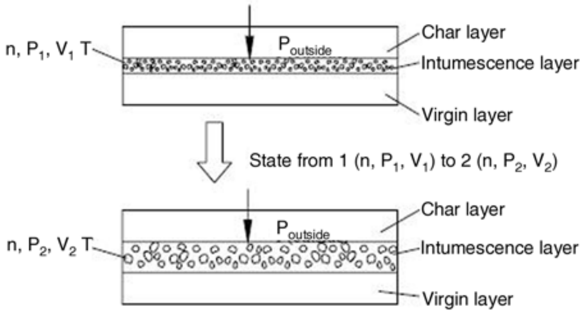

Figure 2. Intumescent volume change from state 1 (n, P_1, V_1, T) to state 2 (n, P_2, V_2, T)

where p represents internal pressure. Replace ideal gas state equation $pv = nRT$ with the Equation (1), the Equation (2) is deduced:

$$W = -\int_{V_{g1}}^{V_{g2}} \frac{nRT}{V}\mathrm{d}V = nRT\ln\left(\frac{V_{g_1}}{V_{g_2}}\right) = \frac{m_g}{M_g}RT\ln\left(\frac{V_{g_1}}{V_{g_2}}\right) \tag{2}$$

According to the first law of thermodynamics $\Delta U = Q + W$, with $\Delta U = 0$ for ideal gas isothermal process. So the heat absorption, Q, in the isothermal reversible process is (3):

$$Q = -W = -\frac{m_g}{M_g}RT\ln\left(\frac{V_{g_1}}{V_{g_2}}\right) = \frac{m_g}{M_g}RT\ln\left(\frac{V_{g_2}}{V_{g_1}}\right) \tag{3}$$

Suppose that intumescence semi-fluid solid's volume is V, the porosity is ϕ, then the gas volume is $V\cdot\phi$, accordingly (4):

$$Q = \frac{m_g}{M_g}RT\ln\left(\frac{\phi_2 V_2}{\phi_1 V_1}\right) \tag{4}$$

When the sample is flamed out, we suppose that the residual char yield will not change with the depth of the sample. So the residual char yield, char%, is the same at the same experimental conditions (5):

$$m_g = m_0(1 - \text{char\%}) \tag{5}$$

Substituting Equation (5) in Equation (4), we obtain:

$$Q = \frac{m_0(1-\text{char\%})}{M_g}RT\ln\left(\frac{\phi_2 V_2}{\phi_1 V_2}\right) \tag{6}$$

For simplification, we suppose porosity ϕ will not change during intumescence. So Equation (6) can be simplified as Equation (7).

$$Q = \frac{m_0(1-\text{char\%})}{M_g}RT\ln\left(\frac{V_2}{V_1}\right) \tag{7}$$

As per unit mass semi-fluid solid expands from V_1 to V_2, the heat absorption needed, Q, is (8):

$$Q = \frac{1}{m_0}\left[\frac{m_0(1-\text{char\%})}{M_g} RT \ln\left(\frac{V_2}{V_1}\right)\right] = \frac{1-\text{char\%}}{M_g} RT \ln\left(\frac{V_2}{V_1}\right) \quad (8)$$

As per unit mass semi-fluid solid expands one unit volume, the heat absorption needed, q_i, is (9):

$$q_i = \frac{\ln 2}{M_g} RT(1-\text{char\%}) \quad (9)$$

As reported previously [11], it is assumed that the generated gas composition is approximated by a mixture of 50%(wt) CO_2 and 50%(wt) H_2O. The generated gas molar mass M_g can be expressed by the Equation (10):

$$M_g = 50\%\cdot M_{H_2O} + 50\%\cdot M_{CO_2} \quad (10)$$

Therefore, the generated gas molar mass M_g was taken as equal to 31 g·mol^{-1}.

The pyrolysis temperature of PP occurs at about 553~623 K [16]. If we take the intumescence temperature as 600 K, char% = 31.94%, M_g = 31 g·mol^{-1}, and input these parameter values into Equation (9), the result of q_i is $7.59\cdot10^4$ J·kg^{-1}. In literature [11, 17] the values of pyrolysis heat reported for PP are variable, ranging from 50 J·kg^{-1} to $1.3\cdot10^6$ J·kg^{-1}. These differences in pyrolysis heat may be caused by different experiment conditions, however, it is clear that more accurate pyrolysis heat of PP is needed. The calculation results in Equation (9) show that the intumescent heat absorption for PP is of importance comparing with that of pure PP.

2.3. Intumescent velocity submodel

For intumescent velocity u, it requires an equation to relate the velocity to other parameters. Basically, a momentum balance would be performed to obtain the relationship between the pressure generated by the volatile products, the bulk viscosity of the semi-fluid solid, and the velocity. However, the pressure field and viscosity are not easily attainable experimentally [15]. In this paper, we adopted an alternative approach to determine intumescent velocity by relating it to moving velocity $\partial s/\partial t$ of intumescent front interface. Under certain experimental conditions, intumescent velocity u is a function of intumescent front interface movement velocity. We define an intumescent ratio $\Delta v_f/v_0$, where Δv_f is the difference between the initial volume v_0 and the final volume v_f, v_0 is the initial volume of sample, d is the initial depth of sample, and D is the final depth of sample.

Assuming that the intumescent direction of material is one-dimensional (11), (12):

$$\frac{D}{d} = \frac{v_f}{v_0} \quad (11)$$

$$\frac{D-d}{d} = \frac{v_f - v_0}{v_0} = \frac{\Delta v_f}{v_0} \quad (12)$$

Equation (12) can be changed into Equation (13):

$$D - d = \frac{\Delta v_f}{v_0} d \quad (13)$$

differentiating Equation (13) with respect to time (14):

$$\frac{\partial(D-d)}{\partial t} = \frac{\Delta v_f}{v_0}\frac{\partial d}{\partial t} \quad (14)$$

Where the left side of Equation (14) is u, and $\partial d/\partial t$ equals to $\partial s/\partial t$. So Equation (14) can be changed into Equation (15):

$$u = -\frac{\Delta v_f}{v_0}\frac{\partial s}{\partial t} \quad (15)$$

Thus, the intumescent heat absorption submodel and intumescent velocity submodel can be incorporated into the following intumescent mathematical model.

2.4. Intumescent mathematical model

Intumescent combustion process is very complicated and the proposed model can not include all of the factors that influence the process. The present mathematical model is based on the conservation of energy with the following simplifiying assumptions: 1 – the model is one-dimensional; 2 – there is no heat exchange between generated gas and char; 3 – the thermal properties such as density, heat capacity, thermal conductivity are independently constant at char layer and virgin layer; 4 – the temperature at the interface of char layer and virgin layer $x = s(t)$ is the intumescence (pyrolysis) temperature; 5 – moisture content is ignored; 6 – intumescent layer is very thin, and turns into char layer quickly, and heat absorption includes pyrolysis heat and intumescent heat absorption.

Preheating stage:

The initial heat transfer mode on the material is dominated by heat conduction (16).

$$\frac{\partial T}{\partial t} = \frac{k_v}{\rho_v c_v}\cdot\frac{\partial^2 T}{\partial x^2} \tag{16}$$

Boundary conditions (17), (18):

$$x = 0,\ k_v\frac{\partial T}{\partial x} = 0 \tag{17}$$

$$x = L,\ k_v\frac{\partial T_v}{\partial x} = a_v\dot{q}'' - h_v(T_s - T_\infty) - \varepsilon_v\sigma(T_s^4 - T_\infty^4) \tag{18}$$

Initial condition (19):

$$t = 0,\ T = T_\infty \tag{19}$$

Intumescent combustion stage:

When the top surface of the sample reaches intumescence (pyrolysis) temperature, intumescence stage starts. The material is divided into three layers: char layer, intumescent layer, virgin layer.

1) Char layer

Energy conservation (20):

$$\frac{\partial T}{\partial t} + u\frac{\partial T}{\partial x} = \frac{k_c}{\rho_c c_c}\cdot\frac{\partial^2 T}{\partial x^2} \tag{20}$$

Boundary conditions (21), (22):

$$x = L(t),\ k_c\frac{\partial T}{\partial x} = a_c\dot{q}'' - h_c(T_s - T_\infty) - \varepsilon_c\sigma(T_s^4 - T_\infty^4) \tag{21}$$

$$x = s(t),\ T = T_p \tag{22}$$

T_s represents the temperature of char layer surface, $s(t)$ represents the location of intumescent layer.

2) Intumescent layer ($x = s(t)$)

Energy conservation (22), (23):

$$k_c\frac{\partial T_c}{\partial t} = k_v\frac{\partial T_v}{\partial t} - \rho_v q_p\frac{\partial s}{\partial t} + u\rho_v q_i \tag{23}$$

Intumescent velocity is equal to Equation (15).

Mass loss rate (24):

$$\dot{m}'' = -(\rho_v - \rho_c)\cdot\frac{\partial s}{\partial t} \tag{24}$$

3) Virgin layer

Energy conservation is equal to Equation (16).

Boundary conditions is equal to Equations (22) and (17).

For preheating stage, the Equations (16), (17) and (18) can be solved by iteration in each time step. The temperature distributions can be predicted quickly, the stability of the equations is reasonably good. The iteration computation can continue till the temperature reaches intumescence temperature. For intumescent combustion stage, two tasks have to do, i.e. to calculate the temperature distribution in the char and virgin layers and to track the intumescence interface. These two tasks were strongly coupled with each other by the boundary conditions. The method used here is to decouple the two tasks by iteration in each time step. The temperature field can be determined by char/virgin energy equations. The intumescence interface can be determined by Equation (23). Then mass loss rates can be calculated by Equation (24). In each iteration step of the decoupling process, the meshes of the sample need to be divided again because of the changeable sample thickness due to intumescence. Numerical results show that numerical calculation of the model is stable and sensitive.

3. Experimental

3.1. Materials

Materials used in the study include polypropylene (PP) supplied by Dalian Petrochemical Corporation; pentaerythritol (PER) supplied by Tianjin BoDi; ammonium polyphosphate (APP) supplied by Haida Chemical; zinc borate (ZB) supplied by Zhenjiang Sulfuric Acid Corporation; polyamide-6 (PA6) supplied by Shanghai Plastics Corporation; montmorillonite (MMT) supplied by Zhejiang Fenghong; zeolite (ZEO) prepared by laboratory.

MMT was used to prepare organic montmorillonite (OMMT) according to literature[18]. PA6 nano was prepared by extruding the mixture of PA6 and OMMT.

3.2. Testing

The FTT cone calorimeter was used for fire testing following the procedure defined in ISO-5660-1.

The standard procedure used involves exposing specimens at heating flux levels of 50 $\mathrm{kW\cdot m^{-2}}$, specimen sizes were 100 mm×100 mm×10 mm. The experiments were conducted in air.

Differential scanning calorimetry NETZSCH DSC204 was used to measure heat capacity at a heating rate of 10 K/min under air atmosphere. Heat capacity was computed using sapphire as reference.

The thermal conductivity of the sample is measured by using hot-wire method on a DRX-I thermal conductivity test instrument following the procedure defined in GB5990-86. The sample was measured from 293 K to 653 K.

4. Results and discussion

Variation of heat capacity versus temperature of intumescent PP is shown in Figure 3, which shows that there are two peaks appeared during heating. When the temperature approaches 440 K, PP begins to melt and heat is absorbed to complete phase change, resulting in a peak, which appears at about 440 K. Then a rapid decrease of heat capacity is observed between 440 K and 460 K. After that, heat capacity remains constant, but another peak appears at 500 K because of the pyrolysis of fire retardant. Figure 4 shows variation of heat capacity versus temperature of char. Heat capacity of char increases gradually when the temperature is below 400 K, then decreases after that, indicating that the char is oxidized exothermally and results in the decrease of heat capacity of char. For simplicity, we take an approximate heat capacity value as the model's input parameter value, that is $C_v = 2600\ \mathrm{J\cdot kg^{-1}\cdot K^{-1}}$, $C_c = 3000\ \mathrm{J\cdot kg^{-1}\cdot K^{-1}}$.

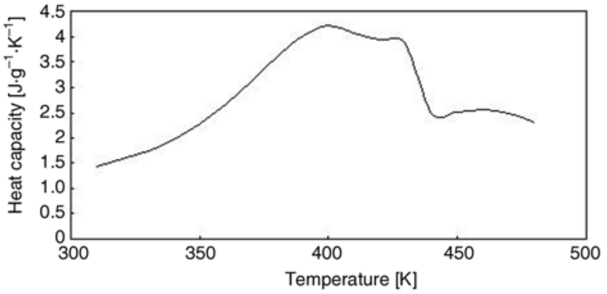

Figure 4. Variation of heat capacity versus temperature of char

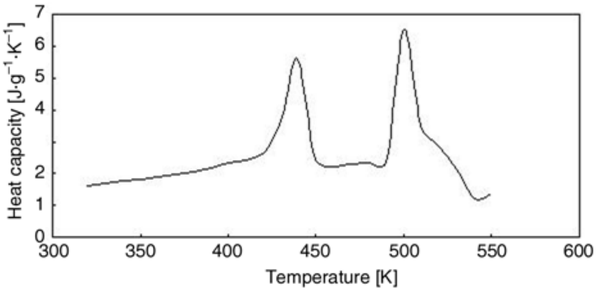

Figure 3. Variation of heat capacity versus temperature of intumescent PP

Variation of thermal conductivity *k versus* temperature of intumescent PP as shown in Figure 5 shows that *k* increases gradually with temperature when below about 373 K. The value of the thermal conductivity initially increases until 373 K then decreases, goes through a minimum at about 553 K and after that increases up to about 653 K. The sample begins to soften when the temperature above 373 K, and melt at about 433 K, which results in a decrease in thermal conductivity of the sample. When the temperature reaches 533 K, PP begins to decompose and generates gases which form some bubbles remaining inside the sample and decrease the thermal conductivity. On the other hand when the temperature goes beyond 573 K, char begins to form, and solid char improves the thermal conductivity of the sample. However, the thermal conductivity of char is still lower than that of the intumescent PP at low temperature. For simplicity, we take an approximate thermal conductivity value as the model's input parameter value, that is $k_v = 0.5\ \mathrm{W\cdot m^{-1}\cdot K^{-1}}$, $k_c = 0.2\ \mathrm{W\cdot m^{-1}\cdot K^{-1}}$.

The value of heat capacity and thermal conductivity based on the previous discussions are used in the model, all input parameters are listed as follows [19, 20]: $k_v = 0.5\ \mathrm{W\cdot m^{-1}\cdot K^{-1}}$; $\rho_v = 900\ \mathrm{kg\cdot m^{-3}}$; $c_v = 2600\ \mathrm{J\cdot kg^{-1}\cdot K^{-1}}$; $k_c = 0.2\ \mathrm{W\cdot m^{-1}\cdot K^{-1}}$; $\rho_c = 200\ \mathrm{kg\cdot m^{-3}}$; $q_p = 1\cdot 10^6\ \mathrm{J\cdot kg^{-1}}$; $h_v = h_c = 10\ \mathrm{W\cdot m^{-2}\cdot K^{-1}}$; $T_p = 600$ K; $a_v = a_c = \varepsilon_v = \varepsilon_c = 0.95$; $T_\infty = 298$ K; $c_c = 3000\ \mathrm{J\cdot kg^{-1}\cdot K^{-1}}$; $\Delta v_f/v_0 = 1.5$; Char yields = 44.09%; $q = 50\ \mathrm{kW\cdot m^{-2}}$.

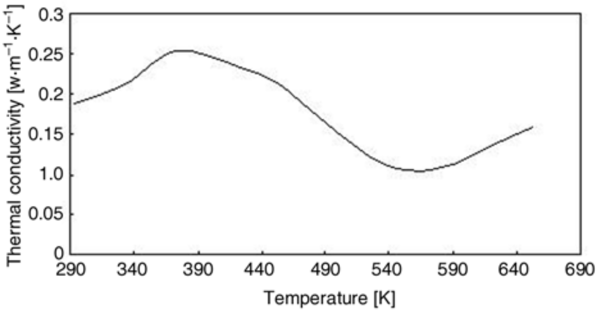

Figure 5. Variation of thermal conductivity versus temperature of the intumescent PP

Predicted temperature curves at 1, 8, 9, 10 mm locations from the bottom for polypropylene sample at incident heat flux of 50 kW·m^{-2} were shown in Figure 6. From the simulation curve, it is clear that when the temperature approaches intumescent temperature, the temperature increased very slowly due to the energy consumption for intumescent reaction. From the numerical prediction, it can be seen that the bending curve during the intumescent reaction was properly predicted by the model. Bending phenomenon is one of the characteristics of intumescent materials during fire. The present model can appropriately describe the intumescent behavior of polymer.

Meanwhile the thicknesses of the intumescent polypropylene during burning were measured for the validation of the model predictions. The validation results showed that the intumescent thicknesses predicted by the model were in fair good agreement with the experimental results as shown in Figure 7.

Figure 8 presents the comparison of the measured mass loss rates with the numerical mass loss rates obtained from the simulations. When the temperature of the sample reaches the pyrolysis temperature, the mass loss rate will increase quickly. The swelling of intumescent layer and the resulting multicellular char-forming limit both the heat transfer from the heat source to the substrate and the mass transfer from the substrate to the heat source, consequently protecting the underlying material. The mass loss rate will decrease after peak mass loss rate. Comparison with experimental results demonstrates that the predictions of mass loss rates are in reasonably good agreement with the experiment.

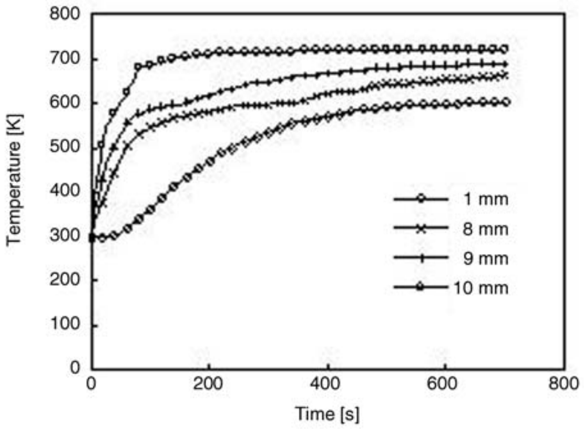

Figure 6. Predicted temperature curves at 1, 8, 9, 10 mm above the bottom of sample at incident heat flux of 50 kW·m^{-2}

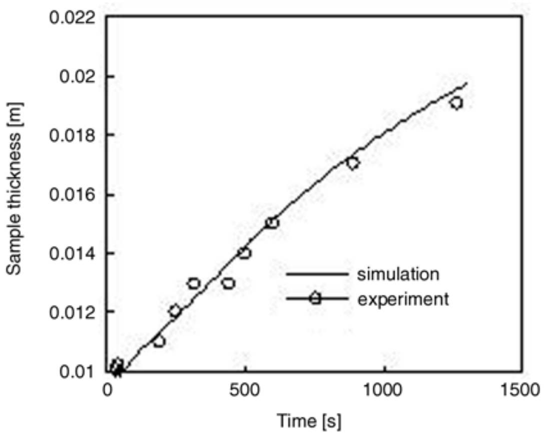

Figure 7. Comparison of measured and predicted materials thickness change with time for polypropylene at incident heat flux of 50 kW·m^{-2}

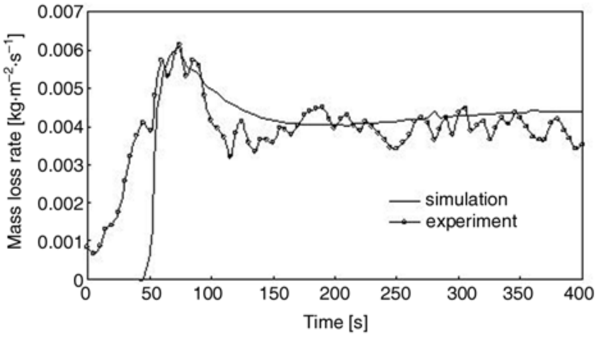

Figure 8. Comparison of the measured and predicted mass loss rates at incident heat flux of 50 kW·m^{-2}

5. Conclusions

A prediction model for the intumescence process in fire for intumescent flame retardant PP was developed. The model emphasizes the thermodynamic aspect of the intumescence process and a corresponding submodel is presented. Some key parameters such as thermal conductivity and heat capacity were measured and found these values would vary with time during experiment.

The validation results showed that the intumescent thicknesses and mass loss rates predicted by the model were in reasonably good agreement with the experimental results. The model was also used to predict the temperature distribution across the sample thickness during burning. The study shows that the present model can appropriately describe the intumescent behavior of polymer and numerically predict their intumescent thickness and temperature distribution in fire.

Acknowledgements

The authors gratefully acknowledge the financial support of China NSFC Funds (No. 50176021) and China Special Doctorate Funds for Colleges and Universities.

Nomenclatures

a – absorbility
c – specific heat capacity [$J\cdot kg^{-1}\cdot K^{-1}$]
D – the final depth of sample
d – the initial depth of sample
h – coefficient of convection heat [$W\cdot m^{-2}\cdot K^{-1}$]
k – thermal conductivity [$W\cdot m^{-1}\cdot K^{-1}$]
L – sample thickness [m]
M – molar weight [$g\cdot mol^{-1}$]
m – mass [kg]
$\dot{m}''$ – mass loss rate [$kg\cdot m^{-2}\cdot s^{-1}$]
n – amount of gas [mol]
P – pressure of gas [Pa]
$\dot{q}''$ – external heat flux [$W\cdot m^{-2}$]
q_p – heat of pyrolysis [$J\cdot kg^{-1}$]
q_i – intumescent heat absorption [$J\cdot kg^{-1}$]
Q – heat absorption [kJ]
R – universal gas constant [$8.314\ kJ\cdot kmol^{-1}\cdot K^{-1}$]
s – intumescent front [m]
T_P – intumescent temperature [K]
t – time [s]
Δt – time step [s]
T – temperature [K]
T_∞ – ambient temperature [K]
u – intumescent velocity [$m\cdot s^{-1}$]
U – internal energy [kJ]
v_0 – initial volume of sample [m^3]
v – volume [m^3]
$\Delta v_f/v_0$ – intumescent ratio
W – work [kJ]
x – coordinates axis [m]
Δx – distance step [m]
ε – emissivity
ρ – density [$kg\cdot m^{-3}$]
σ – Stefan-Boltzmann constant [$5.669\cdot 10^{-8}\ W\cdot m^{-2}\cdot K^{-4}$]
ϕ – porosity

Subscripts

c – char material
g – gas
s – surface of sample
v – virgin material
∞ – ambient

References

[1] Jimenez M., Duquesne S., Bourbigot S.: Multiscale experimental approach for developing high-performance intumescent coatings. Industrial and Engineering Chemistry Research, **45**, 4500–4508 (2006).

[2] Shuklin S. G., Kodolov V. I., Klimenko E. N.: Intumescent coatings and the processes that take place in them. Fibre Chemistry, **36**, 200–205 (2004).

[3] Wei P., Li H., Jiang P., Yu H.: An investigation on the flammability of halogen-free fire retaudant PP-APP-EG systems. Journal of Fire Sciences, **22**, 367–377 (2004).

[4] Bourbigot S., Le Bras M., Dabrowski F., Gilman I. W., Kashiwagi T.: PA-6 clay nanocomposites hybrid as char forming agent in intumescent formulations. Fire and Materials, **24**, 201–208 (2000).

[5] Shih Y. C., Cheung F. B., Koo J. H.: Theoretical modeling of intumescent fire-retardant materials. Journal of Fire Sciences, **16**, 46–71 (1998).

[6] Le Bras M., Bourbigot S., Revel B.: Comprehensive study of the degradation of an intumescent EVA-based material during combustion. Journal of Materials Science, **34**, 5777–5782 (1999).

[7] Di Blasi C.: Processes of flames spreading over the surface of charring fuels: effects of the solid thickness. Combustion and Flame, **97**, 225–239 (1994).

[8] Parker W. J.: Predictions of the heat release rate of Douglas fire. in 'Proceedings of Fire Safety Science, Second International Symposium, Tokyo, Japan' 337–346 (1989).

[9] Anderson C. E., Wauters D. K.: A thermodynamic heat transfer model for intumescent systems. International Journal of Engineering Science, **22**, 881–889 (1984).

[10] Buckmaster J., Anderson C., Nachman A.: A model for intumescent paints. International Journal of Engineering Science, **24**, 263–276 (1986).

[11] Bourbigot S., Duquesne S., Leroy J-M.: Modeling of heat transfer of a polypropylene-based intumescent system during combustion. Journal of Fire Sciences, **17**, 42–56 (1999).

[12] Staggs J. E. J.: A simplified mathematical model for the pyrolysis of polymers with inert additives. Fire Safety Journal, **32**, 221–240 (1999).

[13] Di Blasi C.: Analysis of convection and secondary reaction effects within porous solid fuels undergoing pyrolysis. Combustion Science and Technology, **90**, 315–340 (1993).

[14] Bhargava A., Griffin G. J.: A two dimensional model of heat transfer across a fire retardant epoxy coating subjected to an impinging flame. Journal of Fire Sciences, **17**, 188–208 (1999).

[15] Bulter K. M., Baum H. R., Kashiwagi T.: Heat transfer in an intumescent material using a three-dimensional Lagrangian model. in 'International conference on fire research and engineering. Orlando, Florida USA', 261–266 (1995).

[16] Zhang J., Ji K. J., Xia Y. Z.: Polymer combustion and fire-retardant technology. Chemical Industry Press, Beijing (2005).

[17] Wang Y., Zhang J., Lu X. D.: Simulated effects of melting behavior on combustion process of polymers. The Journal of Qingdao University of Science and Technology, **26**, 312–316 (2005).

[18] Liu J. H., Zhang J., Li F.: Emulsion copolymerized styrene and butyl-crylate/organic-montmorillonite nanocomposites. China Synthetic Rubber Industry, **28**, 90–93 (2005).

[19] Beyler C.: Thermal decomposition of polymers. in 'The SFPE handbook of fire protection engineering' (eds.: Di Nenno P. J., Beyler C. L., Custer R. L. P., Walton W. D., Watts J. M., Drysdale D. D., Hall J. R.), National Fire Protection Association, Quincy, 173–176 (1988).

[20] Sun S. C.: Applied Handbook of Plastics. Zhejiang Science and Technology Press, Hangzhou (1999).

eXPRESS Polymer Letters Vol.1, No.3 (2007) 166–172
Available online at www.expresspolymlett.com
DOI: 10.3144/expresspolymlett.2007.26

Synthesis and properties of a novel pH sensitive poly(N-vinyl-pyrrolidone-co-sulfadiazine) hydrogel

J. Guo, L. Li, Y. Ti, J. Zhu*

School of Chemical Engineering and Technology, Tianjin University, Tianjin 300072, China

Received 6 November 2006; accepted in revised form 7 March 2007

Abstract. Sulfadiazine monomer (SDM) was synthesized by the reaction of sulfadiazine with acryloyl chloride. The SDM was characterized by ^{1}H-NMR and IR spectra. A novel hydrogel with $–SO_2NH–$ group was obtained by the radical copolymerization of SDM with N-vinyl-pyrrolidone (NVP). Effects of the reaction temperature, reaction time, the monomer ratio, and the amount of the cross-linker on the pH sensitivity of the hydrogel were investigated. Results indicate that the hydrogel shows strong pH sensitivity in the pH range of 6.5 to 7.2. It also exhibits a good swelling reversibility at buffer solutions of pH 6.5 and 7.2. At last, drugs tests demonstrated the release effect of the hydrogel in pH range of 6.5 to 7.2.

Keywords: *polymer gels, pH-sensitive, sulfadiazine, N-vinyl-2-pyrrolidone, drug release*

1. Introduction

Hydrogels are three-dimensional polymeric networks in which there are a lot of hydrophilic groups, those swell quickly by imbibing a large amount of water or de-swell in response to changes in their external environment. Some hydrogels can swell or shrink when changing the pH of the environment, because of the existence of the acid/basic groups in the molecular network of the pH-sensitive hydrogel. They have therefore found wide application in the bio-medical materials field, including drug control and release [1], artificial organs [2], and bio-sensor [3], etc. In particular, much attention has been paid in the last twenty years to pH-responsive polymers for drug delivery application. However, pH sensitive range of most hydrogels that contain weak acid group, is between 4 and 6. On the other hand, hydrogels that contains basic group show the sensitivity only above pH 8 [4], which leads to the limitation of the hydrogel application in the body fluid where pH is around 7.4 and changes are within 0.2~0.4 [5]. So copolymerization of monomers that contains weak acidic/basic group with the hydrophobic monomer was attempted in order to adjust the pH sensitive range to the neutral range [6]. Nevertheless, these copolymers can hardly find application in the bio-medical materials field because of the toxicity or the bio-compatibility limitation of the monomer. N-vinyl-pyrrolidone (NVP) is a hydrophobic compound with excellent bio-compatibility, and high polymer surface activity, etc. It is widely used as the blood extender and drug control/release material.

Sulfonamide compounds are the derivatives of p-aminobenzene sulfonamide. The p-aminobenzene sulfonamide was first synthesized in 1908 and then widely applied in the dye industry. It was later used as antimicrobial [7], anticancer reagent [8], and chelating ligand [9], etc. Up to now, more than 5400 sulfonamide compounds have been synthesized and investigated. The sulfonamide group (structure showed in Figure 1) is a weak acid group. Due to the high electronegative attraction of oxygen atoms in $–SO_2NH–$, electrons of the sulfur

---

*Corresponding author, e-mail: jtguo@tju.edu.cn

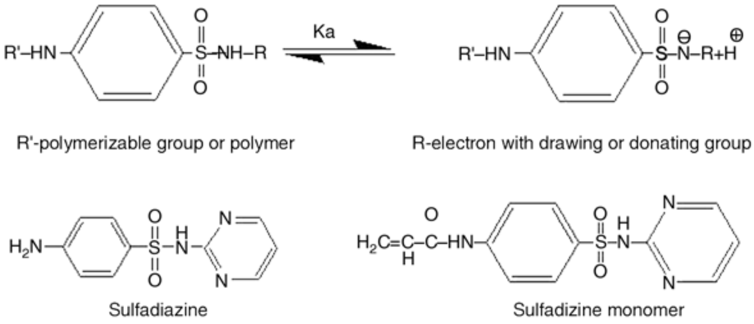

Figure 1. Chemical structures of sulfonamide, sulfadiazine, and sulfadiazine monomer

are attracted, which leads to the movement of the N–H electronic cloud toward the nitrogen atom and results in the ionization. The pK_a value of sulfonamide compounds depends on their substituents and varies in the range of 3~11 [10].

By introducing sulfonamide groups into the hydrogel, it is expected that its swelling property will have severe changes corresponding to the in vivo environment. Herein, we introduced the sulfadiazine with pK_a of 6.8, prepared a novel pH sensitive hydrogel, and investigated its pH sensitivity.

2. Experimental

2.1. Materials

Acryloyl chloride was supplied by Hengyuan Zhongye Limited Company (Beijing,China) and sulfadiazine was supplied by Southwest medicine Co. Ltd, which were used directly. N-vinyl-pyrrolidone (NVP) was supplied by Nankai University Fine Chemicals Factory (Tianjin, China). N,N-methylene-bis-acrylamide (MBA) was supplied by Zhejiang Huangyan Renmin Chemical Engineering Factory, and acrylic acid (AA) was purchased from Tianjin 5th Chemicals Factory. N-vinyl-pyrrolidone, N,N- methylene-bis-acrylamide, and acrylic acid monomers were used after vacuum distilling. 2-2'-azobis-(isobutyronitrile) (AIBN) was purchased from Tianjin 1st Chemicals Factory, which was recrystallized from methanol. Other chemicals were of analytical grade and used without any pretreatment.

2.2. Instruments

Following instruments were used for characterizations: FTIR (FTS3000, BIO-RAD, USA), pellets were made with KBr by pressing; NMR (AV400, Bruker) with DMSO-d6 as solvent; constant temperature water bath vibration machine (SHZ-88); SEM (Panasonic X-650).

2.3. Synthesis of the monomer

The preparation method of the SDM was the same as described in the literature [11]. In brief, sulfadiazine (5.3 g) was dissolved in 40 ml water/acetone (1:1 v/v) solvent, which contains 0.8 g sodium hydroxide, and poured into a four-neck flask with stirring device, condensing tube, and thermometer. The flask was placed in an ice-water bath and the reaction temperature was kept under 5°C. When the temperature became stable, the acryloyl chloride (2.5 ml) was added to the mixture with constant stirring and the temperature was kept under 10°C for 3 hrs. The precipitated product was washed with distilled water for three times. Fine yellow powder was obtained after drying in vacuum at room temperature for 24 hrs. The synthetic route is shown in Figure 2.

2.4. Preparation of the hydrogel

Poly(SDM-co-NVP) hydrogel was synthesized by free radical copolymerization of SDM(1.82 g), NVP(1.56 g), MBA(0.03 g), and AIBN(0.018 g) in DMSO. The synthetic route is shown in Figure 3. The polymerization proceeded for 10 hrs at 55°C

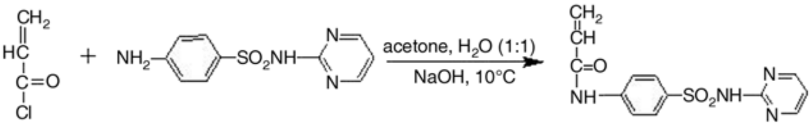

Figure 2. The synthetic route of SDM

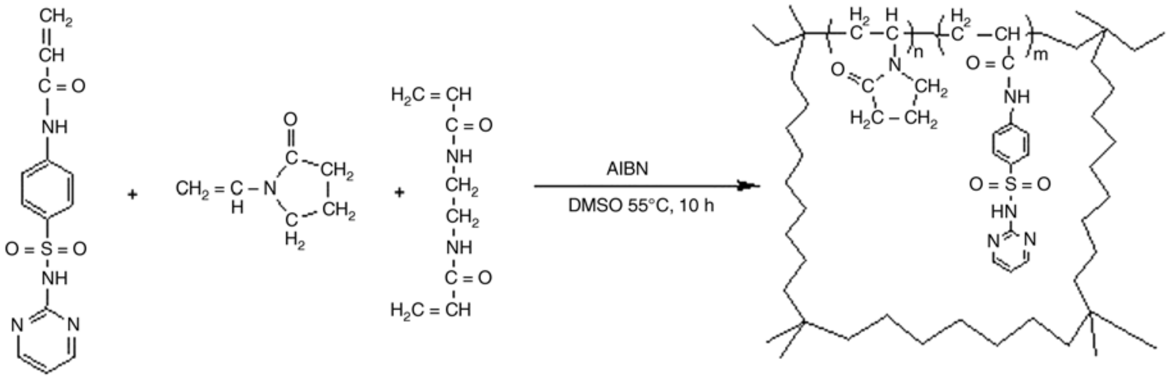

Figure 3. Chemical structures of gel components and the synthetic route of the hydrogel

under a nitrogen atmosphere. The synthesized hydrogel was separated from the tube and soaked in ethanol for 30 min. It was then immersed in an aqueous sodium hydroxide solution (pH 8) for 2 days and followed by soaking in aqueous hydrogen chloride solution (pH 3) for 1 day. Finally, the hydrogel was washed using deionized water for several times and dried in vacuum at 40°C for 2 days.

2.5. Swelling measurement

The swelling ratio (SR) of hydrogels was measured at 37°C in buffer solutions and pH varying from 4.0 to 9.0. 0.2 M $KHC_8H_4O_4$/0.1 M NaOH was used as pH 4.0–5.5 buffer, 0.2 M KH_2PO_4/0.1 M NaOH for pH 5.8–8.0 buffer, and 0.025 M $Na_2B_4O_7$/0.1 M HCl for the rest of pH value buffers. The total ionic strength of each buffer was adjusted to 0.2 M with calculated amount of 0.1 M NaCl. The incubation time was approximately 2 days. Periodically, gels were withdrawn from the buffer solution and weighed after removal of excessive surface water by lightly blotting with a filter paper. The weight-swelling ratio (SR) was calculated by Equation (1):

$$\mathrm{SR} = \frac{W_{swollen} - W_{dry}}{W_{dry}} \tag{1}$$

where $W_{swollen}$ and W_{dry} are weights of the fully swollen gel and dried gel, respectively.

2.6. In vitro release studies

The chloramphenicol was used as the standard drug in the drug release experiment. 50 mg chloramphenicol was dissolved in 20 wt% ethanol and adjusted to 50 ml. 0.1~0.8 ml (with 0.1 ml interval) solution were taken from above solution and diluted to 25 ml. The light absorption degree was measured by WFZ-26A UV spectrophotometer and the standard calibration curve of the chloramphenicol was obtained. Its linear regression equation is $C = 0.05396A + 4.81022e - 4$ ($R = 0.9994$, $p < 0.0001$).

Dry hydrogels were immersed in a concentrated ethanol solution of chloramphenicol and left soaking for 2 days at room temperature. After this period, the hydrogels were rapidly washed with ethanol and dried to a constant weight. The loaded amount of drug in hydrogel disk is defined as Equation (2):

$$\text{Loaded amount of drug} = W_{p+d} - W_p \tag{2}$$

where W_{p+d} is the weight of a dried disk after the drug is loaded, and W_p is the weight of the dried disk before the drug is loaded.

Drug-loaded hydrogels (25 mg) were placed in dialysis bags and those bags were placed in flasks containing 50 ml buffer solutions (pH 6.5). The drug-release experiment was carried on in a SHZ-88 water bath shaker incubator with reciprocating motion (100 rpm). Equal portions were withdrawn and assayed with UV spectrophotometer every other hour. After each sampling, an equal volume of fresh buffer solution was added as release medium. The sample was quickly moved to another buffer solution (pH 7.2) after 4 hrs to continue the release experiment. All the release determinations were carried out in triplicate.

3. Results and discussion

3.1. Structure characterization of SDM

To investigate the structure of sulfadiazine monomer, IR spectra of sulfadiazine and sulfadi-

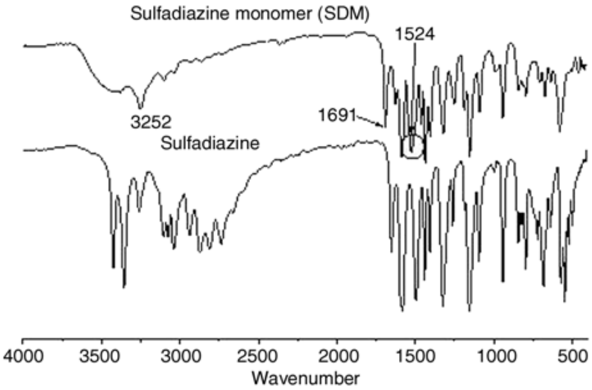

Figure 4. IR spectra of sulfadiazine and sulfadiazine monomer

azine monomer were recorded as shown in Figure 4. The IR spectrum of sulfadiazine reflects that the $–NH_2$ vibration absorption peaks are at 3424 $cm^{–1}$, 3356 $cm^{–1}$, and 3259 $cm^{–1}$. However, the IR spectrum of the sulfadiazine monomer shows only one strong absorption peak at 3252 $cm^{–1}$, which indicates that the $–NH_2$ is not existent. Peaks at 1691 $cm^{–1}$ and 1524 $cm^{–1}$ are the characteristic absorption peaks of the –CONH– group. The symmetric and asymmetric vibration absorption peaks of $–SO_2–$ can be observed in both IR spectra of sulfadiazine and sulfadiazine monomer at 1322 $cm^{–1}$ and 1154 $cm^{–1}$. Figure 5 shows the ^1H NMR (400 MHz, DMSO-d6) spectrum of sulfadiazine monomer with δ = 5.8, 6.3 (s, 2H, $CH_2–C$), 6.55 (s, 1H, $CH_2–CH$), 7.0, 8.55 (s, 3H, pyridine-H), 7.82, 7.94 (d, 4H, benzene-H), 10.4 (s, 1H, –CONH–), 11.7 (s, 1H, $–SO_2NH–$). When combining both the NMR and the IR spectra of SDM, it is indicated that the SDM is generated from the reaction of sulfadiazine with acryloyl chloride. The results of the NMR and the IR spectra coincide with the previous results [11, 12].

3.2. SEM studies

The dry blank hydrogel was placed on the glass substrate and coated with gold. Its surface morphology and cross-sectional view were observed under SEM. Figure 6a shows that the surface of the blank hydrogel is smooth. Figure 6b shows that the hydrogel has big hollow canal-like structure, which indicates its suitable application in drug loading.

3.3. pH sensitivity of the hydrogel

3.3.1. Effect of temperature on pH sensitivity

Temperature is a crucial factor when the hydrogel is synthesized by free radical copolymerization. It can be observed from Figure 7 that the higher the copolymerization temperature, the lower the

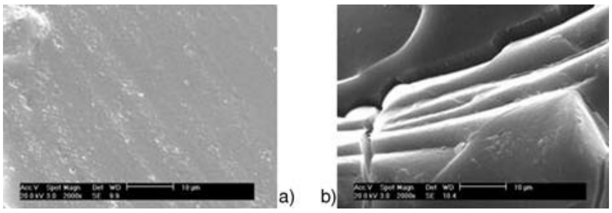

Figure 6. SEM images of blank hydrogels: a) the surface morphology; b) the cross-sectional view

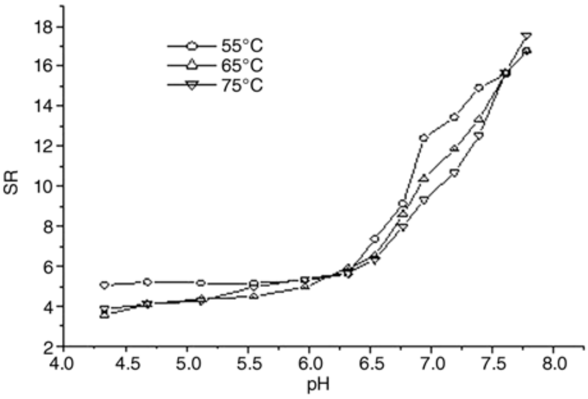

Figure 7. Effect of temperature on pH-sensitivity of hydrogel

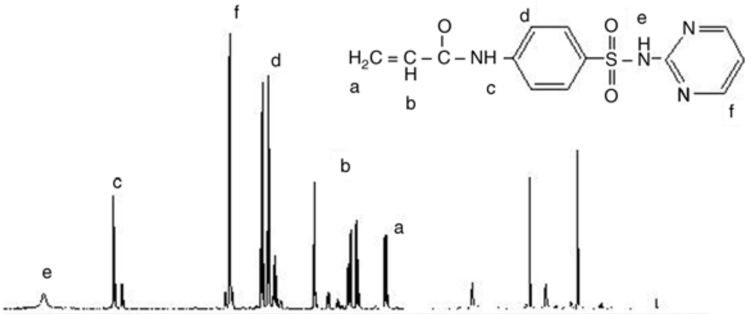

Figure 5. ^1H NMR spectrum of sulfadiazine monomer in DMSO-d6

swelling degree of the hydrogel under the acidic condition. Due to the increasing of the temperature, the decomposition rate of the AIBN increased, which increases the copolymerization rate. The network formation under these conditions is relatively complete. Therefore, the crossing degree of the polymer is higher but the swelling degree is lower. Within the pH range of 6.5 and 7.2, poly(NVP-co-SDM) hydrogel has excellent pH sensitivity, when the copolymerization temperature increases, the pH sensitivity of the hydrogel decreases. This is possibly due to the suitable decomposition rate of AIBN at 55°C, which results in the formation of a homogeneous hydrogel structure. When the temperature rose to 65°C or 75°C, the AIBN rapidly decomposes which affects the structure of the hydrogel and decreases its mechanical property due to the existing bubbles (N_2 from the decomposition) in the hydrogel.

3.3.2. Effect of reaction time on pH-sensitivity

The reaction time directly affects the copolymerization reaction. In order to assure the lowest residual monomer amount in the final hydrogel product, enough reaction time must be provided to complete the reaction. Figure 8 shows that effect of the reaction time on pH-sensitivity of the hydrogel. The reaction time of the hydrogels is 6 h, 8 h and 10 h in Figure 8. From the trends of the swelling curves, it is revealed the swelling ratio of the hydrogels increase slowly under lower pH 4.0~6.3, whereas it increases rapidly and reaches the highest under higher pH ,which reveals high pH sensitivity of the hydrogel. The hydrogel whose reaction time is 10 h shows the highest PH sensitivity, and its swelling degree changes the most distinctly due to its complete and homogeneous structure, that is, it is more pH sensitive.

3.3.3. Effect of different amount of monomers

Poly(NVP) hydrogel and samples with the molar ratio of SDM to NVP 1/8, 2/8, 3/8 were synthesized at the same condition in order to compare the effect of the monomers ratio to pH sensitivity of the hydrogel. The pH sensitivity measurement results are shown in Figure 9. It is indicated that the swelling property and pH sensitivity have been greatly improved after introducing the SDM, especially between pH 7.0~7.5. When the molar ratio of SDM to NVP is 1/8, 2/8, as the amount of the SDM increases, pH sensitivity of the hydrogel increases as well. On the other hand, pH sensitivity becomes obvious only at higher pH values when only a small amount of the SDM is introduced. For the hydrogel contains 3/8 SDM, it shows similar pH sensitivity and the swelling degree as the 2/8 SDM hydrogel.

3.3.4. Effect of different amount of the cross-linker

The amount of the cross-linker also affects the swelling property of the hydrogel. Here, we investigated the effect of different amount of cross-linker on pH sensitivity of the hydrogel, as shown in Figure 10. It is shown that polymer with complete network structure can be formed when a significant amount of the cross-linker was added. Such formulated polymer has high cross-linking degree and low swelling degree. However, when excess amount of cross-linker is applied, the yielded

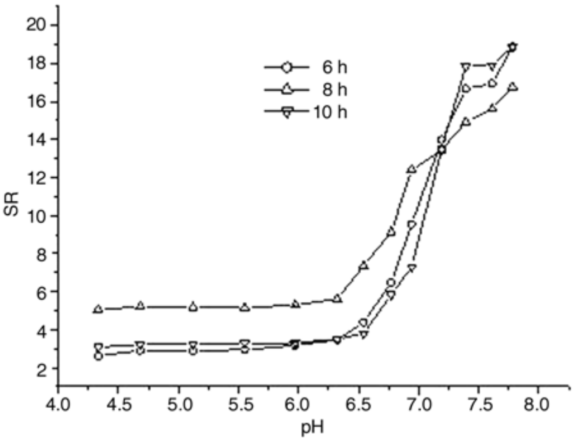

Figure 8. Effect of reaction time on pH-sensitivity of hydrogel

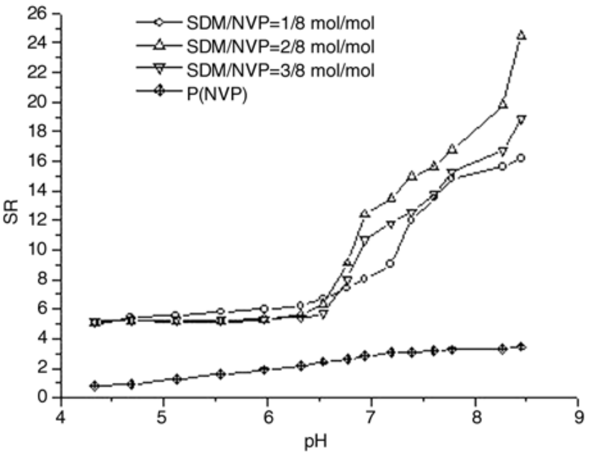

Figure 9. Effect of different amount of monomers on pH-sensitivity of hydrogel

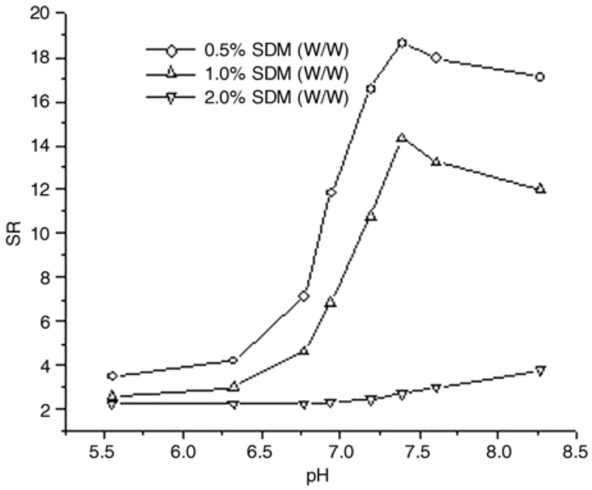

Figure 10. Effect of amount of cross-linker on pH-sensitivity of hydrogel

hydrogel is brittle and rigid. Even if it is immersed in the solvent for a long time, the cross-link network cannot be expanded completely. After the ionization of –SO_2NH–, the network cannot be further expanded due to the electrostatic repulsion. Hence, it shows low pH sensitivity. When lower amount of the cross-linker is used, the hydrogel formed has better swelling property and pH sensitivity, but with lower strength and poor mechanical property. Hence, proper amount of cross-linker should be applied.

Here we chose 1wt% cross-linker to SDM. Both the swelling property and pH sensitivity of the obtained hydrogel are ideal.

3.4. Swelling-deswelling-reswelling kinetics

The reversibility in swelling and swelling/deswelling kinetics of hydrogels is demonstrated as shown in Figure 11 in two different pH buffer solutions at 37°C. The cycle started from a dry polymer, followed by repeated cycles between two fixed pH values.

It shows that the hydrogel was swelling when the pH was equal to 7.2. On the contrary, the deswelling process was exhibited when the hydrogel was transferred to the buffer solution of pH 6.5. Therefore, the hydrogel synthesized from SDM and NVP has excellent response to small pH changes and its swelling process is reversible.

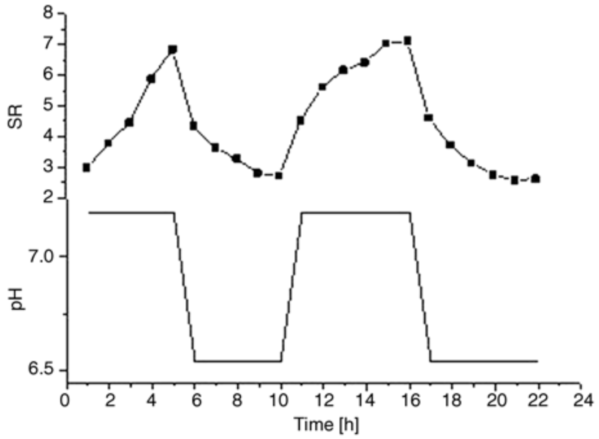

Figure 11. Swelling reversibility test of hydrogels as a function of time at 37°C under repeated changes in pH between 7.2 and 6.5

The pH sensitivity measurements of the hydrogel show that the ionization of –SO_2NH– in the weak base environment can be shown as Figure 12.

There are considerable amounts of –SO_2NH– groups in the network of this polymer. Due to the electrostatic repulsion, the cross-link network expands and swelling degree increases rapidly. Hence, it shows great pH sensitivity. Foregoing researches also revealed its excellent pH sensitivity in between the pH range of 6.5 to 7.2.

3.5. Release behavior of the hydrogel

A more reliable and informative analysis can be obtained considering that in swellable polymers two phenomena affect the solute release: the swelling property of the hydrogel and the rate of drug-dissolution from the polymer. For the investigation of drug-release behavior of P(SDM/NVP) hydrogels, drug loading experiments were firstly conducted in 1 mg/ml of chloramphenicol ethanol solution. Loading amount of the drug is 1.6 mg in 0.1 g hydrogels.

Figure 13 shows that the drug is released slowly as the hydrogel gradually swells. The drug release shows an increasing trend in the releasing curve. Once the sample was moved to the pH 7.2 buffer solution, there is a sudden release which can be

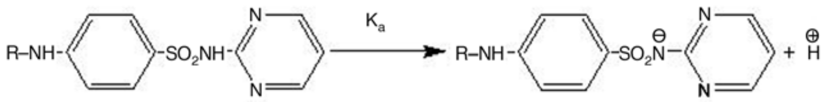

Figure12. The ionization of –SO_2NH–in the weak base environment

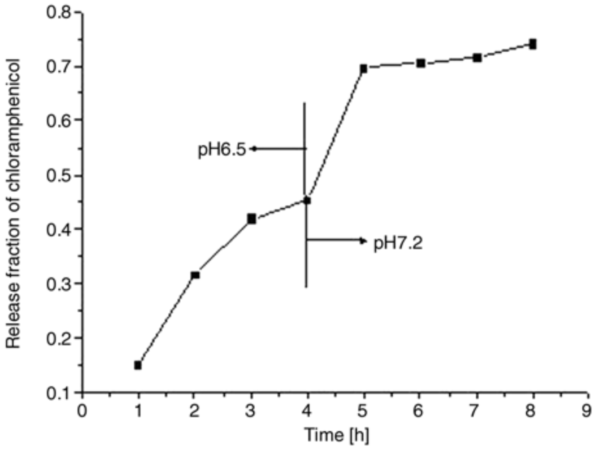

Figure 13. Release of chloramphenicol from hydrogels (37°C)

observed from the curve as a rapid increase of the slope. In Figure 13, the drug release ratio in pH 6.5 buffer solution is 41%; when the hydrogel is transferred to pH 7.2 buffer solution, the release ratio increases to 70%. The drug release experiment demonstrates the excellent pH sensitivity of the synthesized hydrogel.

4. Conclusions

By introducing SDM in P(NVP) hydrogel, a novel pH sensitive hydrogel, poly(NVP/SDM), was synthesized. SEM images show that this hydrogel has canal-like structure, which is favorable in application of drug release. pH sensitivity measurements reveal that the hydrogel shows strong sensitivity in between pH 6.5 and 7.2. It exhibits excellent swelling reversibility in the above pH range at 37°C. Drug release investigation also demonstrates that the hydrogel has strong sensitivity to pH changes.

References

[1] Peppas N. A., Langer R.: New challenges in biomaterials. Science, **263**, 1715–1720 (1994).
[2] Jeong B., Gutowska A.: Lessons from nature: stimuli responsive polymers and their biomedical application. Trends in Biotechnology, **20**, 305–311 (2002).
[3] Kikuchi A., Okano T.: Intelligent thermoresponsive polymeric stationary phases for aqueous chromatography of biological compounds. Progress in Polymer Science, **27**, 1165–1193 (2002).
[4] Qiu Y., Park K.: Environment-sensitive hydrogels for drug delivery. Advanced Drug Delivery Reviews, **53**, 321–339 (2001).
[5] Shiroya T., Tamura N., Yasui M., Fujimoto K., Kawaguchi H.: Enzyme immobilization on thermosensitive hydrogel microspheres. Colloids and Surfaces B: Biointerfaces, **4**, 267–274 (1995).
[6] Kalpana R., Park K., Park K.: Biodegradable hydrogels in drug delivery. Advanced Drug Delivery Reviews, **11**, 59–84 (1993).
[7] Li Z., Ramay H. R., Hauch F. D., Xiao D. M., Zhang M. Q.: Chitosan-alginate hybrid scaffolds for bone tissue engineering. Biomaterials, **26**, 3919–3928 (2005).
[8] Hoffman A. S.: Hydrogels for biomedical applications. Advanced Drug Delivery Reviews, **54**, 3–12 (2002).
[9] Zhang X. Z., Lewis P. L., Chu C. C.: Fabrication and characterization of a smart drug delivery system: microsphere in hydrogel. Biomaterials, **26**, 3299–3309 (2005).
[10] Gupta P., Vermani K., Garg S.: Hydrogels: from controlled release to pH-responsive drug delivery. Drug Discovery Today, **7**, 569–579 (2002).
[11] Kang S. I., Na K., Bae Y. H.: Sulfonamide containing polymers: a new class of pH-sensitive polymers and gels. Macromolecular Symposia, **172**, 149–156 (2001).
[12] Park S. Y., Bae Y. H.: Novel pH-sensitive polymers containing sulfonamide groups. Macromolecular Rapid Communications, **20**, 269–273 (1999).

eXPRESS Polymer Letters Vol.1, No.3 (2007) 173–179
Available online at www.expresspolymlett.com
DOI: 10.3144/expresspolymlett.2007.27

Effect of the structure of ethylene-propylene-diene-graft-polystyrene graft copolymers on morphology and mechanical properties of SAN/EPDM blends

A. Ptiček, Z. Hrnjak-Murgić, J. Jelenčić*

Faculty of Chemical Engineering and Technology, University of Zagreb, P.O. Box 177, 10000 Zagreb, Croatia

Received 25 January 2007; accepted in revised form 6 March 2007

Abstract. Ethylene-propylene-diene-graft-polystyrene (EPDM-g-PS) copolymers were synthesized to obtain different structures of graft copolymers with different graft lengths and graft densities. The structure of synthesized EPDM-g-PS copolymers was characterized by gel permeation chromatography (GPC) and by Fourier transforms infrared spectroscopy (FTIR). These presynthesized graft copolymers were added (5 phr) to styrene-acrylonitrile (SAN) and ethylene-propylene-diene (EPDM) blends, prepared to maintain the following SAN/EPDM ratios a) 95/5 and b) 90/10. SAN/EPDM blends were characterized by the determination of mechanical properties (tensile strength, elongation at break) while their morphology was inspected by scanning electronic microscopy, SEM. The obtained results show that various structures of EPDM-g-PS copolymers influence the miscibility in SAN/EPDM blends. Optimal concentration of side branches of graft copolymers provide the finest morphology and enhance mechanical properties.

Keywords: *mechanical properties, graft copolymer, styrene-acrylonitrile, ethylene-propylene-diene monomer, morphology*

1. Introduction

Combining two polymers by blending is one of the most favourite techniques used to generate new polymeric materials, as confirmed by the available literature on polymer blends abounding in data on immiscible systems [1–5]. Most incompatible polymer blends often manifest high interfacial tension and weak adhesion at the interfaces between the dispersed phase and the matrix. That results in inferior mechanical properties as well as coarse and unstable morphology. Compatibility of such blends can be enhanced by the addition of an appropriate presynthesized block or graft copolymers [6, 7] with different segments, having affinity for either of the two blend components.

Graft copolymers have a wide range of application owing to the possibility of tailoring their properties trough a combination of monomers that form the backbone and side chains. One can thus obtain thermoplastic elastomers by combining a soft polymer backbone with hard polymer grafts, or vice-versa [8]. The obtained structure of graft copolymers with several branches significantly differs from the linear structure due to its high segment density which considerably affects the crystallization process, as well as, the final mechanical and viscoelastic properties. The addition of a small amount of graft copolymer to an immiscible polymer blend is often a powerful means to increase interaction between the phases, and thus enhance the mechanical properties due to the formation of a strong interface. The graft copolymer used as a compatibilizer tends to be located at the interface of two components and improves adhesion by the 'bridge' effects of the chains [9, 10].

---

*Corresponding author, e-mail: zhrnjak@marie.fkit.hr

In order to obtain different structures of graft copolymers (graft densities), the use of various types of coagents has become popular in many investigations [11]. Thus, the participation of a small amount of coagent (triallylcyanurate, TAC) will suppress the grafting reaction at the tertiary C-atom of the main chain of the EPDM polymer, which leads to a diminished grafting efficiency [12]. The diversity of possible structures along with the adequate selection of the main backbone facilitates the process of tailoring of the properties of graft copolymers. Grafting reactions could induce significant changes in the polymer chain like the chemical composition, the polymer chain structure, the size of molecular masses and these parameters are responsible for the interactions between polymers.

The aim of this work was to investigate the effect of various structures of presynthesized EPDM-g-PS copolymers on interactions between SAN and EPDM polymers in blends. The effect of dissimilar graft copolymers structures on compatibility in blends was followed by the examination of morphology and the determination of mechanical properties.

2. Experimental

2.1. Materials

Polymers used for the synthesis of graft copolymers were ethylene-propylene-diene (EPDM, Keltan 312, DSM) containing 55 wt% ethylene and 4 wt% ethylidene norbornene, Mooney viscosity 36 MU, monomer styrene (St) 99.8 wt% was supplied by DIOKI (Croatia), and the triallylcyanurate (TAC; purity: 50 wt%) which was used as coagent, was purchased to Bayer. Polymers used for the preparation of studied blends, were the above described EPDM and styrene-acrylonitrile (SAN, Tyril 790, The Dow Chemical Company) with 24 wt% AN, the melt flow rate (MFR, measured at 220°C, using a load of 10 kg) was 22 g/10 min.

2.2. Preparation of samples

Graft copolymers were prepared by in-situ polymerization by adding monomer styrene (45.97 cm^3) to a toluene solution of the EPDM polymer (10 g). Dibenzoyl-peroxide (0.39 g) was used as an initiator and the reaction was carried out at 90°C. One series of graft copolymers was synthesized for various polymerization times (3 and 7 hours) while the second series was synthesized with the addition of coagent TAC (1.5 phr) in order to design different structures of graft copolymers. After the synthesis, EPDM-g-PS copolymers were separated from the polymerization solution by Soxhlet extraction in tetrahydrofurane for 8 hours [13]. Extracted graft copolymers were further used as compatibilizer (5 phr) in SAN/EPDM blend compositions 95/5 and 90/10. Studied blends were prepared as thin films (1 mm) cast from 6 wt% toluene solution; their compositions are listed in Table 1. The grafting efficiency was determined on the basis of polymer weight and the total amount of EPDM-g-PS formed, respectively (Equation 1).

$$\text{grafting efficiency}\,[\%] = \frac{\text{weight of EPDM-g-PS}}{\text{total weight of polymers formed}}\cdot 100 \qquad (1)$$

3. Characterization

3.1. GPC measurements

The molecular masses ($\overline{M}_m$, $\overline{M}_w$) of extracted graft copolymers were determined by gel permeation chromatography (GPC) (Polymer Laboratories, PL-GPC 20) using dilute polymer solutions (c = 10 mg/5 ml) in THF at room temperature at a rate of 1 ml/min.

3.2. FTIR spectroscopy

FTIR spectra were recorded on a Perkin-Elmer Spectrum One, in the range of 4000–500 cm^{-1}, with

Table 1. Composition of SAN/EPDM/EPDM-g-PS blends

Samples	SAN/EPDM [phr]		SAN/EPDM-3* [phr]				SAN/EPDM-7* [phr]			
SAN	95	90	95	95	90	90	95	95	90	90
EPDM	5	10	5	5	10	10	5	5	10	10
EPDM-g-PS	–	–	5	–	5	–	5	–	5	–
EPDM-g-PS + TAC	–	–	–	5	–	5	–	5	–	5

*samples prepared with EPDM-g-PS copolymers synthesized for 3 and 7 hours resolution of 4 cm^{-1}. Samples were prepared as thin films cast from 6% toluene solution. The absorbance of vibrations at 1453 and 1493 cm^{-1} due to the polystyrene aromatic groups in the graft copolymer was followed. The absorbance of (–CH_2–) rocking vibrations of the EPDM main chain at 722 cm^{-1} was used as an external standard to eliminate the differences in thickness of the recorded samples.

3.3. Mechanical properties

The mechanical properties of blends were tested using a Zwick Testing Machine (model 1445) at a constant temperature of 23°C and the humidity of 70% RH. The gauge length of 45 mm, crosshead speed of 1 mm/min and sample size (75×13×1 mm) were used to determine of tensile strength and elongation at break. The results are the average of five samples.

3.4. Scanning Electron Microscopy (SEM)

Morphology of examined blends was characterized by a cross-section of cryogenically fractured surfaces of film samples (1 mm thick) using a Philips XL 30 Scanning Electron Microscope. The samples were immersed in liquid nitrogen to cool down for more than 15 min, and then fractured immediately. The dried samples were sputter-coated with gold prior to scanning electron microscopy (SEM) examination.

4. Results and discussion

4.1. Characterization of presynthesized EPDM-g-PS copolymers

The grafting mechanism proceeds with the formation of radical centers in the EPDM chain by breaking the double bond in the third monomer (ENB in EPDM) and in the tertiary C-atom by the abstraction of secondary hydrogen, Figure 1a. At these two active centers of the backbone it is possible to create a modified structure of graft copolymers by: a) extending the polymerization time, and b) adding the coagent TAC. It is expected that with the extended polymerization time the number of side branches would increase, Figures 1b, 1c, whereas in the presence of the coagent TAC the number of side branches would decrease Figures 2b, 2c. The results of grafting efficiency and the molecular masses of synthesized graft copolymers confirmed this assumption, Table 2. The grafting efficiency increase is due to an increasing number of grafting points along the backbone of EPDM. For example, the grafting efficiency at 3 hours of polymerization was 35.6% and at 7 hours 58.5%.

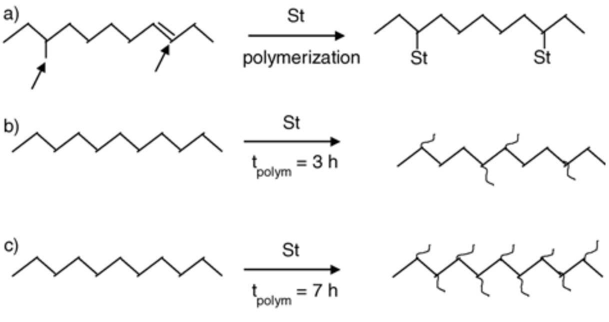

Figure 1. a) possible grafting locations, b) graft density of side branches after 3 hours, c) graft density of side branches after 7 hours

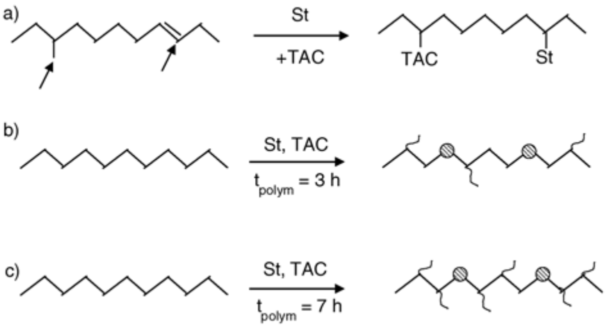

Figure 2. a) suppresion of grafting, b) graft density of side branches after 3 hours, c) graft density of side branches after 7 hours (◍– active centers blocked by TAC)

The results of determined molecular masses of synthesized EPDM-g-PS copolymers, Table 2, show that the values increased due to a continuous decomposition of the initiator during the reaction time. A significant increase in the values of molecular masses ($\overline{M_n}$ = 26 200 of the EPDM-g-PS-3 and $\overline{M_w}$ =54 000 of the EPDM-g-PS-7) was obtained because during the polymerization side branches

Table 2. Characterization of synthesized EPDM-g-PS copolymers

Samples	Grafting efficiency [%]	$\overline{M}_n$	$\overline{M}_w$
EPDM virgin	–	95 000	313 000
EPDM-g-PS-3[a]	35.6	15 900	26 200
EPDM-g-PS-7[a]	58.5	35 000	54 000
EPDM-g-PS-3-T[b]	31.9	14 800	25 800
EPDM-g-PS-7-T[b]	43.8	20 000	42 000

[a] graft copolymers synthesized without TAC
[b] graft copolymers synthesized with TAC

continuously are formed and an increase in the free molecular volume of the graft copolymer was present. The increase in weight molecular mass, $\overline{M_w}$, implies a higher graft density, i.e. higher concentration of side branches [14] and that is the result of a higher degree of branching and a higher number of conformations.

The influence of coagent TAC on graft composition can be seen from the results of the grafting efficiency. Significant decrease in grafting efficiency was observed for the graft copolymers synthesized without coagent TAC (58.5% for 7 h of polymerization) in comparison with graft copolymers synthesized with coagent (43.8% for 7 h of polymerization). These results are explained by 'blocking' the active centers (tertiary C-atom) on the EPDM chain by the coagent TAC, because the rate of reaction of TAC with backbone is faster than the rate of grafting, Figure 2a [15]. The result is a lower graft density of synthesized graft copolymers, as shown by the results relating to the grafting efficiency. Various conditions of graft polymerization lead to the creation of a different structure of graft copolymers, which is also supported by the results of the FTIR characterization.

The grafting reaction of polystyrene on the main EPDM chain was studied via aromatic groups which caused the absorbance of vibrations at 1453 and 1493 cm^{-1}, Figure 3. The higher concentration of polystyrene branches present in graft copolymers resulting as higher values of absorbance, which were calculated from the FTIR spectra. The values of absorbance in the EPDM-g-PS-7 copolymer were $A_{1453} = 1.01$ and $A_{1493} = 0.55$, while in the EPDM-g-PS-7-T they were $A_{1453} = 0.86$ and $A_{1493} = 0.48$, respectively. An addition of the coagent TAC prevents bonding of polystyrene groups onto EPDM chain, resulting in lower values of absorbance and these results also indicate certain differences in the grafting density.

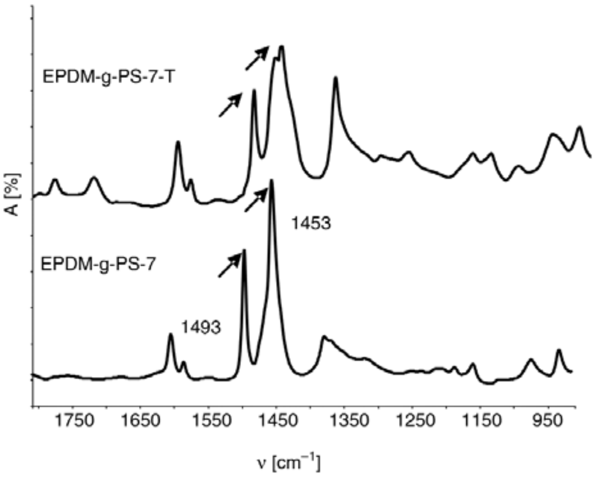

Figure 3. FTIR spectra of graft copolymers synthesized for 7 hours (EPDM-g-PS-7) and for 7 hours with the coagent TAC (EPDM-g-PS-7-T)

4.2. Mechanical properties of the SAN/EPDM/EPDM-g-PS blends

The mechanical properties, tensile strength and elongation, of SAN/EPDM blends obtained by presynthesized EPDM-g-PS copolymers are given in Figures 4 and 5. The standard deviation of the measured results of mechanical properties was in the range ±(0.1–0.7). The first series of blends, denoted as SAN/EPDM-3, SAN/EPDM-7, were prepared by adding of graft copolymers synthesized for 3 and 7 hours. Samples denoted as SAN/EPDM-3-T, SAN/EPDM-7-T were prepared by adding graft copolymers synthesized in the presence of the coagent TAC as the second series, Table 1.

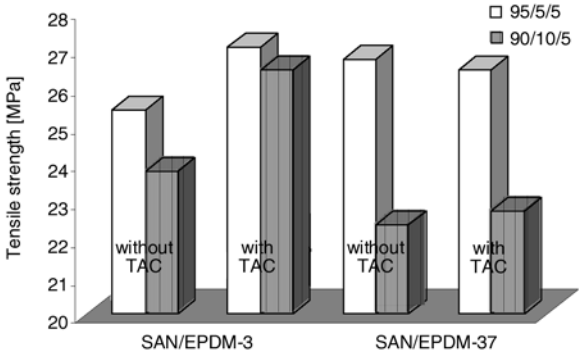

Figure 4. Tensile strength of SAN/EPDM-3, SAN/EPDM-7, SAN/EPDM-3-T and SAN/EPDM-7-T blends compositions 95/5/5 and 90/10/5

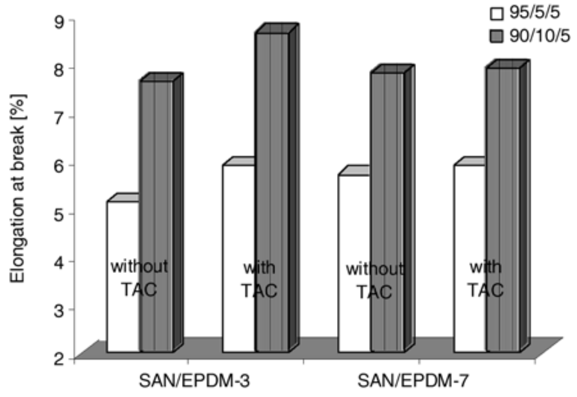

Figure 5. Elongation of SAN/EPDM-3, SAN/EPDM-7, SAN/EPDM-3-T and SAN/EPDM-7-T blends compositions 95/5/5 and 90/10/5

It is a well known fact [16] that SAN and EPDM polymers are incompatible due to the dissimilarity of chemical structure which exhibits poor mechanical properties of blends. Mechanical properties can be improved by adding an interfacial agent to enhance adhesion due to better interaction between the phases. The effect of compatibilizers on mechanical properties is well seen in blend compositions 90/10 because various structures of presynthesized graft copolymers show different influence on the compatibility in SAN/EPDM blends. Optimal mechanical properties are obtained for sample SAN/EPDM-3-T (90/10/5) prepared by a compatibilizer synthesized with the coagent TAC, which implies a lower concentration of side branches, Figure 2b. Considering the sample prepared with the graft copolymer synthesized for 3 hours without the coagent in comparison with the sample SAN/EPDM-3-T (prepared with coagent TAC), different structure is observed, i.e. a higher concentration of side branches, Figure 1b, and a weakening of mechanical properties of the blends are obtained. The similar behavior is observed for the extended polymerization time (7 hours) of synthesis of graft copolymers, i .e. increase of concentration of side branches, which caused continued weakening in mechanical properties of the blends. For example, tensile strength for the sample SAN/EPDM-3 (prepared with coagent TAC) was cca. 27 MPa while for the sample SAN/EPDM-7 this value decreased to 22.5 MPa, Figure 4. From that it can be concluded that the concentration of side branches, i.e. graft density is responsible for interactions between the polymers in a blend. However, there are negligible differences in the mechanical properties of blends when these are prepared with compatibilizers synthesized for 7 hours (with and without TAC), Figures 1c, 2c. In this case, it is assumed that when the concentration of side branches is higher then optimal, then the effect of the different structures of the graft copolymers on miscibility would not be observed. Considering the sample composition 95/5/5 it can be seen that addition of compatibilizer improves compatibility but the effect of different structures of the graft copolymers on miscibility is negligible, which can be seen from the results of mechanical properties. This is explained with the low concentration of the dispersed EPDM phase.

4.3. Morphology of the SAN/EPDM/EPDM-g-PS blends

The morphology of SAN/EPDM blends compositions 95/5 and 90/10 can be seen on the micrographs of the cryogenically fractured surfaces of

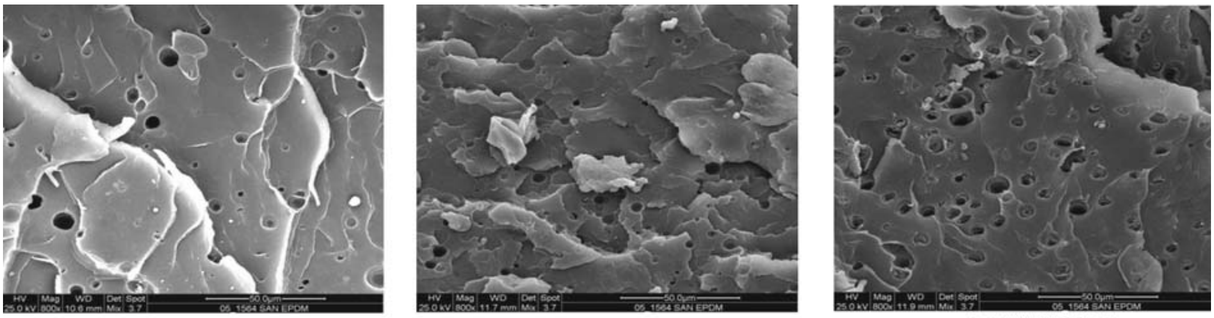

a) SAN/EPDM 95/5 b) SAN/EPDM-3 c) SAN/EPDM-3-T

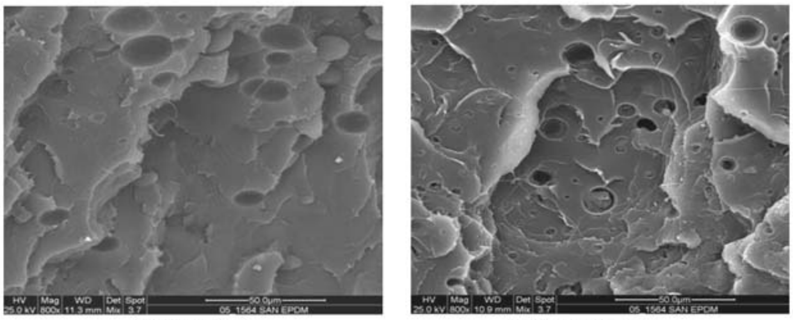

d) SAN/EPDM-7 e) SAN/EPDM-7-T

Figure 6. SEM micrographs of SAN/EPDM/EPDM-g-PS blends (95/5/5): a) without a compatibilizer, b) formed by grafts synthesized for 3 hours, c) formed by grafts synthesized for 3 hours using TAC, d) formed by grafts synthesized for 7 hours, e) formed by grafts synthesized for 7 hours using TAC

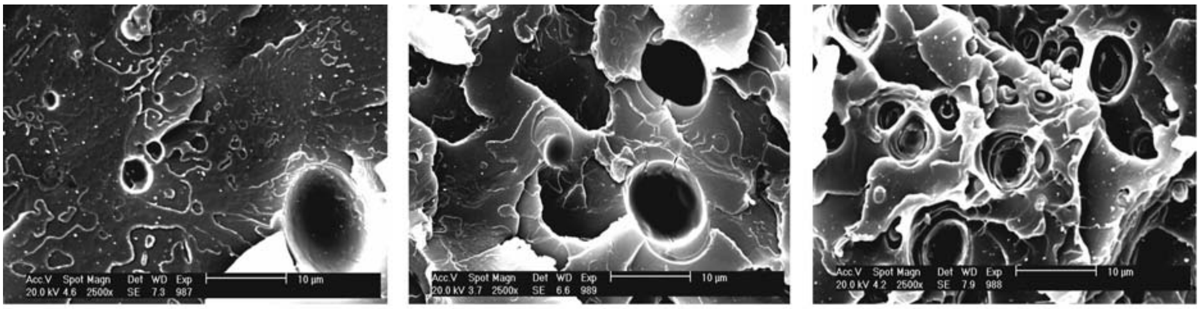

a) SAN/EPDM 90/10 b) SAN/EPDM-3 c) SAN/EPDM-3-T

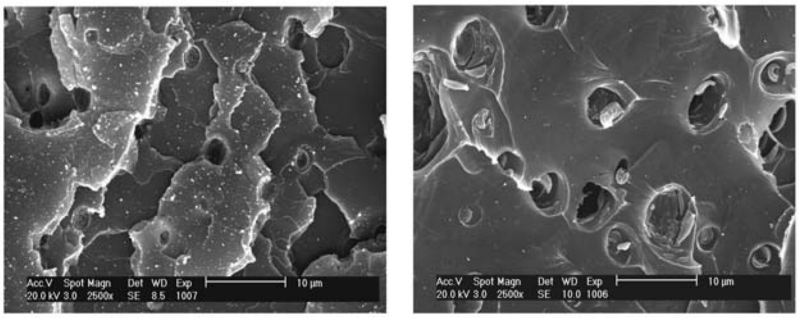

d) SAN/EPDM-7 e) SAN/EPDM-7-T

Figure 7. SEM micrographs of SAN/EPDM/EPDM-g-PS blends (90/10/5): a) without a compatibilizer, b) formed by grafts synthesized for 3 hours, c) formed by grafts synthesized for 3 hours using TAC, d) formed by grafts synthesized for 7 hours, e) formed by grafts synthesized for 7 hours using TAC

SAN/EPDM blends, Figures 6 and 7. A different morphology of the studied blends is obtained, which is result of various structures of the added synthesized graft copolymers. The blends attain a more uniform distribution of EPDM polymer in the SAN matrix, which can be seen when comparing micrographs a)–e) on Figures 6 and 7. Considering the morphology of the samples SAN/EPDM-3 and SAN/EPDM-3-T, Figure 6b and 6c, (particle size of dispersed phase are 4.7 µm and 2.9 µm, respectively), it can be seen some size reduction and homogeneity of the dispersed phase as well as for the samples prepared with the graft copolymers synthesized 7 hours with and without coagent TAC, Figure 6d and 6e (particle sizes of dispersed phase are 9.8 µm and 5.9 µm, respectively). It is assumed that slight size reduction of the dispersed phase in the studied samples compositions 95/5/5 could be the result of the low concentration of EPDM. Minor differences in morphology of the studied blends are reflected in the negligible changes of mechanical properties.

Notable differences in the size and distribution of the dispersed phase for samples compositions 90/10/5 (prepared with graft copolymers synthesized with and without TAC) can be seen on micrographs 7b and 7c. On micrograph 7c the domains of the dispersed phase are smaller (2.8 µm) and much better distributed in the matrix than the domains of the other studied blends (particle size are in the range of 3.1–6.4 µm) micrograph 7b, 7d and 7e. It is obvious that graft copolymers with a lower graft density of side branches, Figure 2b form the finest morphology, which requires better interactions and improves compatibility in blends. It can be concluded that effect of different concentration of side branches on compatibility in blends is particularly visible when the concentration of side branches is lower or equal to the optimal (micrographs 6c and 7c). On the other hand, when the concentration of the side branches is higher then optimal the minor changes in compatibility are present in spite of different structure of compatibilizer (micrographs 7d and 7e). The results of the studied blend samples show good relation between morphology and the changes of mechanical properties.

5. Conclusions

Various parameters like polymerization time and presence of coagent TAC provide synthesis of graft copolymers of different structures, i.e., various concentrations of side branches. From the results of mechanical properties and the morphology it can be seen that different structures of graft copolymers, which is used as a compatibilizer, influence the miscibility in SAN/EPDM blends. The highest improvements in miscibility are obtained for the blends prepared with the graft copolymer (EPDM-g-PS-3T), which contain the optimal concentration of side branches, i.e., optimal graft density.

References

[1] Ji Y., Ma J. H., Liang B.: In situ polymerization and in situ compatibilization of polymer blends of poly (2,6-dimethyl-1,4-phenylene oxide) and polyamide 6. Materials Letters, **59**, 1997–2000 (2005).

[2] Wildes G. S., Harada T., Keskkula H., Paul D. R., Janarthanan V., Padwa A. R.: Synthesis and characterization of an amine-functional SAN for the compatibilization of PC/ABS blends. Polymer, **40**, 3069–3082 (1999).

[3] Martin P., Devaux J., Legras R., van Gurp M., van Duin M.: Competitive reactions during compatibilization of blends of polybutyleneterephthalate with epoxide-containing rubber. Polymer, **42**, 2463–2478 (2001).

[4] Higgin J. S., Tambasco M., Lipson J. E. G.: Polymer blends; stretching what we can learn through the combination of experiment and theory. Progress in Polymer Science, **30**, 832–843 (2005).

[5] Fekete E., Földes E., Pukánszky B.: Effect of molecular interactions on the miscibility and structure of polymer blends. European Polymer Journal, **41**, 727–736 (2005).

[6] Utracki L. A.: Polymer Alloys and Blends. Carl Hanser, New York, (1990).

[7] Fayt R., Jerome R., Teyssie P.: Molecular design of multicomponent polymer systems. XII. Direct observation of the location of a block copolymer in low-density polyethylene-polystyrene blends. Journal of Polymer Science Part C: Polymer Letters, **24**, 25–28 (1986).

[8] Janata M., Masař B., Toman L., Vlček P., Látalová P., Brus J., Holler P.: Synthesis of novel types of graft copolymers by a 'grafting-from' method using ring-opening polymerization of lactones and lactides. Reactive and Functional Polymers, **57**, 137–146 (2003).

[9] Eklind H., Maurer F. H. J., Steeman P. A. M.: Micromechanical and microdielectric transitions in P(S-g-EO) modified PPO/PMMA blends. Polymer, **38**, 1047–1055 (1997).

[10] Cartier H., Hu G. H.: A novel reactive extrusion process for compatibilizing immiscible polymer blends. Polymer, **42**, 8807–8816 (2001).

[11] Mitra S., Ghanbari-Siahkali A., Kingshott P., Rehmeier H. K., Abildgaard H., Almdal K.: Chemical degradation of crosslinked ethylene-propylene-diene rubber in an acidic environment. Part II. Effect of peroxide crosslinking in the presence of a coagent. Polymer Degradation and Stability, **91**, 81–93 (2006).

[12] Coran A. Y.: Vulcanization. in 'Encyclopedia of Polymer Science and Engineering' (eds.: Mark H. F., Bikales N. M., Overberger C. G., Menges G., Kroschwitz J. I.) Wiley Interscience Publication, New York, Vol 17, 666–698 (1985).

[13] Ptiček A., Hrnjak-Murgiæ Z., Jelenčić J., Kovačić T.: Study of the effect of structure of ethylene-propylene-diene-graft-polystyrene copolymers on their physical properties. Polymer Degradation and Stability, **90**, 319–325 (2005).

[14] Dikland H. G., Hulskotte R. J. M., Van der Does L., Bantjes A.: The mechanism of EPDM peroxide vulcanizations in the presence of triallylcyanurate as a coagent. Kautschuk und Gummi, Kunststoffe, **46,** 608–613 (1993).

[15] Kumar M. S. C., Alagar M.: Development and characterisation of vinyloxyaminosilane grafted ethylene-propylene-diene terpolymer (EPDM-g-VOS) for engineering applications. European Polymer Journal, **38**, 2023–2031 (2002).

[16] Mathew M., Thomas S.: Compatibilisation of heterogeneous acrylonitrile-butadiene rubber/polystyrene blends by the addition of styrene-acrylonitrile copolymer: effect on morphology and mechanical properties, Polymer, **44**, 1295–1307 (2003).

eXPRESS Polymer Letters Vol.1, No.3 (2007) 180–187
Available online at www.expresspolymlett.com
DOI: 10.3144/expresspolymlett.2007.28

Effect of thermal and hygrothermal aging on the plane stress fracture toughness of poly(ethylene terephthalate) sheets

T. Bárány[1]*, *E. Földes*[2], *T. Czigány*[1]

[1]Department of Polymer Engineering, Faculty of Mechanical Engineering, Budapest University of Technology and Economics, H-1111 Budapest, Műegyetem rkp. 3., Hungary
[2]Department of Polymer Physics and Chemistry, Institute of Chemistry, Chemical Research Center, Hungarian Academy of Sciences, H-1525 Budapest, P.O. Box 17, Hungary

Received 24 January 2007; accepted in revised form 7 March 2007

Abstract. The in-plane (plane stress) fracture toughness of two polyester (PET, PETG) sheets were assessed using the essential work of fracture (EWF) method after thermal and hygrothermal aging performed just below glass temperature. This ensured that physical aging takes place. On the aged sheets the yield stress (σ_y), enthalpy relaxation (ΔH) and EWF parameters were determined. It was observed that the essential work of fracture component related to the specific yielding ($w_{e,y}$) is suitable for assessing physical aging – independently of the humidity content. A good linear correlations exists between $w_{e,y}$, σ_y and ΔH.

Keywords: *fracture and fatigue, essential work of fracture (EWF), fracture toughness, physical aging, hygrothermal aging*

---

1. Introduction

The transparency of polyesters (e.g. PET bottles) is ensured by a rapid cooling applied during processing, when the material gets into a metastable, amorphous state, characterized by the absence of long-term order. When polymers are below their glass temperatures (T_g), the positions of molecular chains are fixed but the free volume is still significant. The free volume – as well as the temperature – has a significant impact on the mobility of the molecular chain segments. The polymeric systems being in metastable state approach an equilibrium state through slow molecular relaxation. Owning to this process the free volume and mobility of the segments decrease, which results in embrittlement. This slow process is called physical aging and depends on the temperature. The relaxation time decreases exponentially with increasing temperature. In case of PET – used under T_g – the relaxation is very slow, so noticeable change in the properties can occur after only after several years. This explains the use of accelerated aging at higher temperature.

The polyesters are applied both in the absence (dry) and in the presence of water (in wet state, in contact with soft drinks or mineral water). Under wet condition PET absorbs water, the amount of which approaches to the saturation value determined by the ambient parameters. Moisture content increases the molecular mobility significantly, i.e. it reduces the relaxation time, since water acts as a plasticizer. Physical aging has varying importance in case of dry air [1, 2], in presence of humidity [3] and in plasticized systems [1] and it can have very differ-

---

*Corresponding author, e-mail: barany@pt.bme.hu ent effects on the mechanical and fracture properties of polymers. In case of polyester foils stored under normal conditions significant deterioration can occur in even a couple of years. It is important to know, however, how the properties of material change under higher humidity conditions during storage and use.

The embrittlement induced by physical aging can be assessed by determining of the change in the yield stress (σ_y – tensile tests) [2–4]. Furthermore it can be characterized by measuring the enthalpy relaxation (ΔH – differential scanning calorimetry, DSC) [2, 5–7]. Physical aging also influences the fracture mechanical properties of the polymer but only relatively few studies have been published so far. [1–4, 7]. For assessing the fracture characteristics of ductile, tough polymers the Essential Work of Fracture (EWF) method has gained acceptance recently [1–4, 7–15], which has been developed mainly for in-plane load on single- and double-etched notched tensile specimens (SEN-T [12, 13] and DEN-T [1, 14, 15], respectively) and used widely. The advantage of DEN-T specimen is its symmetry, i.e. the distortion of the sample due to loading can be avoided, especially when the specimen is too long and narrow.

The goal of the present study is to prove the applicability of the plane-stress essential work of fracture method for monitoring the effect of physical and hygrothermal aging.

2. EWF method

The EWF theory (see Refs. [1, 2, 4, 7] and references therein), credited to Broberg, splits the total energy required to the fracture of a pre-cracked specimen into two components: the essential (W_e) and non-essential work (W_p) of fracture. W_e is needed to fracture the polymer in the crack propagation zone and thus to generate new surfaces. W_p is the actual work consumed in the outer plastic region, where various energy dissipation mechanisms take place. The total fracture energy, W_f, calculated from the area of the force-elongation curves, can thus be expressed by Equation (1):

$$W_f = W_e + W_p \tag{1}$$

Considering the surface- (i.e. Lt) and volume-dependence (i.e. L^2t) of the constituent terms, Equation (1) can be rewritten using these specific terms (2), (3):

$$W_f = w_eLt + \beta w_pL^2t \tag{2}$$

$$w_f = \frac{W_f}{Lt} = w_e + \beta w_p L \tag{3}$$

where L is the ligament length, t is the specimen thickness and β is a shape factor related to the shape of the plastic zone. The basic prerequisite of the EWF method is that the ligament (L) of the specimen should fully yield before the crack propagation starts. Based on Equation (3), we can be determined from the intercept of the linear regression curve fitted to the plot of w_f *vs.* L.

It was found that w_e is a composite term under plane-stress conditions consisting of a yielding ($w_{e,y}$) and a necking+tearing ($w_{e,n}$) component. The force-elongation behavior displayed in Figure 1a allowed us to separate the specific work of fracture required for yielding (w_y) and that consumed by necking+tearing (w_n). As a consequence, the data

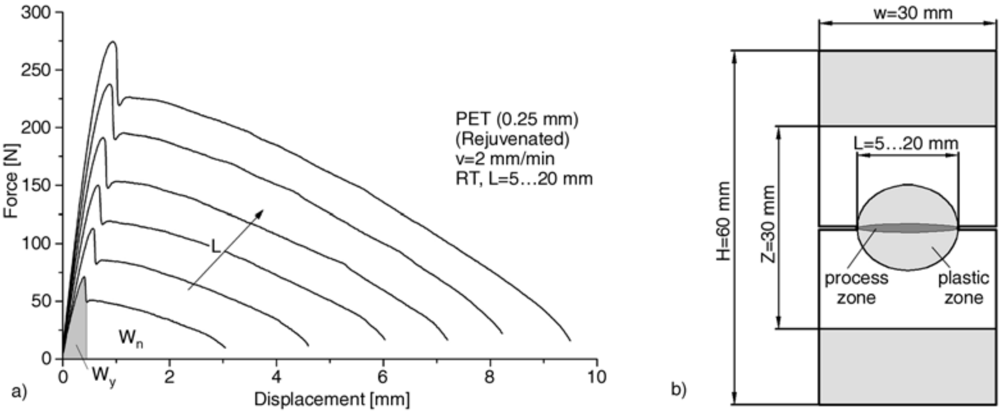

Figure 1. a) Characteristic force-elongation curves of PET (RJ) showing the energy partitioning, b) Dimension of the DDEN-T specimens

reduction given by Equation (3) changed to (4), (5), (6) ([1–4, 8, 11, 14, 15] and references therein):

$$w_f = w_{f,y} + w_{f,n} = w_e + \beta w_p L \tag{4}$$

$$w_{f,y} = w_{e,y} + \beta' w_{p,y} L \tag{5}$$

$$w_{f,n} = w_{e,n} + \beta'' w_{p,n} L \tag{6}$$

This energy partition has been proved experimentally for several ductile polymer sheets ([1–4, 8, 11, 14, 15] and references therein).

Under plane stress condition the EWF approach can be applied, if the following requirements are fulfilled:

1. The total yielding of the ligament and necking should precede crack propagation.
2. Geometrical similarity of the F–x curves registered on DEN-T specimens with different ligament lengths.
3. $L \le 2R_p$, which ensures the complete yielding of ligament prior to crack propagation. In this case a linear correlation between W_p and L^2 exists. R_p is the radius in the plastic zone at the crack tip.
4. $L \le W/3$ which ensures that the edge effects are avoided, i.e. plastic deformation occurs within the ligament region.
5. $L \ge (3–5)t$, which ensures pure plane stress in the ligament region avoiding the plane stress/plane strain transition.

Based on the above written criteria, the ligament lengths are limited by the following relation (7):

$$(3-5)t \le L \le \min\left(2R_p; \frac{W}{3}\right) \tag{7}$$

Note that the upper limit of the applicability of this method was determined for metals therefore it can be stated according to the related literature that this restriction is too conservative for ductile polymers [14–16].

3. Experimental

3.1. Materials and their aging

Two kinds of amorphous copolyester sheets (PET 9921, PETG 6763) produced by a twin-screw extruder (T = 220–240°C, 90 rpm) followed by chill roll sheeting (T = 65°C), were provided by Eastman Chemical Company (Kingsport, TN). Sheets with a thickness of approximately 0.3 mm were studied both after rejuvenation (RJ) and aging for 6–264 hours. The rejuvenation and the aging were performed in a thermostatic oven 87 and 67°C, respectively. Note that the former temperature is just above the glass transition temperature (T_g = 74 and 77°C), whereas the latter one is below T_g. In order to keep the sheet form, the sheets were sandwiched between two preheated glass plates (ca. 4 mm thick each). During hygrothermal aging the sheets were immersed in distilled water.

3.2. Material characterization

For the determination of enthalpy relaxation differential scanning calorimetry (DSC) traces were recorded on a Mettler DSC 821 device in the temperature range from –50 to +300°C at a heating rate of 20°C/min. In case of hygrothermal aging the DSC tests were run on the sample after it was dried under ambient conditions. For the determination of enthalpy relaxation spline approach was selected.

3.3. Specimens and their testing

The specimens were oriented along the machine (film production) direction. Static tensile mechanical properties were determined on dumbbells (1B, according to EN ISO 527) at room temperature (*RT*) and at a crosshead speed of v = 2 mm/min. For the EWF study, double edge-notched specimens (DEN-T) were subjected to tensile loading at room temperature at the aforementioned deformation rate. The dimensions of the DEN-T specimen are given in Figure 1b. The free ligament length of DEN-T specimens ranged from L = 5 to 20 mm. For every ligament length five specimens were prepared and tested.

4. Results

4.1. Tensile tests

Earlier it was demonstrated that yield stress can be a suitable parameter for determining the effects of the plasticizer on the physical aging that occurred in normal environment [1]. Figure 2 shows the change of the yield stress after thermal and hygrothermal aging. The related values are listed in Table 1. One can see that the thermal aging caused embrittlement and increased σ_y for both materials. In contrast, hygrothermal aging decreased the yield

Table 1. Yield stress (σ_y) and enthalpy relaxation (ΔH) results for PET and PETG sheets thermally/hygrothermally aged for 0…264 hours

Aging time [h]	**Thermal aging**				**Hygrothermal aging**			
	PET		**PETG**		**PET**		**PETG**	
	σ_y [MPa]	**ΔH [kJ/kg]**	**σ_y [MPa]**	**ΔH [kJ/kg]**	**σ_y [MPa]**	**ΔH [kJ/kg]**	**σ_y [MPa]**	**ΔH [kJ/kg]**
0 (RJ)	52.3	0.98	46.6	1.04	52.3	0.98	46.6	1.04
6	58.0	3.46	51.8	2.72	40.6	1.08	40.1	1.12
24	58.8	4.71	52.8	3.23	39.9	1.13	41.6	1.24
96	58.9	4.92	54.3	3.59	39.7	1.31	41.9	1.41
264	59.8	5.53	55.2	4.37	42.3	1.49	46.0	1.78

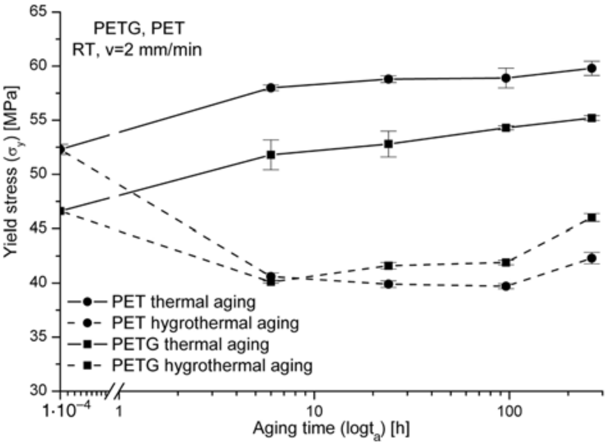

Figure 2. The change of yield stress (σ_y) as a function of aging time (logt_a)

stress after the first 6 hours (the humidity content after ca. 6 hours reaches its saturation value – ca. 1 wt%). After hygrothermal aging physical aging manifested for PETG (yield stress increased). For PET a minor decrease can be experienced up to 96 hours and after physical aging occurred.

4.2. Morphological tests

Physical aging can be assessed by measuring the enthalpy relaxation (ΔH) with DSC. Figures 3a and 3b present the DSC curves of thermally aged PET and hygrothermally aged PETG, respectively. The enthalpy relaxation can be determined by integrating the area designated by grey color (Figure 3). Figure 4 shows ΔH *vs*. aging time in semi-logarithmic scale and Table 1 contains its values. Note that thermal aging influences ΔH similarly to the yield stress, but hygrothermal aging affects it to a much smaller extent after soaking in water at 67°C. The reason is that the water molecules diffused in-between the molecular chains, therefore the molecular mobility increases, the relaxation time decreases, so does ΔH.

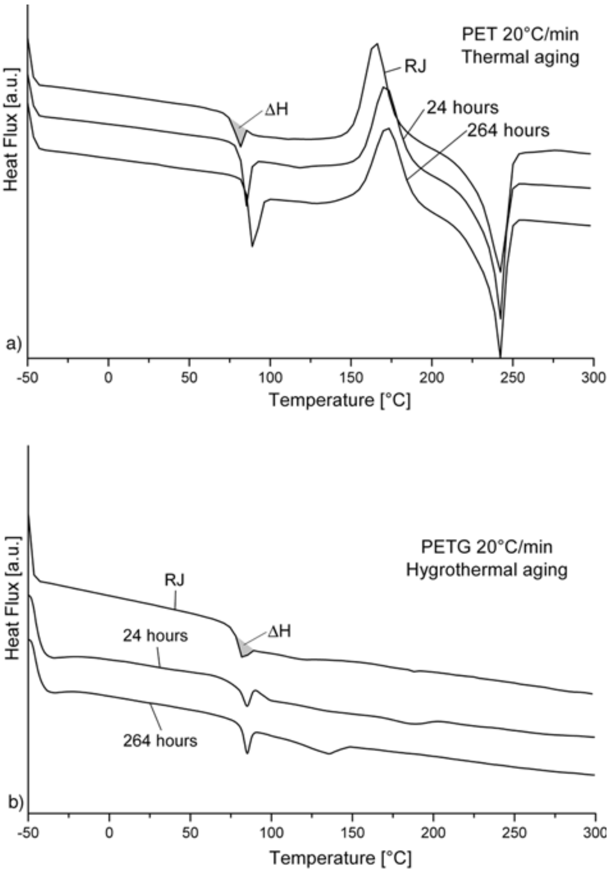

Figure 3. a) DSC curves of thermal aged PET, b) DSC curves of hygrothermal aged PETG

As it is presented above, σ_y changes significantly due to this complex effect, both elements (physical aging and the plasticizing effect of water) influence its value considerably. The enthalpy relaxation cannot or can slightly evolve owning to the higher molecular mobility caused by the presence of water molecules. The amount of absorbed water increases continuously up to 6 hours and reaches its saturation value, i.e. humidity content of the investigated polyesters from this time on is constant. So, the change of the enthalpy relaxation refers to the physical aging of this plasticized material. Therefore it is not worth to look for correlation with the initial

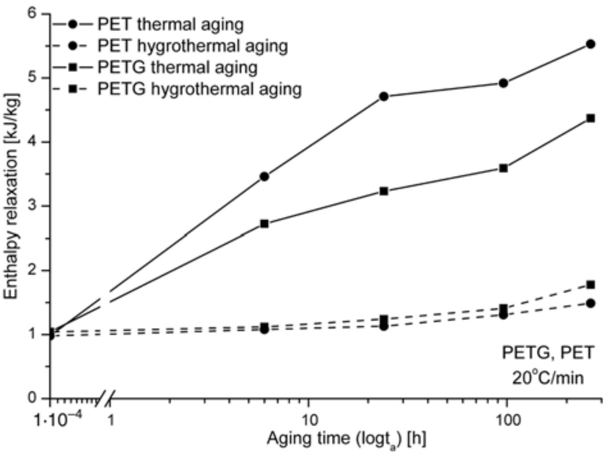

Figure 4. Change of enthalpy relaxation (ΔH) as a function of aging time ($\log t_a$)

value (RJ) since it is not in plasticized state. It can be stated that the physical aging of the polymer becomes much slower by hygrothermal aging owing to the presence of water, which can be assessed by the change of the enthalpy relaxation. The enthalpy relaxation is smaller 4.5 times for PETG and 9 times for PET than measured after thermal aging.

4.3. EWF tests

Figure 5a and 5b show tensile curves of DEN-T specimens cut from thermally aged PETG and from hygrothermally aged PET sheets. By thermal aging, the maximum force increases and the tearing related deformation decreases as a function of aging time. By hygrothermal aging, the maximal load decreases up to 6 hours and the deformation increases giving evidence to the plasticizing effect of diffused water. Comparing the tensile curve of DEN-T aged for 264 hours to that aged for 6 hours, one can notice that the maximum force increases and the tearing related deformation decreases. This refers to physical aging.

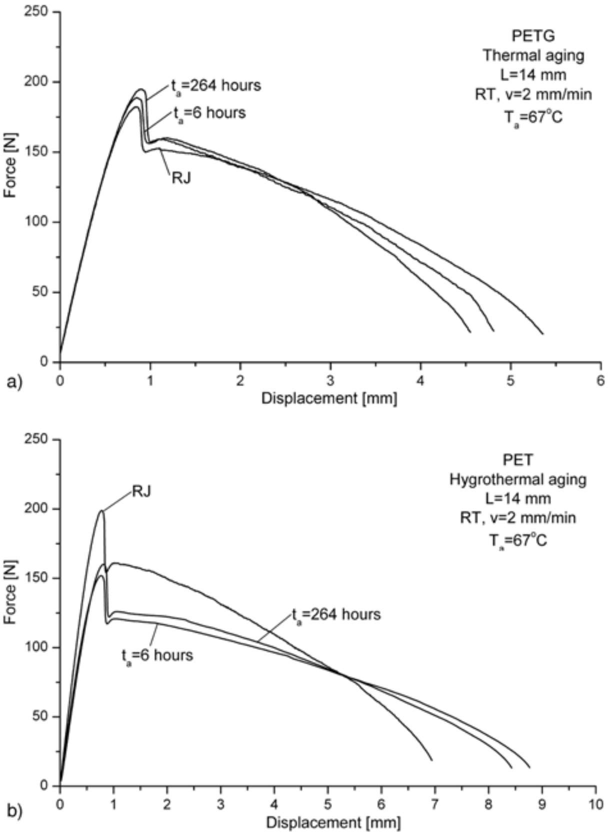

Figure 5. a) Force-deformation curves of DDEN-T specimens (L = 14 mm) of PETG in RJ stage and thermally aged for 6 and 264 hours, b) Force-deformation curves of DDEN-T specimens (L = 14 mm) of PET in RJ stage and hygrothermally aged for 6 and 264 hours

Table 2 and 3 list the specific essential work (w_e), specific ligament related essential work of fracture component ($w_{e,y}$), specific plastic fracture work (βw_p) and its necking+tearing related component ($\beta'' w_{p,n}$) for both investigated polyesters in case of thermal and hygrothermal aging, respectively. The tables also contain the correlation coefficients (R). It can be seen that in case of the w_e no aging-related changes can be detected, while $w_{e,y}$ increases with the increasing aging time for both materials and its tendency is similar to that of yield stress and

Table 2. EWF parameters (w_e, $w_{e,y}$, βw_p, $\beta'' w_{p,n}$) for PET and PETG sheets thermally/hygrothermally aged for 0…264 hours

Aging time [h]	Thermal aging											
	PET						PETG					
	w_e [kJ/m²]	$w_{e,y}$ [kJ/m²]	βw_p [MJ/m³]	R [–]	$\beta'' w_{p,n}$ [MJ/m³]	R [–]	w_e [kJ/m²]	$w_{e,y}$ [kJ/m²]	βw_p [MJ/m³]	R [–]	$\beta'' w_{p,n}$ [MJ/m³]	R [–]
0 (RJ)	50.0	13.6	10.4	0.99	9.0	0.99	39.1	12.4	7.6	0.99	6.4	0.99
6	51.7	14.3	10.3	0.99	8.6	0.99	40.8	12.9	7.3	0.99	5.8	0.98
24	53.7	14.4	9.7	0.99	7.6	0.99	42.7	13.7	6.9	0.98	5.4	0.97
96	53.4	15.3	9.8	0.99	7.9	0.99	40.6	14.4	6.7	0.99	5.1	0.99
264	48.9	15.7	9.8	0.99	8.1	0.98	43.1	15.4	6.4	0.99	4.7	0.98

Table 3. EWF parameters (w_e, $w_{e,y}$, βw_p, $\beta'' w_{p,n}$)for PET and PETG sheets thermally/hygrothermally aged for 0…264 hours

Aging time [h]	Hygrothermal aging											
	PET						PETG					
	w_e [kJ/m²]	$w_{e,y}$ [kJ/m²]	βw_p [MJ/m³]	R [–]	$\beta'' w_{p,n}$ [MJ/m³]	R [–]	w_e [kJ/m²]	$w_{e,y}$ [kJ/m²]	βw_p [MJ/m³]	R [–]	$\beta'' w_{p,n}$ [MJ/m³]	R [–]
0 (RJ)	50.0	13.6	10.4	0.99	9.0	0.99	39.1	12.4	7.6	0.99	6.4	0.99
6	40.4	7.2	10.5	0.99	9.4	0.99	39.0	8.1	7.1	0.99	5.8	0.98
24	40.0	6.4	10.5	0.99	9.3	0.99	29.1	8.8	7.8	0.99	6.5	0.99
96	43.5	5.5	10.2	0.99	8.9	0.99	31.9	8.9	7.8	0.99	6.5	0.99
264	42.9	8.4	10.1	0.99	9.0	0.99	33.5	10.7	7.4	0.99	6.2	0.99

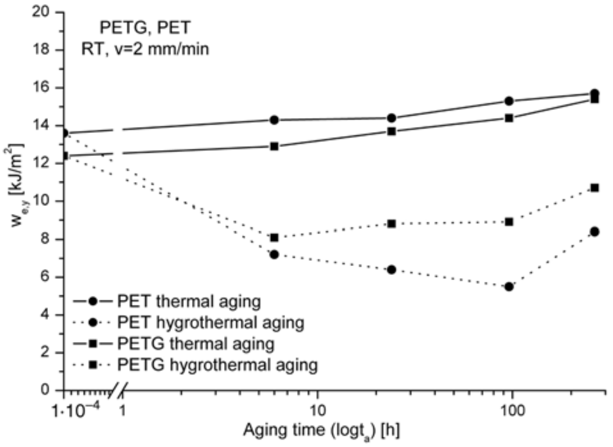

Figure 6. Change of the specific yielding-related essential work of fracture ($w_{e,y}$) as a function of aging time (logt_a)

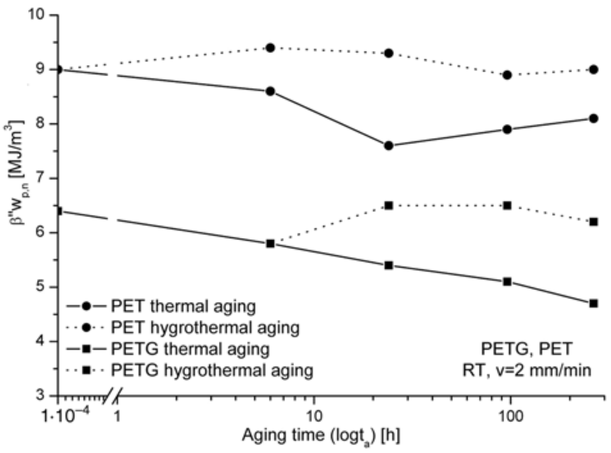

Figure 7. Change of the specific necking+tearing-related plastic work of fracture ($\beta'' w_{p,n}$) as a function of aging time (logt_a)

enthalpy relaxation (Figure 6). By hygrothermally aged samples $w_{e,y}$ shows a similar trend to yield stress: in the first 6 hours of aging the materials reach their saturation state (σ_y and $w_{e,y}$ decrease), after 6 hours physical aging takes place (σ_y and $w_{e,y}$ increase slightly, cf. Figures 2 and 6). Based on the result one can state that the specific yielding related work of fracture ($w_{e,y}$) is a suitable parameter for assessing the thermal and hygrothermal aging of polyesters.

In case of thermal aging βw_p, which represents the resistance of the material against crack propagation – as expected –, decreases with physical aging. For PETG it decreases monotonously but for PET no further decrease can be experienced after 24 hours. The reason is that little crystallization may have taken place in the crystallizable amorphous PET subjected to further aging. For the specific necking+tearing related plastic work of fracture ($\beta'' w_{p,n}$) the above mentioned tendency appears more significantly since in this segment crack propagation occurs and a completely plastic zone is formed (Figure 7). During hygrothermal aging the plasticizer effect [17] of the diffused water increases the plastic fracture work (βw_p), while physical aging has an opposite effect. The question is which effect dominates, or whether these two effects cancel each other. In the present case βw_p shows no significant change as a function of aging time (Figure 7), which allow us to opt for the latter possibility. Investigating $\beta'' w_{p,n}$ a similar conclusion can be drawn as for βw_p. Hence βw_p and $\beta'' w_{p,n}$ can represent the effect of either physical aging or plasticizer, but if both conditions are present together this statement is not true.

5. Discussion

The effect of physical aging is different for polyesters in the presence of various plasticizers. Adding plasticizer (NPGDB [1]) its effect is more significant, since the glass temperature decreases considerably. Absorbed water reduces T_g, because of the presence of humidity a part of the polymer/polymer interaction changes due to polymer/water interactions. For immersed samples the distilled water ensures the equilibrium water content in the polymer. When the polymer relaxes after immersing in water and the amount of polymer/polymer interaction increases, water will be present in equilibrium amount (corresponding to the ambient conditions) and ensures the permanence of plastic deformation. Accordingly, the enthalpy relaxation changes less than in case of thermal degradation (Figure 4). The plasticizer effect of water has practical importance since less physical aging takes place, so life cycle of PET bottles can be extended. Physical aging increases yield stress and the plasticizing effect of water decreases it. In Figure 2 one can see that a little physical aging superposes on the plasticizer effect of the water in case of hygrothermal aging (Figure 4).

The specific essential work (w_e) does not change due to aging. Specific yielding related essential work of fracture component ($w_{e,y}$) shows also a good correlation with yield stress and enthalpy relaxation. The specific plastic work and its $\beta''w_{p,n}$ component decreases in case of thermal aging, and above ca. 1 wt% water content they are independent of physical aging.

Based on the results one can state that the specific yielding related essential work of fracture component ($w_{e,y}$) measured on specimens loaded under plane stress condition is suitable for assessing physical aging independently of humidity content. A good linear correlation can be found between $w_{e,y}$ and σ_y (Figure 8).

In the case of enthalpy relaxation a linear regression line cannot be fitted to each point determined on the thermally and hygrothermally aged specimens, since the diffused water does not influence the value of ΔH but it does $w_{e,y}$. Therefore only those values can be correlated which are measured on the thermally aged samples (Figure 9).

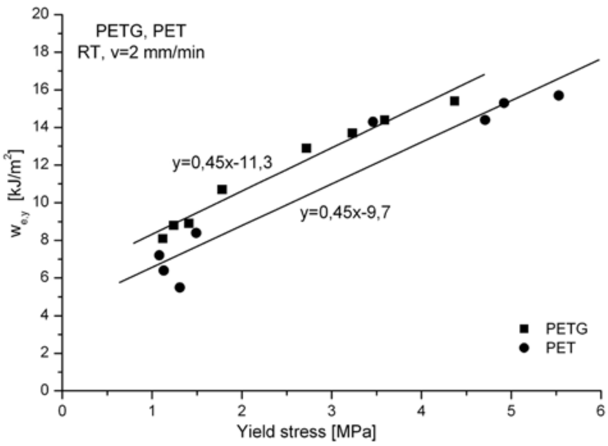

Figure 8. Correlation between $w_{e,y}$ and σ_y

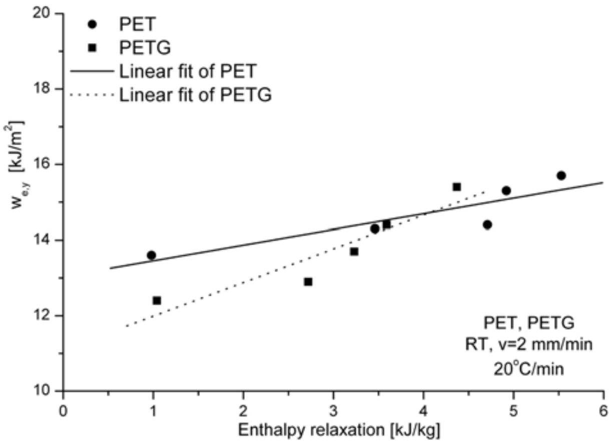

Figure 9. Correlation between $w_{e,y}$ and ΔH

6. Conclusions

Based on this work devoted to assessing the in-plane (plane stress) fracture toughness of physically aged polyester sheets after thermal and hygrothermal aging using the essential work of fracture (EWF) method, the following conclusions can be drawn:

- The effect of physical aging caused by thermal and hygrothermal aging under glass temperature (T_g) can be followed by measuring the change of yield stress (σ_y) and the specific yielding-related essential work of fracture ($w_{e,y}$).
- The specific necking+tearing related plastic work of fracture component ($\beta''w_{p,n}$) can also be a suitable factor for assessing physical aging. This parameter decreases with the aging time. With the embrittlement of the polyesters, associated with the increasing yield stress, the resistance to crack propagation decreases.

Acknowledgements

This study was supported by Hungarian Scientific Research Fund (OTKA NI62729).

References

[1] Karger-Kocsis J., Bárány T., Moskala E. J.: Plane stress fracture toughness of physically aged plasticized PETG as assessed by the essential work of fracture (EWF) method. Polymer, **44**, 5691–5699 (2003).

[2] Bárány T., Ronkay F., Karger-Kocsis J., Czigány T.: In-plane and out-of-plane fracture toughness of physically aged polyesters as assessed by the essential work of fracture (EWF) method. International Journal of Fracture, **135**, 251–265 (2005).

[3] Bárány T., Karger-Kocsis J., Czigány T.: Effect of hygrothermal aging on the essential work of fracture

response of amorphous poly(ethylene terephthalate) sheets. Polymer Degradation and Stability, **82**, 271–278 (2003).

[4] Karger-Kocsis J., Moskala E. J.: Toughness response of amorphous (co)polyesters using the essential work of fracture approach, SPE-ANTEC, **60**, 2002, Vol. II., 1751–1755.

[5] Lu X., Hay J. N.: The effect of physical aging on the rates of cold crystallization of poly(ethylene terephthalate). Polymer, **41**, 7427–7436 (2000).

[6] Aref-Azar A., Arnoux F., Biddlestone F., Hay J. N.: Physical aging in amorphous and crystalline polymers. Part 2. Polyethylene terephthalate. Thermochimica Acta, **273**, 217–229 (1996).

[7] Liu C-H., Nairn J. A.: Using the essential work of fracture method for studying physical aging in thin, ductile, polymeric films. Polymer Engineering and Science, **38**, 186–193 (1998).

[8] Karger-Kocsis J.: Fracture and fatigue behavior of amorphous (co)polyesters as a function of molecular and network variables. in 'Handbook of Thermoplastic Polyesters' (ed.: Fakirov S.) Wiley-VCH, Weinheim, 717–753 (2002).

[9] Hashemi S.: Temperature and deformation rate dependence of the work of fracture in polycarbonate (PC) film. Journal of Materials Science, **35**, 5851–5856 (2000).

[10] Ching E. C. Y., Li R. K. Y., Mai Y-W.: Effects of gauge length and strain rate on fracture toughness of polyethylene terephthalate glycol (PETG) film using the essential work of fracture (EWF) analysis. Polymer Engineering and Science, **40**, 310–319 (2000).

[11] Arkhireyeva A., Hashemi S.: Effect of temperature on work of fracture parameters in poly(ether-ether ketone) (PEEK) film. Engineering Fracture Mechanics, **71**, 789–804 (2004).

[12] Arkhireyeva A., Hashemi S.: Influence of temperature on plane stress ductile fracture of poly(ethylene terephthalate) film. Plastics, Rubber and Composites, **30**, 125–131 (2001).

[13] Arkhireyeva A., Hashemi S.: Fracture behaviour of polyethylene naphthalate (PEN). Polymer, **43**, 289–300 (2002).

[14] Karger-Kocsis J., Czigány T., Moskala E. J.: Deformation rate dependence of the essential and non-essential work of fracture parameters in an amorphous copolyester. Polymer, **39**, 3939–3944 (1998).

[15] Arkhireyeva A., Hashemi S.: Effect of temperature on fracture properties of an amorphous poly(ethylene terephthalate) (PET) film. Journal of Materials Science, **37**, 3675–3683 (2002).

[16] Ferrer Balas D., Maspoch M. Ll., Martinez A. B., Santana O. O.: On the essential work of fracture method: Energy partitioning of the fracture process in iPP films. Polymer Bulletin, **42**, 101–108 (1999).

[17] Chen Y., Lin Z., Yang S.: Plasticization and crystallization of poly(ethylene terephthalate) induced by water. Journal of Thermal Analysis, **52**, 565–568 (1998).